

# Ph.D. Dissertation

Péter Salamon

2013



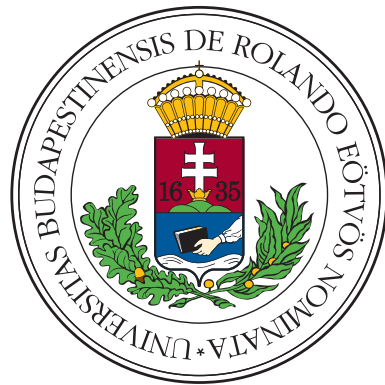
# Extraordinary properties of bent-core and rod-like nematic liquid crystals

PH.D. DISSERTATION

**Péter Salamon**

Institute for Solid State Physics and Optics  
Wigner Research Centre for Physics  
Hungarian Academy of Sciences

Supervisor: Dr. Nándor Éber, C.Sc.



EÖTVÖS LORÁND UNIVERSITY  
Graduate School of Physics

Head of the School: Prof. Dr. László Palla, D.Sc.

Materials Science and Solid State Physics Program  
Program Leader: Prof. Dr. János Lendvai, D.Sc.

Budapest  
2013



# Contents

<b>Foreword</b> . . . . .	1
<b>Acknowledgements</b> . . . . .	3
<b>1. Introduction to Liquid Crystals</b> . . . . .	5
1.1 Liquid crystals in general . . . . .	5
1.1.1 Rod-like liquid crystals . . . . .	6
1.1.2 Bent-core liquid crystals . . . . .	8
1.2 Properties of nematics . . . . .	9
1.2.1 Elasticity and surface alignment . . . . .	9
1.2.2 Anisotropic magnetic and electric properties . . . . .	12
1.2.3 The flexoelectric effect . . . . .	14
1.2.4 Dielectric behavior and molecular properties . . . . .	15
1.2.5 Dynamic dielectric properties . . . . .	17
1.2.6 Optics of nematics . . . . .	24
1.2.7 Pattern formation in nematics . . . . .	28
<b>2. Objectives</b> . . . . .	35
2.1 Bent-core nematic liquid crystals . . . . .	35
2.2 Ultra-low frequency pattern formation . . . . .	38
<b>3. Materials and techniques</b> . . . . .	40
3.1 Dielectric studies . . . . .	40
3.1.1 Measurement technique . . . . .	40
3.1.2 The materials . . . . .	43
3.2 Studies of elasticity . . . . .	44
3.2.1 The splay geometry . . . . .	45
3.2.2 The twist geometry . . . . .	50
3.2.3 Experimental technique . . . . .	54
3.2.4 The materials . . . . .	57
3.3 Time resolved pattern imaging . . . . .	59
3.3.1 Experimental technique . . . . .	59
3.3.2 The used compounds . . . . .	60
<b>4. Results and discussion</b> . . . . .	62
4.1 Dielectric studies . . . . .	62
4.1.1 Thermal characterization of the phase behavior . . . . .	62
4.1.2 Dielectric relaxations in the pure bent-core compound . . . . .	63
4.1.3 Dielectric relaxations in the mixtures . . . . .	68

---

4.1.4	Calculations of molecular dipole moments . . . . .	73
4.1.5	Discussion . . . . .	76
4.2	Studies of elasticity . . . . .	83
4.2.1	Elasticity of a typical bent-core nematic compound . . . . .	83
4.2.2	Simulations of the twist geometry . . . . .	86
4.2.3	The case of an unconventional bent-core compound . . . . .	91
4.2.4	Characterization of a rod-like compound . . . . .	93
4.2.5	Discussion . . . . .	95
4.3	Pattern formation at low frequencies . . . . .	98
4.3.1	The transition to the low frequency regime . . . . .	98
4.3.2	Flashing contrast and current . . . . .	104
4.3.3	Threshold characteristics . . . . .	107
4.3.4	Determination of the flexoelectric coefficients . . . . .	114
4.3.5	Conclusions . . . . .	117
<b>5.</b>	<b>Summary and outlook . . . . .</b>	<b>120</b>
	<b>Appendix A. Theoretical description of the splay geometry . . . . .</b>	<b>126</b>
	<b>Appendix B. Fitting methods . . . . .</b>	<b>129</b>
	<b>Appendix C. Dielectric measurement using an oscilloscope . . . . .</b>	<b>131</b>
	<b>References . . . . .</b>	<b>133</b>
	<b>List of publications . . . . .</b>	<b>143</b>
	<b>Theses . . . . .</b>	<b>144</b>
	<b>Résumé . . . . .</b>	<b>146</b>
	<b>Összefoglaló . . . . .</b>	<b>147</b>

# Foreword

Liquid crystals undoubtedly play an important role in our daily life today, due to the widespread usage of flat displays based on them. Although the liquid crystalline state of matter has been known since the late eighteenth hundreds, the basic phenomena could be well understood by the achievements of the continuum description in the sixties of the last century. The first displays based on the twisted nematic (TN) effect were developed in the seventies, but a significant part of the monitors and televisions uses the same principle until today.

The rise of liquid crystal applications also helped the basic research to go forward. The huge number of newly synthesized compounds led to the discovery of many exotic phases with complicated structures that could exhibit novel phenomena to study. In the nineties, the scientific interest has turned to liquid crystals consisting of bent-core molecules, forming special, so called 'banana' phases that are still under intense studies. The first bent-core materials forming the nematic phase, were created at around the millenium, and since then it has turned out that bent-core nematics exhibit extraordinary properties compared to the conventional rod-like nematic compounds.

The first topic of the dissertation addresses the different nature of rod-like and bent-core nematic liquid crystals concerning their dielectric properties and elasticity. The second main part of the results is about pattern formation in rod-like and in bent-core nematics at very low frequency voltage excitation.

The scientific results included in the dissertation were published in seven papers, cited as [P1], [P2], ... , [P7], and collected separately from the other references in the List of publications.



# Acknowledgements

This dissertation could not have been carried out without the outstanding support of a number of people including the direct colleagues, co-workers from abroad, and the family.

First of all, I would like to thank the great guidance of my supervisor Nándor Éber, who always provided me fast and efficient help in my work. I also wish to express my deepest gratitude to an exceptional researcher Antal Jákli, who offered me the opportunities to work in the Liquid Crystal Institute in Kent, giving a lifelong experience in science and in other fields as well. I am indebted to Ágnes Buka for the fruitful discussions, where she shared her vast amount of experience in research and helped my work with her deep physical insight. I also thank her for providing the work facilities as the director of the Institute of Solid State Physics and Optics.

The excellent scientific and financial support by James T. Gleeson and Samuel Sprunt are gratefully acknowledged. I am also very thankful for the hospitality in the Liquid Crystal Institute and in the Department of Physics of the Kent State University, where a significant part of my experimental work was done.

I am greatly indebted to Katalin Fodor-Csorba, Robert Twieg, and Matthias Lehmann for providing the liquid crystal compounds for my studies. I would like to express my gratitude to Alexei Krekhov and Werner Pesch for their theoretical calculations that could be compared to my experiments.

I gratefully thank Sándor Pekker for the useful discussions on the quantum chemical calculations. I am grateful to István Jánossy, the principal investigator of the OTKA Grant No. K81250, who gave me the chance to attend conferences by providing financial funds. Special thanks to the members of the Department of Complex Fluids for the cheerful and inspiring atmosphere.

Last but not least, I would like to thank Hajnalka Mária Tóháti for the useful advices and her unlimited patience.



# 1. Introduction to Liquid Crystals

## 1.1 Liquid crystals in general

Liquid crystals (LCs) were discovered in 1888 by a botanical physiologist Friedrich Reinitzer, when he observed 'two melting points' in a cholesterol derivative [1]. As the name suggests, liquid crystals have some properties of isotropic liquids and of solid crystals as well. There are many different phases of LCs that lie between the solid crystalline and the isotropic liquid state, thus they are often called *mesophases* and the constituent materials as *mesogens*. A widely used definition is that liquid crystals are anisotropic fluids with long range orientational order and with partial or no translational symmetry. This definition is valid for most cases, however, there are exceptions: for example, the smectic-G is considered a liquid crystalline phase in spite of the fact that it cannot flow and exhibits partial positional order, resulting in the behavior of a rather gel-like soft crystal [2]. The second example is that blue phases can be optically isotropic due to their cubic superstructure, nevertheless, they are also considered liquid crystals [3]. More generally LCs could be defined as ordered soft matter.

Thermotropic liquid crystals change their phases due to the variations of temperature. A thermotropic liquid crystal is called enantiotropic if the mesophases appear either by cooling the material from the isotropic phase or by heating it from the crystalline phase. If the mesophases emerge only in cooling, the mesogen is monotropic. The monotropic phases are metastable, however, in most cases the characteristic time of stability is large enough to study them even several degrees below the transition temperature.

Lyotropic liquid crystals are solutions of amphiphilic molecules in a solvent which is often water. Different liquid crystalline phases appear depending on the concentration of the solute. Lyotropics are very important due to their biological relevance. For example in living organisms cell membranes and vesicles are lyotropic systems. Amphotropic LCs are sensitive for both temperature and concentration changes in their phase behavior [1].

Thermotropic LCs are easier to handle and they are simpler model systems in a sense that they can consist of only a single mesogenic compound. Therefore the comparison between macroscopic and molecular properties can be easier. In this dissertation, we are only concerned with thermotropic liquid crystals.

Liquid crystals are formed by organic molecules with anisotropic shape. In the simplest way, the shape anisotropy can be achieved by making the size of the molecule in one dimension much shorter or larger than the sizes in the other dimensions. This approach results in disc-like and rod-like structures. In the former case we can get columnar phases (discotic LCs). More regularly, however, the mesogenic molecules have elongated, rod-like shape. Nevertheless, various non-conventional shaped molecules (like banana, bowl, star, pyramid, etc...) can also form different mesophases.

### 1.1.1 Rod-like liquid crystals

The conventional rod-like compounds are also called calamitics. The constituting molecules usually have a rigid core built by aromatic rings and flexible aliphatic terminal chains. In the scientific literature, the largest amount of knowledge is available for rod-like LCs and mostly these kind of materials are used in applications as well.

Numerous distinct liquid crystalline phases were observed with different symmetries, spatial structures and of course different physical properties. The simplest calamitic LC phase is the so-called nematic (Fig. 1.1(b)), where the symmetry is uniaxial and only orientational. Here the long axes of the molecules fluctuate around an average direction which is called the director and denoted by a unit vector  $\mathbf{n}$ . The director is considered an axial-vector due to the head-tail symmetry of the molecules, thus  $\mathbf{n} = -\mathbf{n}$  should stand.

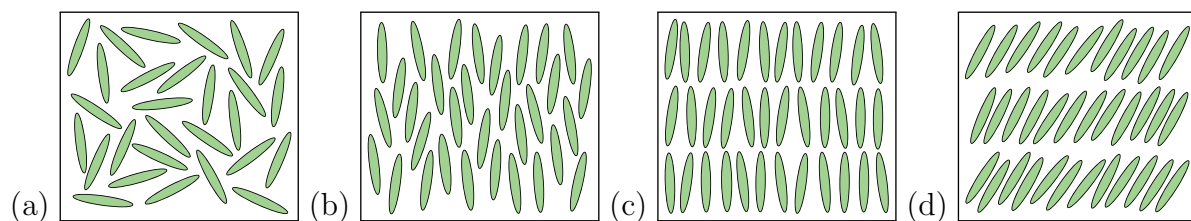


**Fig. 1.1:** Structures of different phases: (a) isotropic, (b) nematic, (c) smectic-A, (d) smectic-C. The ellipses symbolize individual elongated molecules.

In smectic phases, the molecules form layers (Fig. 1.1(c), (d)), thus these mesophases exhibit long range positional order as well. Since the layer thickness correlates with the molecular size, smectics can be considered as two dimensional materials within one layer. The average molecular direction with respect to the layer normal is parallel (Fig. 1.1(c)) and tilted (Fig. 1.1(d)) in the case of smectic-A (SmA) and of smectic-C (SmC) phases, respectively. The SmC phase is optically biaxial.

Introducing chirality in the molecules leads to different phases, usually with helical structures. Both the chiral phase and the chiral center in the molecule is denoted by a star (\*). The chiral nematic phase ( $N^*$ ) is also called cholesteric. Locally it has the symmetries of the nematic, but if no external forces are present, the director follows a helix with a well defined  $P^*$  pitch in a way where the helix axis is always perpendicular to the director (Fig. 1.2). We note that for cholesterics,  $P^*$  is defined as the double of the physical periodicity, because  $\mathbf{n} = -\mathbf{n}$ .

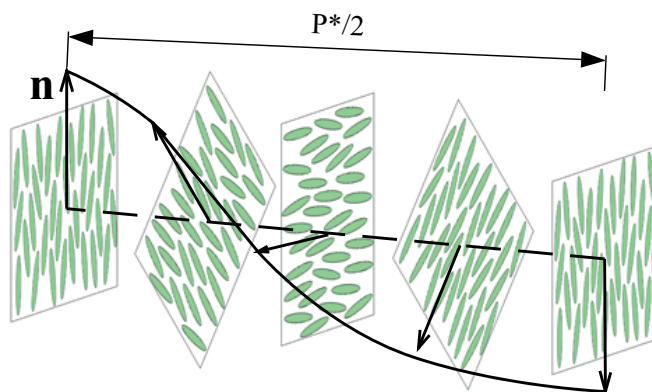


**Fig. 1.2:** The helical structure of the chiral nematic (cholesteric) phase. The director ( $\mathbf{n}$ ) is always perpendicular to the axis of the helix (dashed line); it twists continuously. The half pitch ( $P^*/2$ ) equals to the physical periodicity, since  $\mathbf{n} = -\mathbf{n}$ .

SmC\* has also a helical structure, where the direction of the in-layer tilt follows a helix with an axis parallel to the layer normal (Fig. 1.3). Since the in-layer tilt angle is fixed, the director rotates on the surface of a cone if we observe it along the layer normal. SmC\* is special, because it can be ferroelectric (or antiferroelectric) with a spontaneous polarization ( $\mathbf{P}_s$ ) parallel with the smectic layers. Nevertheless  $\mathbf{P}_s$  averages out globally due to the helical periodicity. A real ferroelectric sample can be obtained, however, if

such liquid crystal is put in a relatively small-scale confined geometry compared to the pitch.

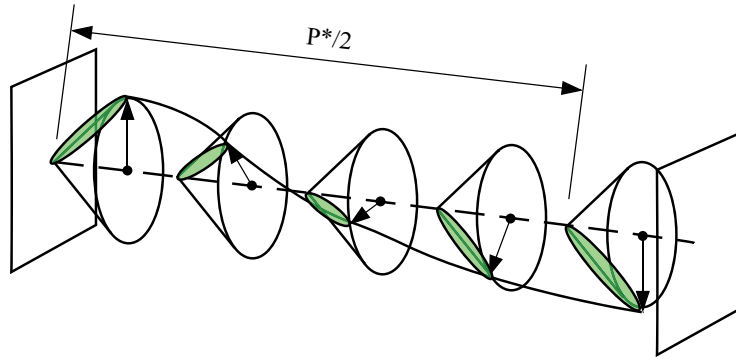


**Fig. 1.3:** The helical structure of the smectic-C phase. The axis of the helix is parallel with the layer normal (dashed line). The tilted director rotates on the surface of a cone. The physical periodicity equals to the pitch ( $P^*$ ).

### 1.1.2 Bent-core liquid crystals

Bent-core (BC) mesogens represent a relatively young family of liquid crystals. The reduced molecular symmetry of BCs compared to that of rod-like compounds lead to the occurrence of phases with unique ordering like the series of 'banana' phases ( $B_1, \dots, B_8$ ). The B phases are mostly three dimensional structures, some details about them are still under discussion. Nevertheless, some can be categorized into columnar-like ( $B_1$ ), and smectic-like ( $B_2, B_3, B_6$  and  $B_7$ ) phases [4]. Maybe the most fascinating feature of this class of liquid crystals is that they can exhibit ferroelectric or antiferroelectric polar ordering, even though the consisting molecules are exclusively achiral [5, 6].

Bent-cores can also form nematic (BCN) phase; that is a main subject of the dissertation. The extraordinary properties of bent-core nematics with the motivations of our research will be discussed in detail in Sec. 2.1.

Though the studies presented in the dissertation can be categorized as basic research, it has to be noted that bent-core liquid crystal have promising perspective in applications as well. Polar phases of achiral bent-core molecules might be the bases of the next generation displays that have wide viewing angles, submillisecond switching time, high contrast ratio, and low threshold voltage [7, 8]. Another type of application may utilize

the large electromechanical response of bent-core liquid crystal based elastomers for sensing and actuating [9].

## 1.2 Properties of nematics

The nematic (N) has the highest symmetry among the liquid crystalline phases that can be characterized by the  $D_{\infty h}$  symmetry group with the axis of the director. The nematic is a non-polar phase. It exhibits long range orientational order, but no positional order; thus nematics can flow freely. The viscous properties can be properly characterized by five independent viscosity coefficients.

The isotropic-nematic phase transition is weakly first order, because the relevant thermodynamic potentials suffer only a small jump at the transition point ( $T_{NI}$ ). The isotropic-nematic transition temperature is often called as clearing point.

The nematic phase is characterized by the tensorial order parameter:  $S_{ij} = S(T)(n_i n_j - \delta_{ij}/3)$ , where  $S(T)$  is the temperature dependent scalar order parameter,  $n_i$  is one component of the director vector,  $i, j = x, y, z$ , and  $\delta_{ij}$  is the Kronecker-delta.  $S(T)$  is used to describe the magnitude of the nematic order; it is defined as  $S(T) = \langle P_2(\cos(\Theta)) \rangle$ , where  $\Theta$  is the angle of one long molecular axis direction with respect to the average, which was defined before as the director.  $P_2()$  is the second order Legendre-polynomial, and  $\langle \rangle$  means an averaging over the orientational distribution function. Molecular theories of nematics can connect several physical quantities (e.g. elastic constants, dielectric, magnetic parameters) to  $S$ , which is usually used to describe the thermal behavior of those.

### 1.2.1 Elasticity and surface alignment

Without special treatment, the director is not uniform in a liquid crystal sample due to the interactions with the container walls or other external forces; thus it is called 'deformed'. Such configurations can be described by a continuum theory if the change of the director can be detected on length scales much larger than the size of a molecule [10]. This requirement is satisfied in most cases. An orientational deformation is described by a director field:  $\mathbf{n}(\mathbf{r})$ .

Since nematic liquid crystals are three dimensional fluids, they cannot sustain shear or extensional strain in a static case. Nevertheless the free energy of nematics is increased if the director field is not uniform. The elastic free energy density ( $f_{elast}$ ) depends on the local director gradient:

$$f_{elast} = \frac{1}{2}K_{11}(\nabla\mathbf{n})^2 + \frac{1}{2}K_{22}(\mathbf{n}(\nabla \times \mathbf{n}))^2 + \frac{1}{2}K_{33}(\mathbf{n} \times (\nabla \times \mathbf{n}))^2, \quad (1.1)$$

where  $K_{11}$ ,  $K_{22}$ , and  $K_{33}$  are the Frank-elastic constants for the elementary deformations of splay, twist, and bend, respectively. An arbitrary bulk director deformation can be described by a combination of splay, twist, and bend deformation modes that are shown in their pure forms in Fig. 1.4(a), (b), and (c), respectively.

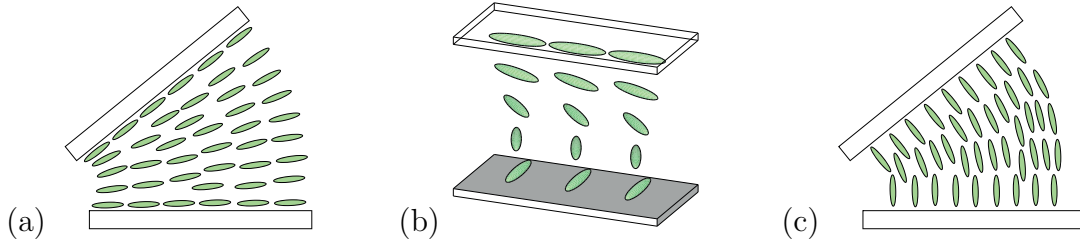


**Fig. 1.4:** The three independent bulk director deformation modes in nematics: (a) splay, (b) twist, (c) bend. The ellipses symbolize the director field.

In both applications and research, liquid crystals are usually put between two parallel glass plates called a sandwich cell. In many cases one wants to have uniform director field, a defect free 'liquid single crystal'. In order to achieve that, the director orientation has to be controlled by so-called alignment layers at the surfaces. If the director is set to be the same on both boundaries, the realized configuration is uniform because then the corresponding elastic free energy (Eq. (1.1)) is the lowest.

There are two main types of surface alignments: homeotropic and planar, in which cases the director is uniformly perpendicular and parallel to the surface, respectively (Fig. 1.5(a), (b)). Usually both types are based on anisotropic adsorption effects on polymer thin layers. Different polyimide coatings are used for homeotropic and planar alignments. In order to achieve planar orientation, the polymer chains are usually aligned by rubbing along the favorable direction. The interaction between the alignment layer and the liquid crystal can be characterized by the anchoring strength. Strong anchoring assumes that the director cannot be changed at the surface in contrast to the case of

weak anchoring. In most cases the planar alignment is considered to establish strong anchoring. In general, the director does not lie perfectly in the plane of the substrate at a planarly treated surface (Fig. 1.5(c)). It is tilted by a small angle ( $1^\circ$ - $5^\circ$ ) called pretilt in the plane that is perpendicular to the substrate and parallel with the rubbing direction. The pretilt is uniform and it depends on the used materials. Nevertheless the effects of this small angle are usually neglected. Besides rubbed polymers, obliquely evaporated *SiO* thin layers forming anisotropic periodic surface structures can also be used to achieve planar orienting layers. Nowadays an emerging technique is the so-called photo-alignment that uses light sensitive polymers and linearly polarized light to align the polymer chains properly.

Homeotropic alignment can be achieved by coating of polymers that have amphiphilic parts preferring perpendicular orientation with respect to the glass surface (Fig. 1.5(a)). In some cases where homeotropic surfaces are used, an appropriate description should include the weak anchoring.

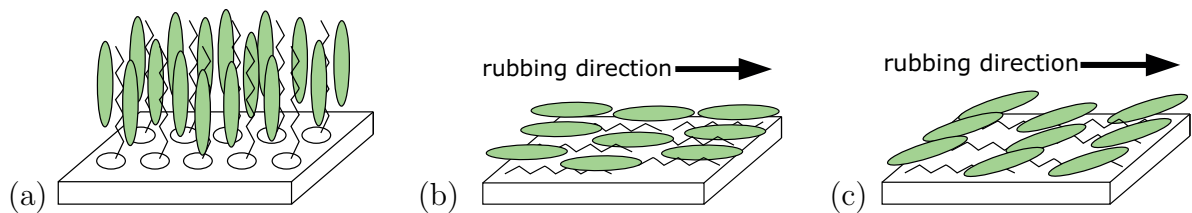


**Fig. 1.5:** Different types of surface alignments for liquid crystals: (a) homeotropic, (b) perfect planar, (c) realistic planar with pretilt. The ellipses symbolize the director.

A liquid crystal cell is called planar if both surfaces are planarly oriented. The rubbing directions can be parallel or antiparallel. In the parallel case, the director at the two plates are at the angle of twice the pretilt, thus the director field in the bulk is not uniform. In order to have an undeformed state, antiparallel rubbing is applied. If the rubbing directions are at an angle of  $90^\circ$ , the cell is called twisted, because the liquid crystal suffers a pure twist deformation inside.

Similarly, if both surfaces are homeotropic, the cell is called homeotropic, while it is named hybrid aligned if one substrate is homeotropic and the other is planar.

### 1.2.2 Anisotropic magnetic and electric properties

A proper description of some orientation dependent physical properties of nematics is given by symmetric tensors, similarly to uniaxial crystals:

$$\Psi = \begin{bmatrix} \Psi_{\perp} & 0 & 0 \\ 0 & \Psi_{\perp} & 0 \\ 0 & 0 & \Psi_{\parallel} \end{bmatrix}, \quad (1.2)$$

where  $\Psi$  denotes a general physical quantity that can be substituted by the following ones: relative dielectric permittivity ( $\varepsilon$ ), diamagnetic susceptibility ( $\chi$ ), electrical conductivity ( $\sigma$ ). In Eq. (1.2) the director orientation was chosen to be parallel to the  $z$ -axis. The indices ' $\perp$ ' and ' $\parallel$ ' show the orientations with respect to the director where the given quantity can be measured. For example if we measure the dielectric constant with an electric field parallel or perpendicular to the director, the resulting effective  $\varepsilon$  values will be  $\varepsilon_{\parallel}$  and  $\varepsilon_{\perp}$ , respectively. It is usual to define the so-called anisotropies of these quantities as:  $\Psi_a = \Psi_{\parallel} - \Psi_{\perp}$ , because in many cases not the actual values of  $\Psi_{\parallel}$  and  $\Psi_{\perp}$  are relevant but their difference. For example: the dielectric anisotropy ( $\varepsilon_a$ ), the diamagnetic susceptibility anisotropy ( $\chi_a$ ), electrical conductivity anisotropy ( $\sigma_a$ ), optical anisotropy ( $n_a$ ).

The rigid cores of the liquid crystal molecules usually consist of organic rings that are diamagnetic, thus  $\chi_{\perp}$  and  $\chi_{\parallel}$  are small negative numbers in the order of  $(-10^{-7}) - (-10^{-5})$ , however, the  $\chi_a$  magnetic anisotropy can be either positive or negative. In the case of compounds with aromatic rings,  $\chi_a$  is mostly positive. We note that there exist para- and ferromagnetic liquid crystals as well [11].

In the presence of a magnetic field  $\mathbf{H}$ , the induced magnetization is calculated by the magnetic susceptibility tensor  $\boldsymbol{\chi}$  as  $\mathbf{M} = \boldsymbol{\chi}\mathbf{H}$ . This latter expression can be rewritten to a form, which includes the director as follows:

$$\mathbf{M} = \chi_{\perp}\mathbf{H} + \chi_a\mathbf{n}(\mathbf{nH}). \quad (1.3)$$

In a deformed director field,  $\mathbf{M}$  can vary in the sample that changes  $\mathbf{H}$  also, since  $\mathbf{B} = \mu_0(\mathbf{M} + \mathbf{H})$  is constant if the external field is homogenous (because  $\nabla\mathbf{B} = 0$ ). Nevertheless the variation of  $\mathbf{H}$  is usually neglected, because the magnetic susceptibilities

are very small. With this assumption, the magnetic free energy density ( $f_{magn}$ ) of the LC is given by:

$$f_{magn} = - \int \mathbf{B} d\mathbf{H} = f_{magn}^0 - \frac{1}{2} \mu_0 \chi_a (\mathbf{n}\mathbf{H})^2 = f_{magn}^0 - \frac{1}{2} \frac{\chi_a}{\mu_0} (\mathbf{n}\mathbf{B})^2, \quad (1.4)$$

where  $f_{magn}^0$  is the director-independent magnetic free energy, and  $\mu_0$  is the vacuum permeability. Eq. (1.4) shows that for a material with positive (negative)  $\chi_a$ , it is energetically favorable to have the director parallel (perpendicular) to the magnetic field.

If the nematic material is exposed to an  $\mathbf{E}$  electric field, then a  $\mathbf{P} = \varepsilon_0 \boldsymbol{\chi}^e \mathbf{E} = \hat{\boldsymbol{\alpha}} \mathbf{E}$  polarization is induced, where  $\boldsymbol{\chi}^e$  and  $\hat{\boldsymbol{\alpha}}$  are the dielectric susceptibility and the macroscopic polarizability tensors, respectively. There can be contributions in the polarization from other origins (e.g. from flexoelectricity discussed later), however, those are neglected here for simplicity. Consequently, the electric displacement is given by  $\mathbf{D} = \varepsilon_0 \mathbf{E} + \mathbf{P} = \varepsilon_0 \boldsymbol{\varepsilon} \mathbf{E}$  which can be transformed to:

$$\mathbf{D} = \varepsilon_0 \varepsilon_{\perp} \mathbf{E} + \varepsilon_0 \varepsilon_a \mathbf{n}(\mathbf{n}\mathbf{E}). \quad (1.5)$$

Having a deformed director field,  $\mathbf{E}$  becomes inhomogeneous, since  $\nabla \mathbf{D} = 0$  has to be satisfied. Here we cannot neglect this inhomogeneity as we did in the magnetic case, because the values of  $\boldsymbol{\varepsilon}$  are in the order of 1-10.

The dielectric free energy density is:

$$f_{diel} = - \int \mathbf{D} d\mathbf{E} = f_{diel}^0 - \frac{1}{2} \varepsilon_0 \varepsilon_a (\mathbf{n}\mathbf{E})^2, \quad (1.6)$$

where  $f_{diel}^0$  is the director-independent electric free energy. Analogously to the case of magnetic field, the favorable director orientation with respect to the field is parallel and perpendicular for  $\varepsilon_a > 0$  and  $\varepsilon_a < 0$ , respectively.

The magnetic and electric field induced reorientation of the director is called Fredericksz-transition [2, 10]. Evidently the field induced director reorientation can occur in such geometries, where the field does not stabilize the initial director configuration. As an example let us consider a planar cell,  $\chi_a > 0$ , and an applied  $\mathbf{B}$  in the direction of the cell normal. Applying very high fields, the director is reoriented to a quasi-homeotropic configuration that means it is parallel with the field in the middle part of the cell. Since we have strong anchoring, the director remains planar at the sur-

faces, thus a strongly deformed zone can be found in the vicinity of the surfaces. The reorientation starts only above a well defined threshold field.

In general, for the different geometries, the magnetic inductance threshold  $B_{t0}$  is given by:

$$B_{t0} = \frac{\pi}{d} \sqrt{\frac{\mu_0 K_{ii}}{|\chi_a|}}, \quad (1.7)$$

where depending on the geometry,  $i$  can be 1, 2, or 3. In the electric case, the threshold is characterized by the voltage  $U_{t0}$ :

$$U_{t0} = \pi \sqrt{\frac{K_{ii}}{\varepsilon_0 |\varepsilon_a|}}. \quad (1.8)$$

An important difference is that  $U_{t0}$  does not depend on the cell thickness  $d$ , in contrast to the magnetic case.

We note that if a high frequency (e.g. 1 kHz) AC voltage is applied,  $U_{t0}$  corresponds to the rms voltage [10]. The details of Freedericksz-transitions in different geometries are discussed later in Sec. 3.2.

### 1.2.3 The flexoelectric effect

Due to symmetry reasons, nematics can obtain polarization from other than dielectric origin [2, 12, 13]. The flexoelectric effect is basically a splay and bend director deformation induced polarization defined as follows:

$$\mathbf{P}_f = e_1 \mathbf{n}(\nabla \mathbf{n}) + e_3 (\nabla \times \mathbf{n}) \times \mathbf{n}, \quad (1.9)$$

where  $e_1$  and  $e_3$  are the splay and bend flexoelectric coefficients, respectively. The effect is naively visualized in Fig. 1.6; it shows how one could expect a macroscopic polarization due to molecular interactions in the case of droplet and bent-shaped molecules. In Fig. 1.6(a) and (b), the director is homogeneous, thus the molecular dipole moments are randomly oriented, then there is no macroscopic polarization. If a splay or a bend deformation is present, the symmetry is broken because of molecular interactions, thus a flexoelectric polarization appears (see Fig. 1.6(c) and (d)).

Flexoelectricity is analogous with piezoelectricity that can be observed in solids [14]. The difference is that piezoelectricity is defined as a mechanical stress (mechanical strain)

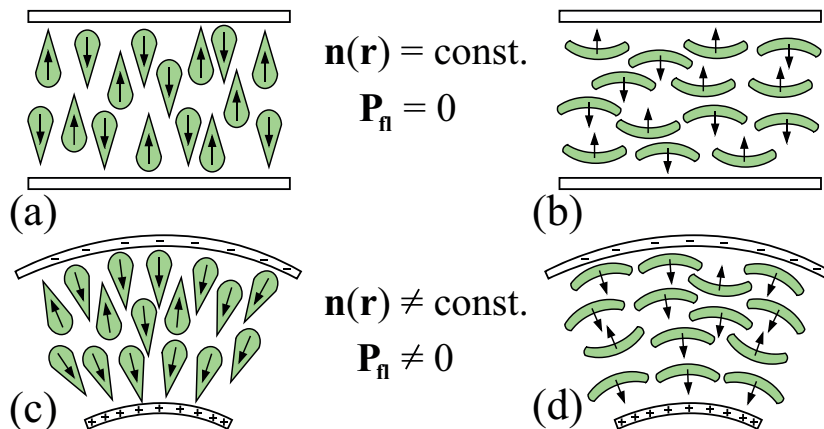


**Fig. 1.6:** A naive visualization of the flexoelectric effect. The molecular dipoles (arrows) are averaged out in a homogeneous director field for: (a) droplet-shaped, (b) bent-shaped molecules, since nematic is a non-polar phase. The dipole distribution is biased due to molecular interactions, if the director field is distorted by (c) splay, or (d) bend deformations. The generated flexoelectric polarization ( $\mathbf{P}_n$ ) is characterized by the splay ( $e_1$ ) and bend ( $e_3$ ) flexoelectric coefficients.

induced polarization, instead of orientational deformation induced polarization, which corresponds to the flexoelectricity in nematic LCs. Another important difference is that piezoelectricity appears in dielectrics with no inversion symmetry, in contrast to flexoelectricity, where there is no such requirement. We have to note that the terminology of flexoelectricity is also used in solid state physics for the phenomenon of the strain gradient induced polarization [14]. Flexoelectricity related effects in nematics are discussed in details in Sections 1.2.7, 2.1 and 2.2.

### 1.2.4 Dielectric behavior and molecular properties

In this section we show some aspects of how molecular properties affect the macroscopic electrical properties of a dielectric liquid. We consider first the case of isotropic materials [15].

In the presence of an external electric field ( $\mathbf{E}$ ), a macroscopic polarization ( $\mathbf{P} = \hat{\alpha}\mathbf{E}$ ) builds up in a dielectric liquid. The static polarizability can be split into two parts:  $\hat{\alpha} = \hat{\alpha}_e + \hat{\alpha}_o$ , where  $\hat{\alpha}_e$  and  $\hat{\alpha}_o$  refer to ionic-electronic and orientational polarizabilities, respectively. The electric field distorts the electron density distribution of a molecule creating an induced dipole moment. The magnitude of this effect is characterized by  $\hat{\alpha}_e$ .

Polar molecules also have permanent dipole moments  $\boldsymbol{\mu}$  that exist without the presence of any external electric field, however, due to thermal motion, they are randomly distributed, thus there is no detectable macroscopic polarization. After applying  $\mathbf{E}$ , the permanent dipoles tend to be aligned by the field giving the contribution of  $\hat{\alpha}_o$  in the total polarizability. Nevertheless the alignment has to be weak, since we consider linear effects with very low fields. It is rather a small biasing of the dipole moment distribution of molecules.

The Clausius-Mosotti equation connects the macroscopic dielectric constant  $\varepsilon$  to the molecular quantities of  $\hat{\alpha}_e$  and  $\boldsymbol{\mu}$  as follows [15]:

$$\frac{\varepsilon - 1}{\varepsilon + 2} = \frac{N}{3\varepsilon_0} \left( \hat{\alpha}_e + \frac{\boldsymbol{\mu}^2}{3k_B T} \right), \quad (1.10)$$

where  $N$  and  $k_B$  correspond to the number density of molecules and the Boltzmann-constant, respectively. We note that in order to derive Eq. (1.10), one has to take into account that the internal electric field acting on the molecules is different from what can be detected outside the sample.

The case of nematic liquid crystals is more complicated due to the reduced symmetry [11]. There are models that connect  $\varepsilon_{\perp}$  and  $\varepsilon_{\parallel}$  to molecular properties, but those include parameters that are hard to access experimentally, thus they are beyond our scope. Nevertheless, a useful expression to calculate  $\varepsilon_a$  from the Maier-Meier molecular theory is shown next [1, 11, 16]:

$$\varepsilon_a = \frac{NhFS}{\varepsilon_0} \left( \hat{\alpha}_{ea} + \frac{\boldsymbol{\mu}^2 F}{2k_B T} (3 \cos^2 \beta - 1) \right). \quad (1.11)$$

Here  $h$  and  $F$  are internal field correction factors,  $\hat{\alpha}_{ea} = \hat{\alpha}_{e\parallel} - \hat{\alpha}_{e\perp}$  is the anisotropy of the electronic-ionic polarization, and  $\beta_m$  is the angle between the dipole moment and the long molecular axis. Since  $\hat{\alpha}_{ea}$  is usually negligible, the sign of  $\varepsilon_a$  is determined by  $\beta_m$ . For values of  $\beta_m$  larger (smaller) than  $54.7^\circ$ , the dielectric anisotropy is expected to be negative (positive). For a given molecular structure,  $\beta_m$  can be determined from quantum-chemical methods as it will be presented in Sec. 4.1.4.

### 1.2.5 Dynamic dielectric properties

Applying alternating electric fields on isotropic fluids (or liquid crystals), the relative dielectric permittivity is frequency dependent since a macroscopic polarization does not build up in the material instantly [1]. The frequency dependence of  $\varepsilon$  can be relatively complex, because there are several processes included with different time constants. The emergence of the induced dipoles is very fast, the corresponding frequencies are in the optical range. Therefore at much lower frequencies, the induced dipoles can easily follow the field, thus they can contribute in  $\hat{\alpha}$ . At much higher frequencies, however, the measurable  $\varepsilon$  is decreased, because there is no time for the generation of the induced dipoles. At a specific intermediate resonance frequency, a phenomenon called dielectric resonance occurs, since the electron-ion system can be excited as an oscillator.

Dielectric relaxations are different; their characteristic frequencies are much lower as well. Due to the interaction of permanent dipoles, the electric field rotates the molecules or at least parts of them, thus this process is slower than the one discussed above. The time constant that characterizes the alignment is called the relaxation time ( $\tau_R$ ). The so-called relaxation frequency is defined as  $f_R = 1/(2\pi\tau_R)$ .

Let us consider the case where the static polarizability is built up by only one component, which originates from orientational polarizability. Thus in the static case, the polarization is given by

$$P_{max} = \chi^e(0)\varepsilon_0 E, \quad (1.12)$$

where  $\chi^e(0)$  means the static electrical susceptibility (at 0 frequency). We assume that if the polarization is perturbed, it relaxes back to  $P_{max}$  with the rate proportional to the deviation from the static value and inversely proportional to a constant relaxation time  $\tau_R$ . This yields a differential equation:

$$\frac{dP(t)}{dt} = \frac{P_{max} - P(t)}{\tau_R}. \quad (1.13)$$

Assuming that  $P(t=0) = 0$ , the solution is an exponential with  $\tau_R$  time constant:

$$P(t) = P_{max}(1 - e^{-t/\tau_R}). \quad (1.14)$$

The case of a harmonic alternating field is considered using the complex formalism  $E = E_0 e^{i\omega t}$ , where  $\omega$  corresponds to the angular frequency ( $\omega = 2\pi f$ ). Then the polarization is expressed by the frequency dependent complex susceptibility  $\chi^e(\omega)$ :

$$P = \chi^e(\omega) \varepsilon_0 E_0 e^{i\omega t}. \quad (1.15)$$

Combining eqs. (1.13), (1.12) and (1.15) leads to:

$$i\omega P = i\omega \chi^e(\omega) \varepsilon_0 E_0 e^{i\omega t} = \frac{\chi^e(0) \varepsilon_0 E_0 - \chi^e(\omega) \varepsilon_0 E_0}{\tau_R} e^{i\omega t}, \quad (1.16)$$

from where  $\chi^e(\omega)$  can be expressed as:

$$\chi^e(\omega) = \frac{\chi^e(0)}{1 + i\omega\tau_R}. \quad (1.17)$$

Equation (1.17) describes a so-called Debye-type relaxation. The background susceptibility that originates from other effects can be taken into account by adding  $\chi^e(\infty)$  to the righthand side of Eq. (1.17) and subtracting it from  $\chi^e(0)$ . The resulting expression can be converted to the complex dielectric constant ( $\varepsilon^*(f)$ ), which is usually used in an experimental approach to describe dielectric relaxation phenomena:

$$\varepsilon^*(f) = \varepsilon(\infty) + \frac{\Delta\varepsilon}{1 + i2\pi f\tau_R}, \quad (1.18)$$

where  $\Delta\varepsilon = \varepsilon(0) - \varepsilon(\infty)$  is the dielectric increment.  $\varepsilon^*(f)$  is split into its real and imaginary parts:

$$\varepsilon^*(f) = \varepsilon'(f) - i\varepsilon''(f), \quad (1.19)$$

where  $\varepsilon'(f)$  is the frequency dependent relative dielectric permittivity, and  $\varepsilon''(f)$  is the dielectric loss.

In summary, we can understand a dielectric relaxation as follows. Starting from the static case, the polarization and the dielectric constant are maximal ( $P_{max}$  and  $\varepsilon(0)$ ). Increasing the frequency, approaching  $f_R$ ,  $\varepsilon'$  is decreasing because there is less time to align the permanent dipoles perfectly, thus the contribution in the polarization will be lower. Simultaneously,  $\varepsilon''$  is increasing and it reaches its maximum at  $f_R$ , where the energy absorption (thus the dissipation) is the highest. We note that this effect (dielectric

heating) is used in microwave ovens, where the operating microwave frequency is tuned to the relaxation frequency of water. Further increasing the frequency, both  $\varepsilon'$  and  $\varepsilon''$  are decreasing until  $f$  is far enough from  $f_R$ , where they reach  $\varepsilon(\infty)$  and 0, respectively.

In practice we use an extended description for  $\varepsilon^*(f)$ , where  $k$  relaxations are assumed with different dielectric increments ( $\Delta\varepsilon_j$ ) and relaxation frequencies ( $f_{Rj}$ ):

$$\varepsilon^*(f) = \varepsilon(\infty) + \sum_{j=1}^k \frac{\Delta\varepsilon_j}{1 + i\left(\frac{f}{f_{Rj}}\right)^{1-\alpha_j}} - i\frac{\sigma}{\varepsilon_0 2\pi f}. \quad (1.20)$$

Here  $\varepsilon(\infty)$  is the high frequency limit of the relative dielectric permittivity, which contains all the contributions of effects that are much faster than the time resolution of the given study.  $\sigma$  is the DC conductivity that causes a  $1/f$  divergence in  $\varepsilon''$ . Based on the work of K. S. Cole and R. H. Cole [17], in Eq. (1.20) for each relaxation an  $\alpha_j$  symmetric distribution parameter is introduced that can have values from 0 to 1.  $\alpha = 0$  represents a simple Debye-type relaxation mode possessing a single characteristic time. On the contrary,  $\alpha \neq 0$  indicates a superposition of several processes with different, though close, characteristic times. In the latter case the relaxation is called Cole-Cole type. The expressions for  $\varepsilon'$  and  $\varepsilon''$  are given by:

$$\varepsilon'(f) = \varepsilon(\infty) + \sum_{j=1}^k \Delta\varepsilon_j \frac{1 + \left(\frac{f}{f_{Rj}}\right)^{1-\alpha_j} \sin\left(\frac{\alpha_j\pi}{2}\right)}{1 + 2\left(\frac{f}{f_{Rj}}\right)^{1-\alpha_j} \sin\left(\frac{\alpha_j\pi}{2}\right) + \left(\frac{f}{f_{Rj}}\right)^{2(1-\alpha_j)}}, \quad (1.21)$$

$$\varepsilon''(f) = \frac{\sigma}{\varepsilon_0 2\pi f} + \sum_{j=1}^k \Delta\varepsilon_j \frac{\left(\frac{f}{f_{Rj}}\right)^{1-\alpha_j} \cos\left(\frac{\alpha_j\pi}{2}\right)}{1 + 2\left(\frac{f}{f_{Rj}}\right)^{1-\alpha_j} \sin\left(\frac{\alpha_j\pi}{2}\right) + \left(\frac{f}{f_{Rj}}\right)^{2(1-\alpha_j)}}. \quad (1.22)$$

The usual representations of dielectric spectra are illustrated in Fig. 1.7(a) and (b). The data plotted were simulated using eqs.(1.21-1.22) with the parameter set:  $\varepsilon(\infty) = 3$ ,  $k = 2$ ,  $\Delta\varepsilon_1 = 2$ ,  $\Delta\varepsilon_2 = 2$ ,  $f_{R1} = 500$  kHz,  $f_{R2} = 500$  MHz,  $\alpha_1 = 0$ ,  $\alpha_2 = 0.3$ , and  $\sigma = 1$  nS/m. It can be well seen that the  $j$ th relaxation mode gives an increment to  $\varepsilon'$  equal to the corresponding  $\Delta\varepsilon_j$ . At the relaxation frequencies, an inflection and a peak can be found in  $\varepsilon'$  and in  $\varepsilon''$ , respectively. At high frequencies, the dielectric constant saturates to  $\varepsilon(\infty)$ . At lower frequencies in  $\varepsilon''$ , the divergence due to DC conductivity is seen. The height of a peak in the dielectric loss equals to the half of the dielectric increment if  $\alpha = 0$ . Otherwise the loss peak appears to be smaller and broader. In Fig. 1.7(b),  $\varepsilon''$  is depicted as the function of  $\varepsilon'$ , which is called the Cole-Cole plot. This is useful, because

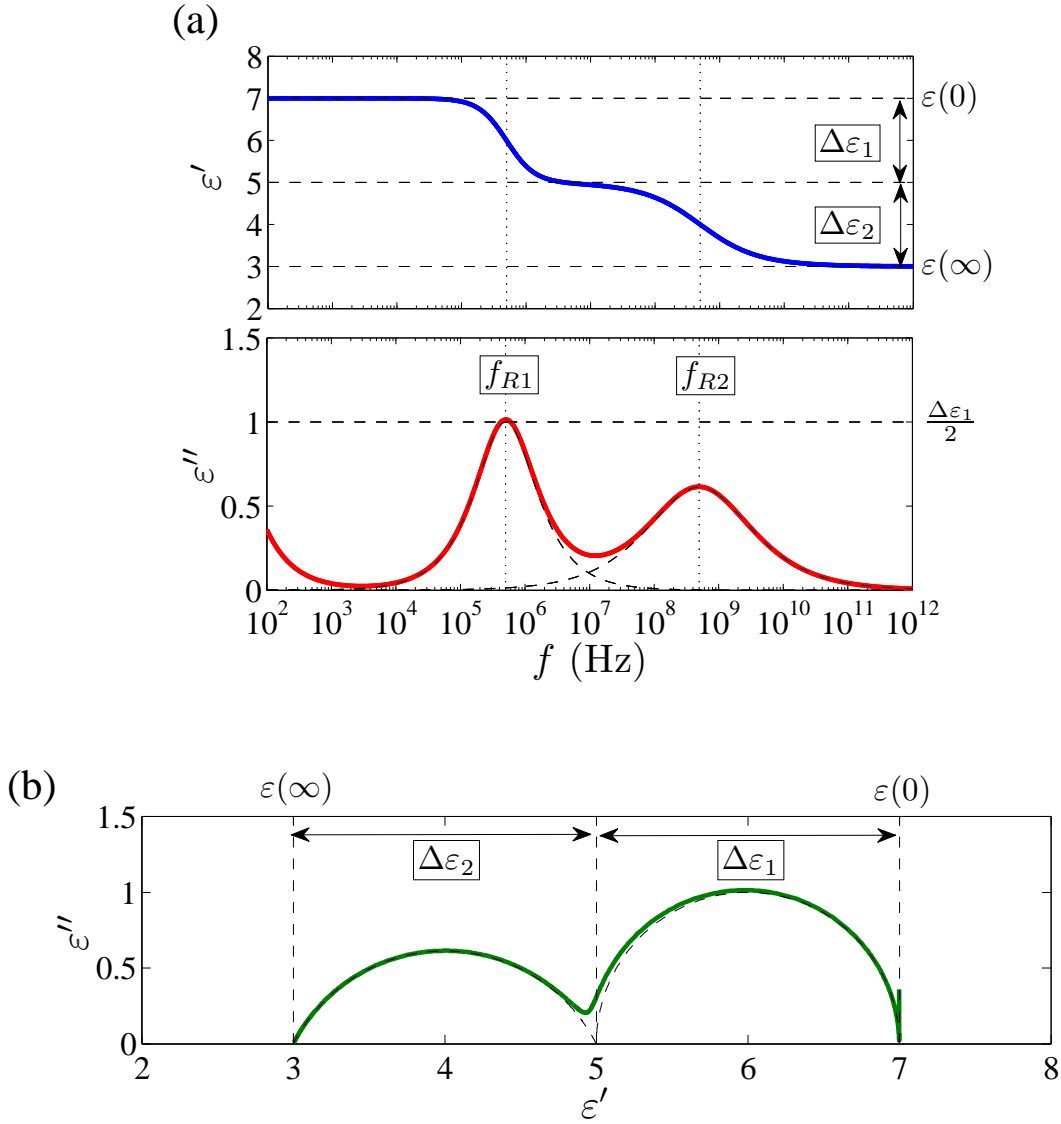


**Fig. 1.7:** Simulated dielectric spectrum with two relaxations and nonzero DC conductivity: (a) the frequency dependence of  $\epsilon'$  and  $\epsilon''$ , (b) the corresponding Cole-Cole plot. The relevant parameters can be found in the text.

it presents  $\epsilon'$  and  $\epsilon''$  together, furthermore it makes easier to distinguish Debye type and Cole-Cole type relaxations. In the Cole-Cole plot one relaxation appears as an arc of a circle. For a Debye-type one, the origin of the circle should be on the  $\epsilon'$ -axis, thus a half circle is visible. With increasing  $\alpha$ , however, the origin appears to be more below the  $\epsilon'$ -axis. We note that in the most general case, an additional so-called asymmetric distribution parameter can be introduced in the frame of the Havriliak-Negami description of dielectric relaxations [18] that has to be applied mostly to polymeric systems.

The theory for dielectric relaxations in isotropic polar liquids was derived by Debye assuming spherical molecules with non-interacting dipole moments [19]. This model predicts a single Debye type relaxation with the relaxation frequency

$$f_{Debye} = \frac{k_B T}{8\pi^2 r^3 \eta}, \quad (1.23)$$

where  $k_B$  is the Boltzmann constant,  $T$  is the absolute temperature,  $\eta$  is the viscosity, and  $r$  is the radius of the molecule. Though the predictions of this Debye-model fail quantitatively even for simple aromatic compounds [20], it shows the basic trends qualitatively well: larger molecules and/or higher viscosities are expected to reduce the relaxation frequency.

The dielectric increment in isotropic fluids is provided by the Onsager-formula [21] which also assumes spherical molecules with no dipolar interactions:

$$\Delta\varepsilon \frac{3\varepsilon(\infty) + 2\Delta\varepsilon}{(\varepsilon(\infty) + \Delta\varepsilon)(\varepsilon(\infty) + 2)^2} = \frac{N}{9\varepsilon_0 k_B T} \mu_{ons}^2, \quad (1.24)$$

where  $\mu_{ons}$  is the dipole moment of the molecule discussed in the frame of the Onsager-theory.

In the isotropic phase of liquid crystals mostly one Cole-Cole type relaxation can be found at high  $f$ , although there exist a few reports about two relaxations [22, 23] between 10 MHz and a few GHz. In practice Eq. (1.24) works well quantitatively for rod-like compounds with relatively weak dipoles [24], in spite of the anisotropic molecular shape and the assumption on the lack of interactions between dipole moments.

In the case of materials with large dipole moments, however, the Onsager-equation needs an improvement. Kirkwood and Fröhlich introduced a correction [15, 25] to Eq. (1.24) in the form

$$\mu_{ons}^2 = \mu^2 g, \quad (1.25)$$

where  $\mu$  is the real molecular dipole moment, and  $g$  is the factor that describes their interaction.  $g = 1$  (no interaction) stands in the isotropic phase of calamitic liquid crystals only for compounds with a relatively small  $\mu$ , while  $g < 1$  is valid for molecules with a large dipole moment along their long axis (e.g., cyano-biphenyls). This was interpreted as a short-range antiparallel ordering of neighboring dipoles leading to a reduction of the effective dipole moment compared to  $\mu$ .

In mesophases, the hindrances of molecular motions are anisotropic, therefore one can expect different dynamic dielectric properties than in the isotropic case. In rod-like nematics, there are usually three distinguishable relaxations: two in the parallel ( $\mathbf{E} \parallel \mathbf{n}$ ), and one in the perpendicular ( $\mathbf{E} \perp \mathbf{n}$ ) orientation [26].

The lowest frequency relaxation appears in the parallel component, and it is denoted by  $CM_{\parallel 1}$  ( $CM$  refers to calamitic-mode).  $CM_{\parallel 1}$  is purely Debye-type ( $\alpha = 0$ ) and corresponds to the rotation of the molecules around their short axis. The relaxation frequencies lie in a wide range between 10 kHz to 10 MHz depending on the temperature, the molecular and the bulk properties (e.g. molecular size, viscosity). The higher frequency relaxation in the parallel geometry ( $CM_{\parallel 2}$ ) is Cole-Cole-type ( $\alpha > 0$ ), and it can be connected to the rotational motions around the long axis of the molecule and around the director. Due to the much smaller hindrance of such movements,  $CM_{\parallel 2}$  occurs at much higher frequencies, between 100 MHz and 1 GHz. The  $f_R$  of the third relaxation ( $CM_{\perp}$ ) that can be detected in the perpendicular component, is usually close to  $f_{CM_{\parallel 2}}$ .  $CM_{\perp}$  is a composite (Cole-Cole) mode too, and it is interpreted also as the rotation of molecules around their long axis and around the director.

The three types of molecular motions can give different contributions to the dielectric increments of the distinct relaxations ( $CM_{\parallel 1}$ ,  $CM_{\parallel 2}$ ,  $CM_{\perp}$ ) depending on: 1) the magnitude of the permanent dipole moment, 2) the orientation of the permanent dipole with respect to the long molecular axis, and 3) the order parameter of the mesophase. The dielectric relaxations in calamitic compounds are well understood in the frame of a polar rod model, which assumes rigid molecules as uniaxial ellipsoids with a fixed dipole moment [23, 24, 27, 28, 29].

We have discussed non-collective molecular modes so far. In chiral smectic phases, however, two types of collective modes are additionally present [30] that are connected to synchronized motions of many molecules in contrast to non-collective modes. These processes are slower than the ones discussed above, due to their collective character.

In  $SmA^*$  and  $SmC^*$  phases, the so-called soft mode ( $SM$ ) can be observed that corresponds to the electric field induced biasing of the molecular tilt fluctuations in the smectic layers. The  $SM$  is especially strong in the  $SmA^*$  phase close to the second order transition to  $SmC^*$ , where the pretransitional tilt fluctuations are large. The corresponding  $f_R$  is between 10 kHz and 1 MHz.

The Goldstone-mode or helix distortion mode ( $HM$ ) originates from the interaction of the in-layer spontaneous polarization ( $\mathbf{P}_s$ ) with the electric field in the helical structure of  $SmC^*$  (Fig. 1.3). The field distorts the helix, because  $\mathbf{P}_s$  is bound to helical structure. Since here the whole helix is affected, the characteristic relaxation frequencies lie in the range: 100 Hz - 10 kHz, much lower than in the case of non-collective modes. The dielectric increment of the helix distortion mode can be very large, up to a few hundreds. Both the soft mode and the helix distortion mode can only be observed in the perpendicular geometry, where  $\mathbf{E} \perp \mathbf{n}$ .

Mode	Range of $f_R$	$\alpha$	Description	Type
$CM_{  2}$	100 MHz - 1GHz	$> 0$	reorientation around the long molecular axis and around the director	non-collective
$CM_{\perp}$	10 MHz - 1 GHz	$> 0$		
$CM_{  1}$	10 kHz - 10 MHz	0	reorientation around the short molecular axis	
$SM$	10 kHz - 1 MHz	$\gtrsim 0$	in-layer tilt angle fluctuations in $SmA^*$ and $SmC^*$	collective
$HM$	100 Hz - 10 kHz	$\gtrsim 0$	helix distortion by interaction with spontaneous polarization in $SmC^*$	

**Table 1.1:** Dielectrically active relaxation modes in nematics and chiral smectics.

Table 1.1 summarizes the main features of the dielectrically active non-collective and collective relaxation modes in calamitic nematic and smectic phases.

Since non-collective relaxation processes are connected to thermally activated fluctuations, the temperature dependence of the relaxation frequencies usually follow the Arrhenius-law:

$$f_R(T) = f_0 \exp\left\{-\frac{E_A}{k_B T}\right\}, \quad (1.26)$$

where  $f_0$  is a temperature independent constant and  $E_A$  is the activation energy of the relaxation. A higher  $E_A$  can refer to a greater hindrance of the molecular process behind the relaxation. The usual values for  $E_A$  lie in the range of electronvolts.

### 1.2.6 Optics of nematics

The optics of undistorted liquid single crystals is analogous to that of uniaxial single crystals. The optical properties are anisotropic, the two refractive indices are in connection with the relative dielectric permittivities considered at optical frequencies (here denoted as ' $\infty$ ') as follows:  $n_{\perp} = \sqrt{\varepsilon_{\perp}(\infty)}$  and  $n_{\parallel} = \sqrt{\varepsilon_{\parallel}(\infty)}$ . The perpendicular and parallel refractive indices are often called ordinary and extraordinary, respectively ( $n_{\perp} = n_o$  and  $n_{\parallel} = n_e$ ). The optical axis is defined as the direction where the light propagation is independent of the polarization of rays. In nematics, it coincides with the director.

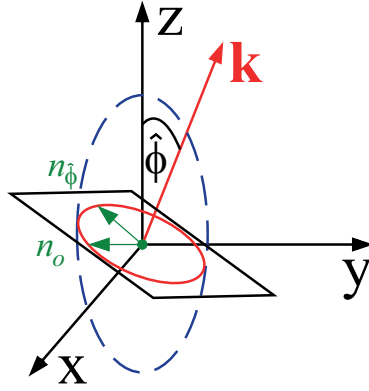


**Fig. 1.8:** The optical axis lies in the z-direction. A plane with the normal direction parallel to the wave vector of light ( $\mathbf{k}$ ) cuts the refractive index ellipsoid (dashed blue) in an ellipse (red). The principal axes of that ellipse are  $n_o$  and  $n_{\hat{\phi}}$  defined in Eq. (1.27).

Let us consider a ray of linearly polarized light propagating in a direction that is at an angle of  $\hat{\phi}$  with respect to the director. If  $\hat{\phi} \neq 0$ , the light can be split into two rays with perpendicular polarizations and different propagating velocities. This effect is called birefringence. The ordinary ray exhibits perpendicular polarization to the director, and its propagation velocity is  $c/n_o$ , independently from  $\hat{\phi}$ . The extraordinary component of light is polarized perpendicularly to the ordinary ray, and its speed equals to  $c/n_{\hat{\phi}}$ , where  $n_{\hat{\phi}}$  depends on  $\hat{\phi}$ . In the two limits, where  $\hat{\phi} = 0$  and  $\hat{\phi} = \pi/2$ ,  $n_{\hat{\phi}}$  equals to  $n_o$ , and  $n_e$ , respectively. In order to give the phase velocity of the extraordinary ray in general, we introduce the refractive index ellipsoid defined as  $x^2/n_o^2 + y^2/n_o^2 + z^2/n_e^2 = 1$ . The optical axis lies along the z-direction. The normal of the plane that crosses the origin represents the propagation direction ( $\mathbf{k}$ ) of our general linearly polarized light (Fig. 1.8).

The normal vector is at an angle of  $\hat{\phi}$  with respect to the z-axis as it was stated above. The cross-section of this plane and the refractive index ellipsoid is an ellipsis defined as:

$$\frac{1}{n_{\hat{\phi}}^2} = \frac{\cos^2 \hat{\phi}}{n_o^2} + \frac{\sin^2 \hat{\phi}}{n_e^2} \quad (1.27)$$

that can be used to determine  $n_{\hat{\phi}}$  as the function of  $\hat{\phi}$ .

Let us consider a planar cell that is illuminated by a linearly polarized monochromatic light beam propagating along the normal direction of the cell plane ( $\hat{\phi} = \pi/2$  case). The phase difference between the ordinary and extraordinary rays is given by:

$$\Delta\varphi_0 = \frac{2\pi}{\lambda} d n_a, \quad (1.28)$$

where  $\lambda$  is the wavelength of light,  $d$  is the cell thickness, and we used the definition of optical anisotropy, which is:  $n_a = n_e - n_o = n_{||} - n_{\perp}$ . For rod-like compounds,  $n_a$  is always positive and it lies usually in the interval between 0.01 and 0.3.

Describing the optics of liquid crystals in the presence of a deformed director field can be challenging. An important case of the continuous twist deformation can be analyzed by considering the polarized light propagation along the helix of a cholesteric liquid crystal. If the cholesteric pitch is much larger than the wavelength of the light, the polarization follows the rotation of the director. This phenomenon is referred to as adiabatic light propagation or Mauguin-effect [2]. Mathematically, the condition for the Mauguin-effect is satisfied if:  $\lambda \ll P n_a$ , where  $P$  is the cholesteric pitch.

Liquid crystals are widely used in optical devices such as displays. Maybe the most widespread display mode applies twisted nematic (TN) cell, where the director field is purely twist deformed (Fig. 1.9). In this case two polarizers are placed parallel with the rubbing directions for both surfaces. The incoming light is linearly polarized parallel with the director, and due to the Mauguin-effect, the polarization of light follows the director, rotates by  $90^\circ$  and passes the cell almost unaffected. The second polarizer then also allows the light to pass. Applying sufficiently high voltage on the cell, however, the director reorients inside forming an almost homeotropic configuration. Then the propagation direction of the incident light coincides with the optical axis, thus no light can pass the cell due to the crossed polarizers. We note that if a sample is studied

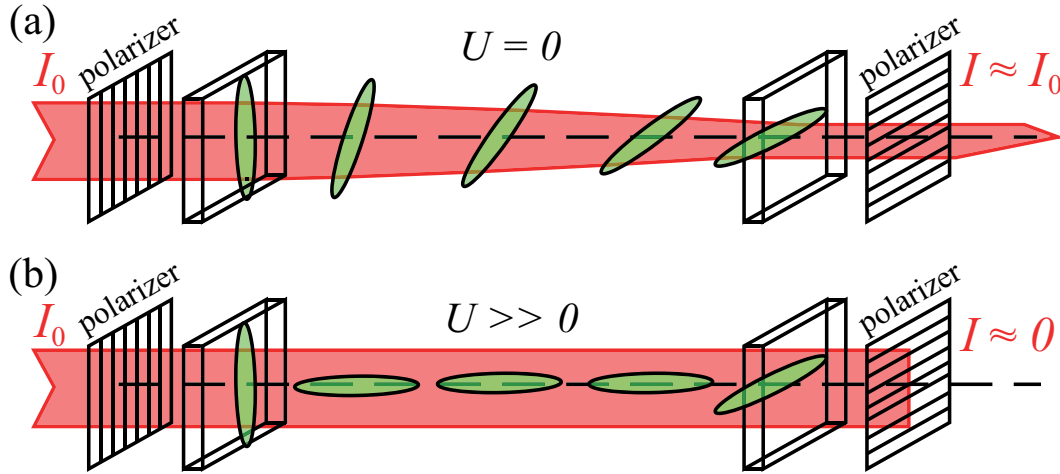


**Fig. 1.9:** The principle of the twisted nematic display mode. (a) With no applied voltage, the polarization of light follows the twisted director field and transmittance is maximal. (b) If the applied voltage is high enough, the director is switched to be parallel with the direction of the light propagation, thus the crossed polarizers do not let the light pass through.

between polarizers, the polarizer on the side of the light incidence is called polarizer, while the other is referred to as analyzer.

Liquid crystals are often used together with other optical elements such as polarizers, birefringent wave plates in various geometries. In order to investigate the response of optical systems, we introduce the versatile Mueller-matrix method [31, 32, 33] next.

A monochromatic ray of light propagating along the  $z$ -direction can be described by the  $x$  and  $y$  components of its electric field vector  $E_x(z, t) = E_{0x} \cos(kz - \omega t)$ ,  $E_y(z, t) = E_{0y} \cos(kz - \omega t + \delta)$ , respectively [32] ( $\omega$ ,  $k$ , and  $\delta$  are the angular frequency, the wave number and the phase difference, respectively.). The partially polarized light can be described by a four element Stokes-vector ( $\mathbf{s}$ ). The elements  $s_0$ ,  $s_1$ ,  $s_2$ ,  $s_3$  are constructed as follows:

$$\mathbf{s} = \begin{bmatrix} s_0 \\ s_1 \\ s_2 \\ s_3 \end{bmatrix} = \begin{bmatrix} E_{0x}^2 + E_{0y}^2 \\ E_{0x}^2 - E_{0y}^2 \\ 2E_{0x}E_{0y} \cos \delta \\ 2E_{0x}E_{0y} \sin \delta \end{bmatrix} \quad (1.29)$$

It is important to note that the light intensity is given by  $s_0$ . For example the Stokes-vector for linearly polarized light in the  $x$ -direction with the total intensity  $I_0$  is described by:  $s_0 = I_0$ ,  $s_1 = I_0$ ,  $s_2 = 0$ , and  $s_3 = 0$ . The effect of an optical element on the incoming

light is characterized by a specific Mueller-matrix. The light transmittance can then be calculated by matrix multiplication.

As an example, the transmittance characteristics of a rotated planar liquid crystal cell between crossed polarizers is calculated below. The monochromatic light propagates along the z-axis, parallel with the normal direction of the cell. The director is at an angle of  $\phi$  with respect to the x-axis. The planar cell performs a  $\Delta\varphi$  retardation as it was discussed above (Eq. (1.28)), thus it can be considered as a waveplate. The Mueller-matrix of a waveplate performing  $\Delta\varphi$  retardation and having its slow axis at an angle of  $\phi$  with respect to the x-axis is denoted as  $\mathbf{M}_{wp}(\phi, \Delta\varphi)$ . In order to perform the calculations, we also need the Mueller-matrix for a polarizer that has its polarizing axis at a  $\zeta$  angle with respect to the x-axis  $\mathbf{M}_{pol}(\zeta)$ :

$$\mathbf{M}_{wp}(\phi, \Delta\varphi) = \begin{bmatrix} 1 & 0 & 0 & 0 \\ 0 & \cos^2 2\phi + \cos \Delta\varphi \sin^2 2\phi & (1 - \cos \Delta\varphi) \sin 2\phi \cos 2\phi & \sin \Delta\varphi \sin 2\phi \\ 0 & (1 - \cos \Delta\varphi) \sin 2\phi \cos 2\phi & \sin^2 2\phi + \cos \Delta\varphi \sin^2 2\phi & -\sin \Delta\varphi \cos 2\phi \\ 0 & -\sin \Delta\varphi \sin 2\phi & \sin \Delta\varphi \cos 2\phi & \cos \Delta\varphi \end{bmatrix}$$

$$\mathbf{M}_{pol}(\zeta) = \frac{1}{2} \begin{bmatrix} 1 & \cos 2\zeta & \sin 2\zeta & 0 \\ \cos 2\zeta & \cos^2 2\zeta & \sin 2\zeta \cos 2\zeta & 0 \\ \sin 2\zeta & \sin 2\zeta \cos 2\zeta & \sin^2 2\zeta & 0 \\ 0 & 0 & 0 & 0 \end{bmatrix} \quad (1.30)$$

The Stokes-vector of the ingoing ray ( $\mathbf{s}_{in}$ ) of intensity  $I_0$  is set to be linearly polarized in the x-direction. The transmitted light ( $\mathbf{s}_{out}$ ) is calculated as:

$$\mathbf{s}_{out} = \mathbf{M}_{pol}(\pi/2)\mathbf{M}_{wp}(\phi, \Delta\varphi)\mathbf{M}_{pol}(0)\mathbf{s}_{in} \quad (1.31)$$

After straightforward calculations, the 0-th element of  $\mathbf{s}_{out}$  is given by:

$$I = I_0 \sin^2(2\phi) \sin^2(\Delta\varphi/2). \quad (1.32)$$

Liquid crystals are often studied using a polarizing microscope in transmittance mode. It is crucial to check the director orientation, which can be done by rotating the sample between crossed polarizers. In such experiments, Eq. (1.32) is used. If the quality of

the orientation is good, then the transmitted intensity should be zero if the director is parallel with one polarizer axis ( $\phi = 0$  or  $\phi = \pi/2$ ). Furthermore if  $\Delta\varphi$  is not equal to an integral multiple of  $\pi$ , one should get the maximum transmittance if the director is adjusted to  $\phi = \pi/4$ . If  $\Delta\varphi$  is changing at a given cell position, the transmitted intensity oscillates, or the apparent color of the cell is varying in the case when white light illumination is used instead of monochromatic. Such effects can be observed by changing the temperature since  $\Delta\varphi$  is proportional to  $n_a$  which is roughly proportional to the order parameter  $S$ .

One can also affect  $\Delta\varphi$  by inducing a Fredericksz-transition using electric and/or magnetic fields in proper geometries. In a geometry where the field reorients the director from a planar to a quasi-homeotropic state, the initial  $\Delta\varphi$  reduces to zero gradually with increasing fields. Thus the transmittance will oscillate as the function of the field above the Fredericksz-threshold and finally at high fields, where the sample can be considered as homeotropic, it goes to zero. The optics of Fredericksz-transitions will be discussed in detail in Sec. 3.2.

### 1.2.7 Pattern formation in nematics

Numerous different types of spatially inhomogeneous structures (patterns) can be formed in liquid crystals if they are driven far from the equilibrium state. The driving forces can be among others: temperature, pressure or concentration gradients, and magnetic or electric fields. Some of the pattern forming mechanisms are specific for only liquid crystals, because they require anisotropy, while others can be observed in isotropic fluids as well.

Hereunder we consider only electric field driven patterns in nematics. The main control parameters in this case are the frequency and the magnitude of the applied voltage. Applying electric field on a planar liquid crystal cell often leads to the appearance of spatially periodic stripe patterns [2, 34, 35, 36, 37]. These patterns exhibit a large variety in their morphologies that can be characterized by the magnitude and the direction of their specific wave vectors.

The standard electro-hydrodynamic instability or electroconvection (EC) is one AC electric field driven mechanism that leads to the appearance of perpendicular (or oblique) stripes with respect to the rubbing direction in a planar cell. EC is observed mostly in

systems with positive conductivity anisotropy ( $\sigma_a > 0$ ) and negative dielectric anisotropy ( $\epsilon_a < 0$ ). In such case, the applied voltage is expected to stabilize the initial homogeneous planar state according to Eq. (1.6). Interestingly, above a critical threshold voltage ( $U_c$ ) the homogeneous state becomes destabilized and a periodic convection roll structure emerges where the director is modulated.

This effect can be observed in a microscope between crossed polarizers, since the director modulation changes the birefringence that leads to intensity modulation. Moreover an other so-called shadowgraph-effect is also present that makes the pattern observation possible even without any polarizers [38]. The shadowgraph-effect is based on the focusing-defocusing of light due to the refractive index gradients induced by the director modulation. Similarly to the mirage phenomenon, a light ray bends towards the larger refractive index while it passes the medium with a refractive index gradient.

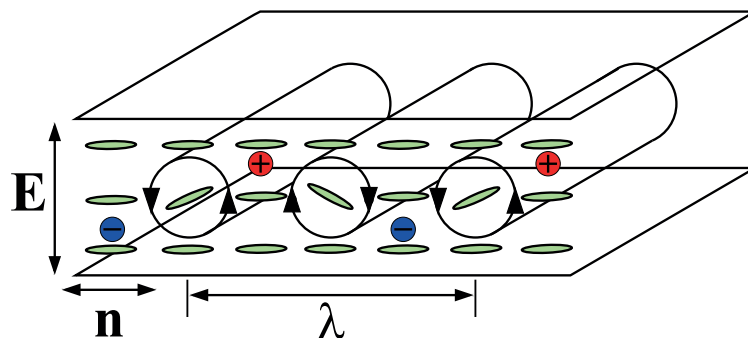


**Fig. 1.10:** A cartoon of the Carr-Helfrich mechanism for the electro-hydrodynamic instability in nematic liquid crystals.

The standard EC effect in nematics is explained by the so-called Carr-Helfrich mechanism [39, 40, 41] presented next as a scenario for the emergence of director destabilizing torques (Fig. 1.10). Due to  $\sigma_a > 0$ , the current assumed to be ohmic is not parallel with  $\mathbf{E}$ , wherever the director is not exactly perpendicular to the field. Such director tilt takes place spontaneously because of thermal fluctuations. Then charge separation occurs due to the current in the plane of the cell. The electric field of the resulting space charges decreases the director stabilizing torque of the external field. Furthermore the external field exerts a force on the charges, which induces viscous vortex flow in the sample. The flow aligns the director, which can further increase the director tilt leading to the formation of a periodic pattern. On the other hand, a stabilizing torque arises from the increased elastic energy of the deformed director and the dissipative viscous torques

are also against the deformation. At small applied voltages the stabilizing torques are stronger, thus the director fluctuations are suppressed. Above a well defined  $U_c$  threshold voltage, however, the destabilizing torques are dominant, thus a pattern can emerge.

The theoretical description of electroconvection induced by the Carr-Helfrich mechanism is in good agreement with the experiments. It was shown that the threshold voltage ( $U_c$ ) and the characteristic wave number of the pattern at the threshold ( $q_c$ ) are important parameters that strongly depend on the frequency of the driving voltage. A typical  $f$ -dependence of  $U_c$  is presented in Fig. 1.11 [37]. The solution of nemato-electrohydrodynamical equations revealed that two distinct regimes of EC exist with different time symmetries [34, 42]. The so-called conductive mode is observed at lower frequencies, where the space charges are oscillating with the driving voltage while the director field is nearly constant in time. In contrary, the so-called dielectric mode exhibits oscillating director field and nearly constant space charge distribution at higher frequencies. The difference between conductive and dielectric modes can be formulated more precisely if we consider the temporal behavior of the relevant director component  $n_z$  that is parallel with the electric field. The time average over a driving period is nonzero in the conductive mode ( $\langle n_z(t) \rangle \neq 0$ ), but it vanishes in the dielectric regime ( $\langle n_z(t) \rangle = 0$ ).

As a consequence of the time symmetries in the dielectric regime, the system has to go through the undistorted state twice in a driving period. In the conductive mode, however, the pattern should remain all the time, only small higher-harmonic oscillations are allowed for  $n_z$  around a constant value. This behavior of the different EC regimes were proven experimentally by time-dependent studies of light diffraction [43] and optical microscopy with high temporal resolution [44, 45, 46, 47].

It was shown that the  $f$ -dependent  $U_c$  curves of the different modes intersect at the so-called crossover-frequency  $f_c$ . In practice, that mode can be observed, which has the lower threshold voltage, therefore a transition between conductive and dielectric EC rolls can be seen at  $f_c$ .

The convection rolls in both regimes are perpendicular to the rubbing direction, if the driving  $f$  is higher than the so-called Lifshitz-frequency ( $f_{Lif}$ ) that mostly lies under  $f_c$ . The pattern is called dielectric (Fig.1.12(c)) and normal rolls (Fig.1.12(b)), in the dielectric and the conductive regimes, respectively. A distinctive feature of dielectric rolls is that their characteristic wavelength (wave number) is predominantly smaller (larger)

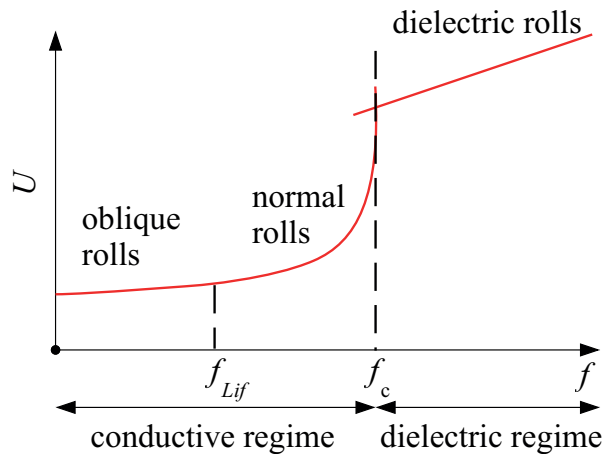


**Fig. 1.11:** A typical frequency dependence of the threshold voltages of standard electroconvection [37]. The conductive and dielectric regimes are separated by the crossover-frequency ( $f_c$ ). The transition between oblique and normal rolls is characterized by the Lifshitz-frequency ( $f_{Lif}$ ).

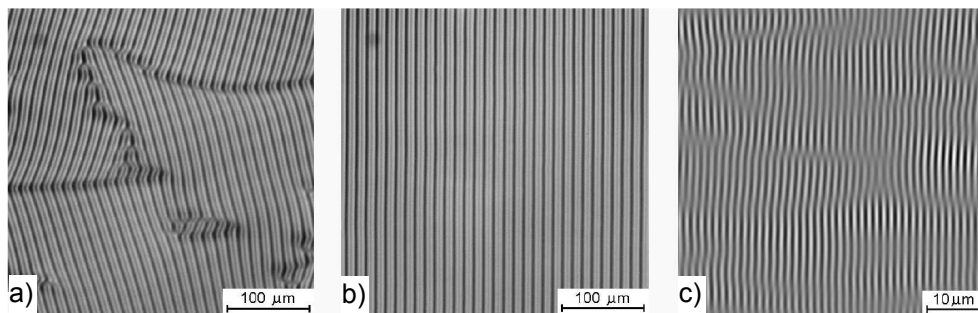


**Fig. 1.12:** Typical snapshots of electroconvection patterns close to the threshold taken by shadowgraph technique: a) oblique rolls, b) normal rolls, c) dielectric rolls. The director lies in the horizontal direction. Phase 5 nematic mixture was used in a  $9 \mu\text{m}$  thick planar cell [37].

than that of conductive normal rolls and is not scaling with the cell thickness. Below  $f_{Lif}$ , the rolls become gradually tilted with respect to the normal roll direction (Fig.1.12(a)). Since the tilting is degenerate, the resulting pattern has a zig-zag structure, often called oblique rolls.

The typical studied  $f$  range of standard EC lies from 10 Hz to a few kHz.  $f_c$  can vary in the whole range, depending on material parameters, especially on the conductivity. An increase of conductivity makes  $f_c$  larger. EC is a complex phenomenon including

several processes that can be characterized by different time constants. The slowest and maybe the most important is called the director relaxation time defined as follows:

$$\tau_d = \frac{\gamma_1 d^2}{K_{11} \pi^2}, \quad (1.33)$$

where  $\gamma_1$  is the rotational viscosity.  $\tau_d$  is approximately the time until the director relaxes back to the equilibrium planar state from a quasi-homeotropic deformed configuration. It was shown that the growth and decay times of EC are in the order of  $\tau_d$  [48, 49]. We notice that  $\tau_d$  is proportional to the square of the cell thickness, and it is important in all phenomena with director dynamics. Usually much faster is the charge relaxation, characterized by its relaxation time:  $\tau_q = \frac{\varepsilon_0 \varepsilon_{\perp}}{\sigma_{\perp}}$ . The shortest relaxation time is the viscous one:  $\tau_v = \frac{\rho d^2}{\tilde{\alpha}_4/2}$ , where  $\rho$  is the density and  $\tilde{\alpha}_4/2$  is the isotropic viscosity. Another natural characteristic time is the period of the AC driving defined as  $\tau = 1/f$ . For example in the case of a 20  $\mu\text{m}$  thick cell with a regular rod-like nematic, the corresponding values for  $\tau_d$ ,  $\tau_q$ ,  $\tau_v$ , are 0.5 s,  $6 \times 10^{-4}$  s, and  $1 \times 10^{-5}$  s [50]. Therefore typically  $\tau_d \gg \tau \gg \tau_q \gg \tau_v$  holds.

Nevertheless there are several electric field induced convective patterns that cannot be explained by the classical standard model discussed above. Occasionally, compounds with  $\varepsilon_a < 0$ ,  $\sigma_a < 0$  (or with  $\varepsilon_a > 0$ ,  $\sigma_a > 0$ ) also show so-called nonstandard electroconvection phenomena. In the case with negative anisotropies one can observe rolls parallel to the rubbing direction. This effect was understood recently [50] by taking into account flexoelectricity in the theory of standard electroconvection, where the charge separation is due to the flexoelectric polarization instead of  $\sigma_a$ . There are still many open questions in this field, for example: the mechanism for cellular and normal roll pattern formation for compounds with positive  $\varepsilon_a$  and  $\sigma_a$  is still unknown [51]. There are the so-called prewavy patterns that appear as large wavelength normal rolls in some calamitic and bent-core nematic mesogens, and their existence is still not explained [52].

A completely different type of pattern forming phenomenon is the flexoelectric instability. The resulting patterns are called Bobylev-Vistin-Pikin domains or simply flexodomains (FDs) [36, 53, 54, 55, 56]. The flexoelectric instability involves a static, spatially periodic director modulation where there is no flow, thus the formation of FDs is a non-dissipative process. The resulting stripes are parallel with the initial director in a

planar cell (Fig. 1.13(a)). Nevertheless FDs can be distinguished from the parallel rolls of nonstandard EC by their static character.

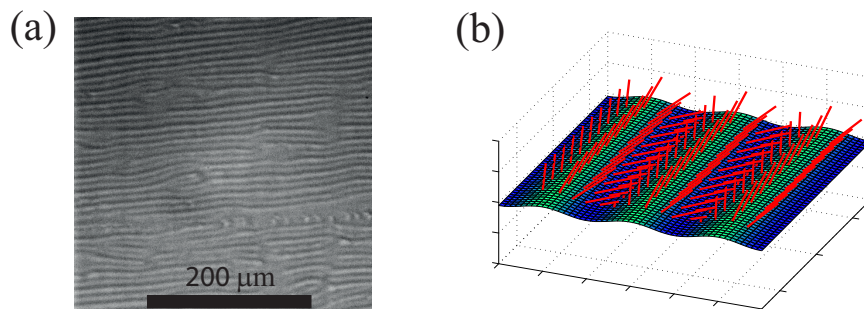


**Fig. 1.13:** A typical shadowgraph image of flexodomains: (a) Phase 5 nematic mixture in a  $11 \mu\text{m}$  thick planar cell [P5]. The director lies approximately horizontally. (b) The three dimensional director profile of flexodomains. The local director is symbolized by red rods.

The theoretical description of FDs is much easier than that of EC. The deformation profile and threshold characteristics of FDs can be obtained by free energy minimization, due to the lack of flow. It has first been shown by Bobylev and Pikin [36, 54] using a one-elastic-constant approximation ( $K = K_{11} = K_{22}$ ) and DC driving, that flexoelectricity is responsible for the appearance of FDs. The periodic director deformation includes here not just director tilt, but twist modulation as well (Fig. 1.13(b)). The formulas for the threshold voltage  $U_{FD}$  and the critical wave number  $q_{FD}$  of the pattern can be given analytically:

$$U_{FD} = \frac{2\pi K}{|e_1 - e_3|(1 + \mu_{FD})}, \quad (1.34)$$

$$q_{FD} = \frac{\pi}{d} \sqrt{\frac{1 - \mu_{FD}}{1 + \mu_{FD}}}, \quad (1.35)$$

where

$$\mu_{FD} = \frac{\varepsilon_0 \varepsilon_a K}{|e_1 - e_3|^2}. \quad (1.36)$$

According to Eq. (1.35), the flexodomains can only appear, if  $|\mu_{FD}| < 1$ , which leads to the requirement  $|\varepsilon_a| < |e_1 - e_3|^2 / (\varepsilon_0 K)$  that should hold for liquid crystals showing FDs.

The description with one-constant approximation has recently been extended taking into account the anisotropy of elasticity and AC driving [57]. Beyond its own scien-

tific interest, flexodomains can also be used to access the combination of flexoelectric parameters ( $|e_1 - e_3|$ ), which is a quite challenging experimental task in general [13].

## 2. Objectives

### 2.1 Bent-core nematic liquid crystals

In Sec. 1.1.2, we presented that bent-core mesogens are special because they form a distinct class of mesophases (B-phases) with unique ordering and symmetries that are characteristic only for liquid crystals consisting of bent-shaped molecules. Bent-core molecules can also form nematic phase (BCN), however, that is rare compared to the nematic (N) phase of the rod-like molecules. This could be explained by that the bent shape is not really compatible with the translational freedom of the nematic phase.

The evident difference between rod-like and bent-core mesogens lies in their symmetry. Rod-like compounds can well be approximated by elongated ellipsoids of revolution. Considering the molecules as such uniaxial objects worked successfully in molecular theories of nematics. Nevertheless bent-cores are different. Their molecular symmetry is reduced compared to that of calamitics, namely BC molecules are biaxial. The bulk symmetry of BCNs, however, remains uniaxial, therefore one would not expect qualitative differences between rod-like and bent-core nematics. An interesting question is then, how the bent-shape of the molecules influences the bulk nematic properties quantitatively?

Compared to rod-like nematics, large quantitative differences in the basic bulk properties (e.g. elastic constants, viscosities) could lead to qualitatively different behavior in complex phenomena, such as pattern formation. Another question is what kind of new effects could be possible with bent-cores that were not observable with calamitics due to the different ranges of material parameters?

The first BCNs were found in 1999 [58], however, the clearing points were too high ( $T_{NI} \gtrsim 200^\circ\text{C}$ ) to conveniently study their physical properties. The most widely studied BCN, the CIPbis10BB was synthesized later in 2002 [59]. The nematic temperature range of that compound was found well below  $100^\circ\text{C}$ , and due to its stability, CIPbis10BB became a representative compound for bent-core mesogens. A significant part of our

studies was also performed on this material. The molecular structure and the basic properties will be shown later in Sec. 3.1.2. In the following paragraphs we summarize the main findings on bent-core nematics that were known before our studies.

One could think first that there is an obvious difference in flexoelectricity between rod-like and bent-core LCs. According to Sec. 1.2.3, a larger bend flexoelectric coefficient ( $e_3$ ) can be expected for bent-cores. Actually in 2006, 'giant flexoelectricity' was found by Harden et. al. [60] in CIPbis10BB. The direct technique to determine flexoelectric coefficients was based on the measurement of (flexo)electric current on a periodically deformed flexible cell. Measurements on a basic rod-like compound (5CB) were also done for comparison, and a three orders of magnitude larger  $|e_3|$  was found in the bent-core liquid crystal. Similar results were obtained by the converse experiment, where the mechanical distortion of a flexible cell was measured as the function of applied voltage [61]. Above a threshold voltage, the giant flexoelectricity appeared here as well.

Molecular statistical models [62, 63] of bent-cores, however, could not explain such high  $|e_3|$  values in the frame of regular nematic flexoelectricity illustrated in Sec. 1.2.3. An alternative explanation argued with the effect of polar molecular clusters (or cybotactic groups) in the nematic matrix, proposed by previous studies of nuclear magnetic resonance (NMR) [64], dynamic light scattering [65], and small angle X-ray scattering [66]. The origin of these nano-scale objects was attributed to the strong short range polar ordering of bent-core molecules. The clusters constructed by few tens of molecules were assumed to be randomly dispersed in the nematic and even in the isotropic phase. The proposed structure of the smectic clusters is illustrated in Fig. 2.1 (from Antal Jáklí [P4]).

The giant flexoelectricity could not be reproduced so far, since the indirect electro-optical methods [67, 68] gave the regular order of magnitude for flexoelectric parameters in bent-cores. It is still not clarified, why could one get giant effect only if the direct/converse mechanical flexing technique is used. A more detailed discussion about this effect is presented later in Chapter 5.

Other extraordinary features of bent-cores such as very high flow induced birefringence [69], large Kerr-effect [70], and unusual rheological properties [71] were also explained by the presence of molecular clusters with higher order, not only in the nematic

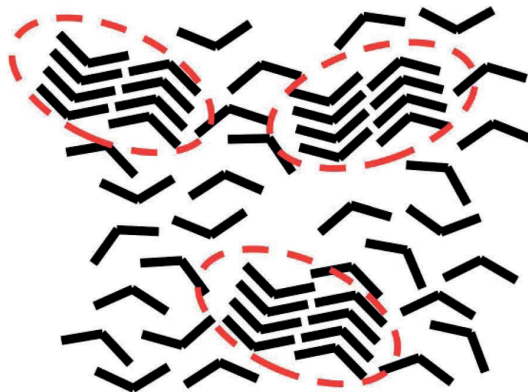


**Fig. 2.1:** The proposed structure of the smectic clusters (marked by dashed ellipses) in a bent-core nematic liquid crystal (from Antal Jáklí [P4]).

but in the isotropic phase as well. The most recent findings on these clusters are presented later in Chapters 4 and 5.

BCs exhibit electric field induced convective patterns [52, 72, 73, 74] that cannot be explained by the standard Carr-Helfrich mechanism (see Sec. 1.2.7). In CIPbis10BB [52], four distinct regimes were found in the studied frequency range including an intermediate frequency gap (bordered by threshold voltage divergences), where no patterns were visible at all. Furthermore  $\sigma_a$  was found to change its sign twice below 100 kHz that could refer to a dielectric loss peak, since  $\sigma(f)$  is proportional to  $\varepsilon''(f)$ . The direct motivation of our dielectric studies of bent-cores was to investigate this possible dielectric relaxation at such unusually low frequencies. Furthermore, no previous studies were done on BCNs before that also encouraged us to perform the dielectric spectroscopy measurements [P1, P4]. We also investigated the dielectric behavior of a number of rod-like - bent-core mixtures with different concentrations, in order to have the chance to see the possible gradual changes of dielectric parameters from the characteristics of the unknown bent-core to that of the regular rod-like. Our results corresponding to frequency dependent dielectric phenomena are presented in Sec. 4.1.

After it became clear that bent-core nematics exhibit extraordinary properties compared to calamitics, the need of exploring basic material properties such as elastic constants has arisen. Previous electro-optical studies demonstrated that in certain BCNs, the ratio of the splay ( $K_{11}$ ) and bend ( $K_{33}$ ) elastic constants is reversed [75] compared to that of rod-like nematics, where  $K_{11}$  is smaller than  $K_{33}$ , except in the immediate vicinity of a nematic-smectic transition (if such exists). The temperature dependences of

the splay and bend elastic constants were also shown to be anomalous [76]. The analysis of transient defect walls in a BCN [77] showed that the twist elastic constant  $K_{22}$  can be an order of magnitude smaller than  $K_{33}$  that could not be observed in rod-like nematics before.

Nevertheless there were no studies before our work that gave the actual values of all individual elastic constants for a bent-core nematic mesogen. Furthermore, no adequate models were presented that would have explained the anomalous elasticity of BCNs. These above facts motivated us to perform comprehensive studies of elastic constants using ClPbis10BB [P2, P4]. Later, in order to broaden our studies and to check the universality of our findings, we have performed similar measurements [P3] on a different type of bent-core compound (DT6PY6E6). On that occasion, we have found a new way to determine  $K_{22}$ . Then the optical and dielectric behavior of our experiments were simulated in order to achieve a deeper understanding of those systems. Our findings that correspond to the elasticity of bent-core nematics are presented in Sec. 4.2.

## 2.2 Ultra-low frequency pattern formation

The basic properties of electroconvection and flexodomains were presented in Sec. 1.2.7. In 2008, experimental studies [78] were extended to the unexplored low-frequency range, where the director relaxation time was smaller than the period of the driving ( $\tau_d < \tau$  - see Sec. 1.2.7). It has turned out that EC appears as flashes that are much shorter than  $\tau$ , if  $f$  is much below 1 Hz. Furthermore, at specific combinations of voltage and frequency, an alternation of EC and FD flashes were also found. Nevertheless, in these studies only the dielectric regime of EC could be investigated, because of the specific material parameters of the studied compound.

We thought that it would be interesting to see the low frequency behavior of EC in the conductive mode, because then a transition could possibly be followed from a stationary pattern state to a flashing regime by decreasing the frequency. That could not be studied in the case of dielectric EC, where the pattern disappears twice in a driving period even at high frequencies, due to the oscillating contrast characteristics originating from the time symmetry of the dielectric mode.

The standard model of EC was extended recently to the regime of  $\tau_d < \tau$ , and a theory for FDs was created that accounts for the anisotropy of elasticity ( $K_{11} \neq K_{22}$ ) and AC driving [57]. The novel theoretical findings were experimentally untested, thus they served also as motivations for our experimental work [P5-P7] in the subject of ultra-low frequency pattern formation.

The novel theory of FDs provided a tool that made an opportunity to determine the flexoelectric parameter  $|e_1 - e_3|$  from the threshold parameters  $(q_c, U_c)$  more precisely than it was possible with the one-elastic-constant approximation before. In such way, a new reliable method became available to compare the flexoelectricity of rod-like and bent-core nematic liquid crystals that could be a valuable scientific result, since there are many open questions in this topic as it was shown above.

## 3. Materials and techniques

### 3.1 Dielectric studies

The practical goal of the dielectric measurements is to determine the real and imaginary parts of the complex relative dielectric permittivity  $\varepsilon^*$ . If the studies concentrate on the frequency dependence of the dielectric parameters, the technique is called dielectric spectroscopy. In Sec. 3.1.1, we present the principle, the practical aspects, and the actually applied experimental setup. Then in Sec. 3.1.2, the substances used for dielectric spectroscopy studies are shown.

#### 3.1.1 Measurement technique

Liquid crystals are usually studied in sandwich cells with transparent indium-tin-oxide (ITO) electrodes. Such a sandwich cell can be considered as a parallel-plate capacitor with a capacitance  $C_0$  connected in series with a resistor  $R_{ITO}$  that corresponds to the resistance of the ITO electrodes. In the most realistic picture, the resistance and capacitance of the alignment layers ( $R_p$  and  $C_p$ ) can be also considered as a parallel RC-term (Fig. 3.1(a)). The empty cell capacitance is determined by the electrode area

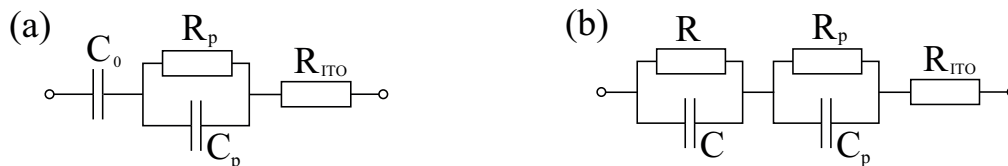


**Fig. 3.1:** The equivalent circuit models for: (a) empty, (b) filled liquid crystal sandwich cells with ITO electrodes.

$A$  and the cell thickness  $d$ :  $C_0 = \varepsilon_0 \frac{A}{d}$ . If the cell is filled with liquid crystal, the equivalent circuit is different (Fig. 3.1(b)); namely  $C_0$  is replaced by a parallel RC-term (with a resistance  $R$  and a capacitance  $C$ ). This substitution is due to the finite conductivity and the different dielectric constant of the material. The parameters  $R$  and  $C$  are frequency

and temperature dependent. The dielectric constant  $\varepsilon'$  and the dielectric loss  $\varepsilon''$  at a given frequency can be calculated as follows:

$$\varepsilon'(f) = \frac{C(f)}{C_0}, \quad (3.1)$$

$$\varepsilon''(f) = \frac{1}{2\pi f R(f) C_0}. \quad (3.2)$$

The complex impedance measurements serve two parameters at a given frequency, therefore the needed  $R$  and  $C$  parameters can be determined reliably only with some restrictions. Usually the term of  $R_p C_p$  can be neglected because its contribution is much smaller than that of the leading term  $RC$ .  $R_{ITO}$  can also be neglected until it is much smaller than the impedance of the  $RC$  term. Depending on the quality of the ITO layer,  $R_{ITO}$  lies in the order of  $100 \Omega - 1 \text{ k}\Omega$ . Therefore at high  $f$  where the impedance of the  $RC$  term is decreased, the resistance of the ITO causes a  $f$ -dependent parasitic effect. Typically above 100 kHz, cells with ITO are not suggested to be used for dielectric spectroscopy measurements. Although there are methods to compensate this effect [1], the best solution is to use metal (e.g. gold) electrodes with higher conductivity.

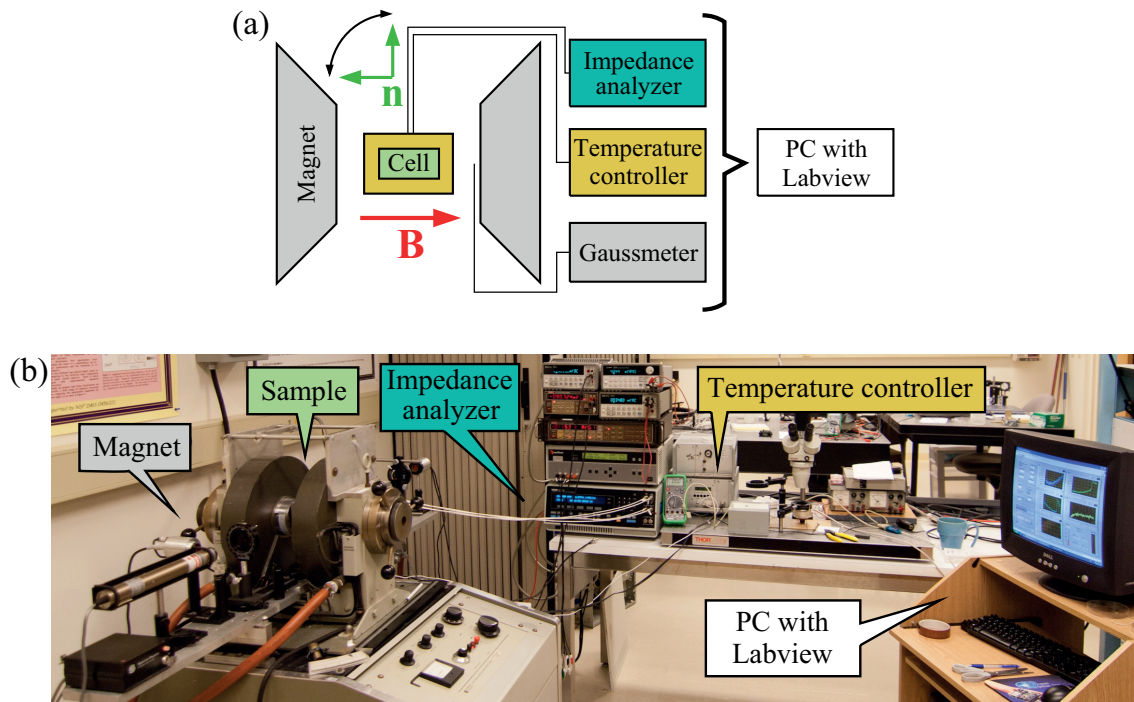


**Fig. 3.2:** The schematic (a) and the real picture (b) of the dielectric spectroscopy experiment.

Our experimental setup (Fig. 3.2) consisted of a Schlumberger 1260 impedance analyzer, an electromagnet capable to produce  $B \approx 1$  T magnetic field, and a custom made temperature controller with a heat stage. The temperature stability was better than  $0.1$  °C. The experimental devices were connected to a computer that controlled the measurements automatically by a Labview program. We note that the setup was assembled in the laboratory of Prof. Dr. Antal Jákli in the Liquid Crystal Institute of the Kent State University in the USA.

The dielectric spectroscopy measurements [P1, P4] were performed in the frequency range  $200$  Hz –  $4$  MHz. In order to remain in the regime of the linear response, the maximum applied measuring voltage was  $0.1$  V (rms). The impedance measurements were done in a 4 wired configuration to reduce the unwanted contribution of the connecting wires. The device was calibrated with a  $1$  k $\Omega$  resistor and the system was successfully tested on parallel RC-probes with known parameters to ensure the precision.

The dielectric properties of the substances were investigated in custom made sandwich cells with gold electrodes. The gold was sputtered onto masked glass plates, then the parts with the patterned electrodes were assembled by sandwiching  $50$   $\mu$ m thick mylar spacers at the edges. UV-curable glue was used for fixation. The electrode area was approximately  $6$  mm  $\times$   $6$  mm and the resulting cell gaps were between  $51$ - $54$   $\mu$ m. Due to the usage of gold electrodes, the electrode resistance could be neglected compared to the impedance of the substances. Since the electrodes were not coated with any alignment layers, the impedance originating from  $R_p$  and  $C_p$  could not play any role at all.  $\varepsilon'$  and  $\varepsilon''$  could be simply calculated by Eq. (3.1) and Eq. (3.2) using the measured values of  $R$  and  $C$ .  $C_0$  was also measured before the filling of the liquid crystals. Because no alignment layers were used, the director had to be oriented by magnetic field. The compounds used have positive diamagnetic susceptibility anisotropies ( $\chi_a$ ), thus their director aligns parallel with the magnetic field.

The measurements of  $\varepsilon_{\parallel}^*$  and  $\varepsilon_{\perp}^*$  could be done by having the normal direction of the cell parallel and perpendicular with respect to  $\mathbf{B}$ . In practice, this could be achieved by rotating the sample holder into the proper position between the poles of the electromagnet. The applied magnetic field was at least 8 times larger than the value of the Fredericksz threshold field. Therefore the measured values are reasonably close to  $\varepsilon_{\parallel}^*$  and  $\varepsilon_{\perp}^*$ .

The evaluation of the dielectric spectra were done by using a complex nonlinear least squares (CNLS) fitting procedure implemented in Matlab. The objective function was defined by Eq. (1.20) with a given number of relaxations. The advantage of this fitting algorithm is that both the real and imaginary parts of the measured  $\varepsilon^*(f)$  dataset are used, thus all parameters ( $\varepsilon(\infty)$ ,  $\Delta\varepsilon_j$ ,  $f_{Rj}$ ,  $\alpha_j$ ,  $\sigma$ ) can be obtained in one step. The details of the CNLS method are presented in the Appendix B.

Temperature ramps with continuous recording of the dielectric data were also performed in order to determine the phase transition temperatures. In such measurements, a constant 10 kHz frequency was used with 1 K/min heating/cooling rates. The resulting data of  $\varepsilon'(T)$  and  $\varepsilon''(T)$  could be used to reveal the phase transitions.

### 3.1.2 The materials

The dielectric spectroscopy measurements [P1, P4] were performed on a bent-core, on a rod-like compound (Fig. 3.3), and on their binary mixtures. We used a typical bent-core mesogen 4-chloro-1,3-phenylene-bis-4[4'-(9-decenyloxy)benzoyloxy] benzoate (ClPbis10BB) that was characterized before in other aspects as it was presented in Sec. 2.1. ClPbis10BB exhibits a monotropic nematic phase in a sufficiently wide temperature range below 100 °C.

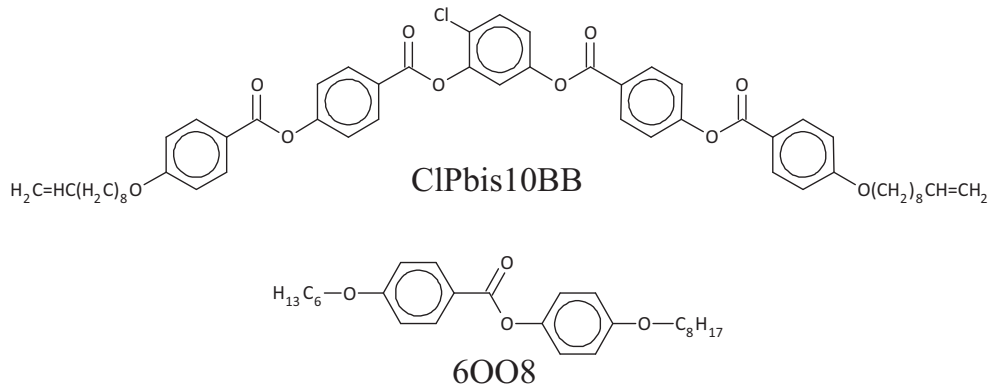


**Fig. 3.3:** The chemical structures of the bent-core ClPbis10BB and the rod-like 6OO8 molecules.

The rod-like compound was a regular calamitic liquid crystal 4-n-octyloxyphenyl 4-n-hexyloxybenzoate (6OO8). We have selected 6OO8 to ensure the complete miscibility with ClPbis10BB in the nematic phase at any concentrations. Previous studies [79] confirmed the total miscibility, which is probably due to the fact that the molecule of

6OO8 is similar to the half of a ClPbis10BB molecule. The pure 6OO8 compound has also a SmC phase below the nematic. The chemical structures of ClPbis10BB and of 6OO8 can be seen in Fig. 3.3.

Mixtures of ClPbis10BB and 6OO8 were prepared in five different concentrations. We have homogenized the mixtures in an ultrasonic bath for 30 minutes, then they were kept at 10 °C above the highest clearing point for one day.

## 3.2 Studies of elasticity

The main goal of our elasticity measurements [P2, P3, P4, P7] were to determine all three Frank elastic constants ( $K_{11}$ ,  $K_{22}$ , and  $K_{33}$ ) of the studied compounds. We have chosen the technique using Freedericksz-transitions because it provides the elastic constants in a relatively direct way compared to the other main branch of methods based on light scattering [80].

The easiest measurements of Freedericksz-transitions concentrate rather on the determination of thresholds  $U_{t0}$ ,  $B_{t0}$ , thus the ratios of  $K_{ii}/|\varepsilon_a|$ , and  $K_{ii}/|\chi_a|$  can be obtained (eqs. (1.8),(1.7)). Performing measurements in different geometries, the ratios of elastic constants can be determined. In order to get the actual values of the elastic constants, however, much more experimental efforts, or known values of  $\varepsilon_a$  and of  $\chi_a$  are needed. Depending on the geometry, the magnetic thresholds are usually characterized by optical or dielectric methods; the electric thresholds are studied mostly by only optical techniques, since the application of large orienting AC voltages with simultaneous dielectric measurements can be problematic.

We could not establish measurements on homeotropic cells using bent-core compounds, since a reliable homeotropic alignment of those were not possible. Furthermore, in order to reduce the necessary amount of materials for the measurements, we employed a procedure with combined electric and magnetic fields to determine a number of different parameters including  $K_{11}$ ,  $K_{33}$ ,  $\varepsilon_{||}$ ,  $\varepsilon_{\perp}$ ,  $\varepsilon_a$ ,  $\chi_a$ , and  $n_a$ , using only a single planar cell. This technique does not focus on the determination of the thresholds, but on the numerical fitting of the whole curves of the effective dielectric constant  $\varepsilon_{eff}$  and of the optical phase difference  $\Delta\phi$  as the function of the applied magnetic field or voltage. The

principle and evaluation methods for this measurement in the so-called *splay* geometry is presented in Sec. 3.2.1.

The determination of  $K_{22}$  can be done in a different (so-called *twist*) geometry. The precise optical detection of a twist deformation is challenging due to the presence of the Mauguin-effect [11]. A dielectric method was thought not to be applicable with a regular planar cell, hence it was not used in the literature. In order to review the difficulties of the *twist* geometry, we developed [P3] a simulation technique to study the relevance of the Mauguin-effect quantitatively, which is lacked from the literature in this context. We also show the basis of the theoretical considerations to reveal the possibility of a novel dielectric method to determine  $K_{22}$  in Sec. 3.2.2.

The used experimental setups are described in Sec. 3.2.3. Finally, the materials under scope are presented in Sec. 3.2.4.

### 3.2.1 The splay geometry

Let us consider a planar cell filled with a nematic liquid crystal that is placed in a Cartesian  $(x,y,z)$  coordinate system (Fig. 3.4(a)). One inner side of the cell is set to lie in the  $x$ - $y$  plane, while the other is shifted with the value of the thickness  $d$  in the  $z$ -direction. The undistorted director without pretilt would be parallel with the  $x$ -axis. Nevertheless a nonzero pretilt  $\Theta_0$  is considered in an antiparallel orientation at the cell boundaries, since that condition is realistic for the description of a planar cell prepared by antiparallel rubbing of the alignment layers.

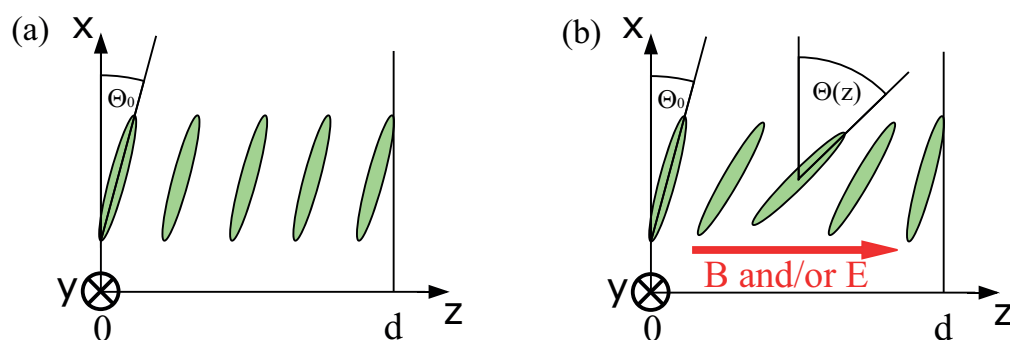


**Fig. 3.4:** The schematic figure of the splay Freedericksz-transition geometry in a planar cell with pretilt. The director is symbolized by green ellipses. (a) With no applied fields, the director is homogeneous. (b) If large enough magnetic and/or electric fields are present, the director field is deformed. The deformation is described by the tilt angle  $\Theta(z)$ .

The homogeneous magnetic inductance  $\mathbf{B} = (0, 0, B)$  is applied in the z-direction. The diamagnetic susceptibility anisotropy  $\chi_a$  is assumed to be positive, thus  $\mathbf{B}$  can destabilize the homogeneous planar director configuration (Fig. 3.4(b)). A voltage  $U$  is optionally switched to cell that generates an electric field parallel with the z-direction. Depending on the sign of  $\varepsilon_a$ , the electric field can either stabilize or destabilize the initial homogeneous director field. First we consider the case with  $U = 0$  V, for simplicity [10].

Our goal is to obtain the material parameters by the numerical fit of the experimental data. In order to achieve that, we calculate the magnetic field dependence of the effective dielectric constant  $\varepsilon_{eff}$  that can be measured directly. Then we calculate the optical phase difference  $\Delta\varphi$  as the function of  $B$ , thus the transmittance measurements can also be fitted. The calculations are shown in detail in Appendix A; we present here only the main steps next.

First of all, we have to calculate the director field as the function of  $B$ . In the splay geometry, the  $B$  induced deformation is considered as homogeneous, which means there is no director modulation in the  $x - y$  planes at an arbitrary value of  $z$ . The deformation profile can be described by only one variable  $\Theta(z)$  that is the z-dependent tilt angle (Fig. 3.4(b)):

$$\mathbf{n} = (\cos \Theta, 0, \sin \Theta). \quad (3.3)$$

The total free energy density  $f_{tot}$  consists of the sum of the elastic (Eq. 1.1) and of the magnetic (Eq. 1.4) free energy densities:  $f_{tot} = f_{elast} + f_{magn}$ . Using Eq. (3.3),  $f_{tot}$  is expressed in terms of  $\Theta$  and of  $\Theta' = \frac{\partial\Theta}{\partial z}$ :  $f_{tot} = f_{tot}(\Theta', \Theta)$ . In equilibrium, the free energy  $F = \iiint_V f_{tot}(\Theta', \Theta) dV$  is minimal; the optimum director configuration minimizes  $F$ . Mathematically this problem can be solved by variation calculus:  $\Theta(z)$  is the solution of an Euler-Lagrange equation:

$$\frac{d}{dz} \left( \frac{\partial f_{tot}}{\partial \Theta'} \right) - \frac{\partial f_{tot}}{\partial \Theta} = 0. \quad (3.4)$$

Eq. (3.4) yields a nonlinear second order autonomous ordinary differential equation with the independent variable  $z$ . The equation to solve is a boundary value problem, since we

considered strong anchoring at the planar alignment layers. Furthermore,  $\Theta'$  has to be 0 in the middle of the cell, due to the mirror symmetry. The boundary conditions are:

$$\Theta(z)|_{z=0} = \Theta(z)|_{z=d} = \Theta_0, \quad (3.5)$$

$$\Theta'(z)|_{z=d/2} = 0. \quad (3.6)$$

The differential equation from Eq. (3.4) can be further processed (see Appendix A) and transformed to an integral equation:

$$\frac{\pi}{2} \frac{B}{B_{ts0}} = \int_{\xi_0}^{\pi/2} \sqrt{\frac{1 + \kappa \sin^2 \Theta_m \sin^2 \xi}{1 - \sin^2 \Theta_m \sin^2 \xi}} d\xi, \quad (3.7)$$

where  $\xi_0 = \arcsin\left(\frac{\sin \Theta_0}{\sin \Theta_m}\right)$ ,  $\kappa = \frac{K_{33} - K_{11}}{K_{11}}$ , and  $B_{ts0} = \frac{\pi}{d} \sqrt{\frac{\mu_0 K_{11}}{|\chi_a|}}$  ('s' stands for *splay*). The numerical solution of Eq. (3.7) gives the maximal tilt angle  $\Theta_m = \Theta(z)|_{z=d/2}$  that we use later. The next steps are to determine  $\varepsilon_{eff}$  and  $\Delta\varphi$  at a given applied magnetic field  $B$ .

In a general deformed state, the cell is inhomogeneous in the  $z$ -direction, hence it is useful to split it into thin slabs of thickness  $dz$ . The cell capacitance  $C$  is the net of the capacitances of all slabs connected in series.  $\varepsilon_{eff}$  is calculated by dividing the capacitance of the cell with that of the empty cell. In the  $dz \rightarrow 0$  limit one obtains

$$\varepsilon_{eff} = \frac{C}{C_0} = d \left[ \int_0^d \frac{1}{\varepsilon_{\perp} + \varepsilon_a \sin^2 \Theta(z)} dz \right]^{-1}. \quad (3.8)$$

Combining eqs. (3.4)-(3.8), after some transformations (see Appendix A) we get the formula what we have actually used in the fitting procedure:

$$\varepsilon_{eff} = \frac{\pi}{2} \frac{B}{B_{ts0}} \left[ \int_{\xi_0}^{\pi/2} \sqrt{\frac{1 + \kappa \sin^2 \Theta_m \sin^2 \xi}{(1 - \sin^2 \Theta_m \sin^2 \xi) (\varepsilon_{\perp} + \varepsilon_a \sin^2 \Theta_m \sin^2 \xi)^2}} d\xi \right]^{-1}. \quad (3.9)$$

The effective refractive index  $n_{eff}$  for the extraordinary ray depends on the  $z$ -direction through  $\Theta(z)$ , thus the net optical phase difference between the transmitted extraordinary and ordinary rays can be obtained by an integral:

$$\Delta\varphi = \frac{2\pi}{\lambda} \int_0^d (n_{eff} - n_o) dz, \quad (3.10)$$

where  $\lambda$  is the wavelength of light, and according to Eq. (1.27):

$$n_{eff} = \frac{n_e}{\sqrt{1 + \nu \sin^2 \Theta}}, \quad (3.11)$$

where  $\nu = \frac{n_e^2 - n_o^2}{n_e^2}$ . After some similar transformations that were done in the case of  $\varepsilon_{eff}$ , the final expression is:

$$\Delta\varphi = \frac{4dn_e}{\lambda} \frac{B_{ts0}}{B} \int_{\xi_0}^{\pi/2} \sqrt{\frac{1 + \kappa \sin^2 \Theta_m \sin^2 \xi}{1 - \sin^2 \Theta_m \sin^2 \xi}} \left( \frac{1}{\sqrt{1 + \nu \sin^2 \Theta_m \sin^2 \xi}} - \frac{1}{\sqrt{1 + \nu}} \right) d\xi \quad (3.12)$$

In summary, first Eq. (3.7) has to be used to determine  $\Theta_m$  for a given value of  $B$ . Then  $\varepsilon_{eff}$ , and  $\Delta\varphi$  are calculated by Eqs. (3.9), and (3.12), respectively. Doing this procedure for a number of  $B$  values, the  $B$  dependence of  $\varepsilon_{eff}$  and of  $\Delta\varphi$  can be obtained that can be compared to the experimental data. A fitting algorithm (see Appendix B) was developed in Matlab that is based on the method described above.

The simulated and measured data of  $\varepsilon_{eff}(B)$  can be compared directly. Our fitting algorithm used a nonlinear optimization method that varied the fit parameters until the sum of the square differences between the experimental and the theoretical data points was minimal. We used four fit parameters:  $B_{ts0}$ ,  $\Theta_0$ ,  $\varepsilon_{||}$ , and  $\kappa$ . The rest of the parameters were known ( $d$ ,  $B$ ) or could be read from the measured data ( $\varepsilon_{eff}|_{B=0} \cong \varepsilon_{\perp}$ ), thus those were fixed in the simulations.

In the optical experiments, we could measure the transmitted intensity of a laser through our sample between crossed polarizers. In order to conveniently fit the experimental data, the magnetic field dependence of the optical phase difference  $\Delta\varphi$  has to be calculated from the measured intensity. This conversion can be done using Eq. (1.32). Nevertheless, this conversion process is not straightforward, because the intensity is not monotonic with  $B$  if  $\Delta\varphi_0 > \pi$ . In a general case, the intensity is an oscillating function of  $B$  (or  $V$ ). It is known that at very high fields, the initial planar structure is reoriented to a quasi-homeotropic state, where  $\Delta\varphi = 0$  and  $I = 0$ . According to Eq. (1.32), the last maximum of the intensity (before its final decay to 0 at high  $B$ ) corresponds to  $\Delta\varphi = \pi$ . Furthermore it is also known that between each neighbouring maximum and minimum in the intensity, there is a  $\pi$  difference in  $\Delta\varphi$ . Consequently the optical phase differences can be given at the specific values of  $B$ , where a maximum or minimum is found in

the intensity. At the intermediate values of the magnetic field (between an intensity maximum and minimum), the inversion of Eq. (1.32) can be done unambiguously to determine the intermediate values of  $\Delta\varphi$ . As the result of this kind of conversion,  $\Delta\varphi(B)$  is obtained in a way, where all intensity data points are assigned to a value of the optical phase difference, providing a detailed curve of  $\Delta\varphi(B)$ . If there is doubt in that the last measured intensity peak is not followed by others above the measurement range of  $B$ , the following procedure has to be applied: 1) Make the conversion similarly as described above, assuming that the last measured intensity peak corresponds to  $\Delta\varphi = \pi$ . 2) Take the values of  $\Delta\varphi$  in the range of  $B \gtrsim 3B_{ts0}$  ( $\Delta\varphi_{asympt}$ ), and plot  $\Delta\varphi_{asympt}$  as the function of  $1/B$ . 3) Fit a line on the graph, then extrapolate it towards  $1/B = 0$  that corresponds to infinitely high  $B$ . 4) If the extrapolated line crosses the  $\Delta\varphi_{asympt}$ -axis close to 0, the initial assumption in 1) was proper. Otherwise  $n2\pi$  ( $n = 1, 2, \dots$ ) has to be added to data of  $\Delta\varphi$  that was obtained after step 1), until the condition defined in step 4) is satisfied.

After  $\Delta\varphi$  is obtained as the function of  $B$ , a fitting procedure similar to the one discussed in the dielectric case could be performed. Here also four parameters were used:  $B_{ts0}$ ,  $\kappa$ ,  $n_e$ , and  $n_o$ . The common parameters could be used to test the consistency of our fitting methods. More details of the fitting can be found in the Appendix B.

In order to determine  $K_{11}$  and  $K_{33}$ , we need more information. If our compound has  $\varepsilon_a > 0$ , the electric Fredericksz-transition can be observed optically, similarly to the magnetic case. The calculations are slightly complicated, due to the inhomogeneity of the electric field (see Sec. 1.2.2) in a deformed director field. Here only the final results are shown that were used in the fitting method.

Applying a voltage  $U$  on the planar cell, the maximal tilt angle  $\Theta_m$  can be determined by solving an integral equation, analogously to Eq. (3.7):

$$\frac{\pi}{2} \frac{U}{U_{ts0}} = \int_{\xi_0}^{\pi/2} \sqrt{\frac{(1 + \gamma \sin^2 \Theta_m) (1 + \kappa \sin^2 \Theta_m \sin^2 \xi)}{(1 + \gamma \sin^2 \Theta_m \sin^2 \xi) (1 - \sin^2 \Theta_m \sin^2 \xi)}} d\xi, \quad (3.13)$$

where  $U_{ts0} = \pi \sqrt{\frac{K_{11}}{\varepsilon_0 \varepsilon_a}}$  and  $\gamma = \frac{\varepsilon_a}{\varepsilon_{\perp}}$ . The phase difference  $\Delta\varphi$  is given by:

$$\Delta\varphi = \frac{2\pi d n_e}{\lambda} \left\{ \frac{\int_{\xi_0}^{\pi/2} \sqrt{\frac{(1 + \kappa \sin^2 \Theta_m \sin^2 \xi) (1 + \gamma \sin^2 \Theta_m \sin^2 \xi)}{(1 - \sin^2 \Theta_m \sin^2 \xi) (1 + \nu \sin^2 \Theta_m \sin^2 \xi)}} d\xi}{\int_{\xi_0}^{\pi/2} \sqrt{\frac{(1 + \kappa \sin^2 \Theta_m \sin^2 \xi) (1 + \gamma \sin^2 \Theta_m \sin^2 \xi)}{1 - \sin^2 \Theta_m \sin^2 \xi}} d\xi} - \frac{1}{\sqrt{1 + \nu}} \right\} \quad (3.14)$$

The voltage dependence of  $\Delta\varphi$  can be fitted by only one parameter  $U_{t0}$ , since all the others were determined previously in the magnetic case.

Nevertheless if our compound exhibits  $\varepsilon_a < 0$ , the applied voltage tends to stabilize the initial planar director configuration, thus an alternative method has to be used. Our idea was to measure the Fredericksz-thresholds, when both electric and magnetic fields are present in the sample. It can be shown [10] that an applied voltage  $U_{ts}$ , may decrease or increase the magnetic threshold field  $B_{ts}$ :

$$\frac{B_{ts}}{B_{ts0}} = \sqrt{1 \mp \left( \frac{U_{ts}}{U_{ts0}} \right)^2}, \quad (3.15)$$

where the  $-$  and  $+$  signs apply for the case of  $\varepsilon_a > 0$  and  $\varepsilon_a < 0$ , respectively.  $B_{ts0}$  and  $U_{ts0}$  correspond to the thresholds discussed above without an applied voltage and magnetic field, respectively.

### 3.2.2 The twist geometry

Let us consider a planar cell with strong anchoring and a pretilt of  $\Theta_0$ , filled with a nematic liquid crystal that exhibits  $\chi_a > 0$ , similarly to the case of the splay geometry (Fig. 3.4(a)). The homogeneous magnetic field  $\mathbf{B} = (B_x, B_y, B_z)$  is applied in a general direction. The magnitude of the magnetic inductance is denoted by  $B = |\mathbf{B}|$ . The pure twist geometry corresponds to the case where,  $B_x = B_z = 0$ . We use this pure case unless it is noted otherwise. Nevertheless our model [P3] is capable of handling magnetic fields lying along a general direction that is used later to describe the situation where  $\mathbf{B}$  is slightly misaligned from the y-direction. The motivation for that is to have the opportunity to simulate the effects of the imperfectly adjusted geometry that is crucial in the comparison with realistic experiments. The twist geometry is visualized in the cross section of the cell (Fig. 3.5(a)), and in a view from the normal direction of the cell

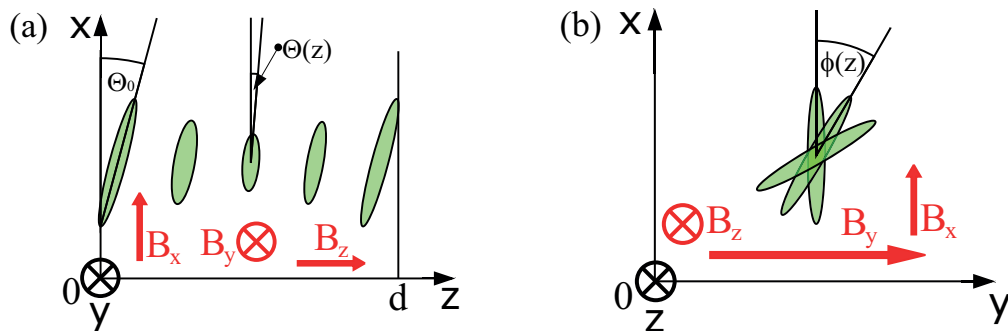


**Fig. 3.5:** The twist Fredericksz-geometry with pretilt in two views: (a) the cross-section normal to the substrates; (b) a view parallel with normal direction of the substrates.

plane (Fig. 3.5(b)). Before our work, the twist geometry was considered with neglected pretilt (e.g. [10]). With  $\Theta_0 = 0$ , the threshold of the twist Fredericksz-transition is given by  $B_{tt0} = \frac{\pi}{d} \sqrt{\frac{\mu_0 K_{22}}{\chi_a}}$ , and the director profile can be described with only one variable: the twist angle  $\phi$ . Considering a nonzero pretilt, however, a second variable, the tilt angle  $\Theta$  is also necessary for an appropriate description of the director field. The director can be expressed in a Cartesian coordinate system by

$$\mathbf{n} = (\cos \Theta \cos \phi, \cos \Theta \sin \phi, \sin \Theta). \quad (3.16)$$

The magnetic field exerts a torque on the director in a way, where both the twist ( $\phi$ ) and the tilt ( $\Theta$ ) angles are changed compared to the undeformed state (see Fig. 3.5). The deformation is homogeneous, thus both angles depend only on the  $z$ -coordinate. The mirror symmetry of the cell here is also assumed as in the case of the splay geometry, yielding that the maximal deformation occurs at  $z = d/2$ .

The main steps of the twist director field calculations are similar to the case of the magnetic Fredericksz-transition in the splay geometry (Sec. 3.2.1). The total free energy density is given by the sum of the elastic and magnetic components:  $f_{tot} = f_{elast} + f_{magn}$ . Substituting  $\mathbf{n}$  (Eq. (3.16)) and the general  $\mathbf{B}$  in  $f_{tot}$  results:

$$\begin{aligned} f_{tot} = & \frac{1}{2} f(\Theta) \Theta'^2 + \frac{1}{2} g(\Theta) \phi'^2 - \frac{1}{2} \frac{\chi_a}{\mu_0} \left[ B_x^2 \cos^2 \Theta \cos^2 \phi \right. \\ & + B_y^2 \cos^2 \Theta \sin^2 \phi + B_z^2 \sin^2 \Theta + 2B_x B_y \cos^2 \Theta \sin \phi \cos \phi \\ & \left. + 2B_x B_z \sin \Theta \cos \Theta \cos \phi + 2B_y B_z \sin \Theta \cos \Theta \sin \phi \right], \end{aligned} \quad (3.17)$$

where  $\Theta' = \frac{\partial \Theta}{\partial z}$ ,  $\phi' = \frac{\partial \phi}{\partial z}$ , and

$$f(\Theta) = K_{11} \cos^2 \Theta + K_{33} \sin^2 \Theta, \quad (3.18)$$

$$g(\Theta) = \cos^2 \Theta (K_{22} \cos^2 \Theta + K_{33} \sin^2 \Theta). \quad (3.19)$$

Euler-Lagrange equations are used to minimize the free energy in order to obtain the equilibrium director configurations:

$$\left. \begin{aligned} \frac{d}{dz} \left( \frac{\partial f_{tot}}{\partial \Theta'} \right) - \frac{\partial f_{tot}}{\partial \Theta} &= 0 \\ \frac{d}{dz} \left( \frac{\partial f_{tot}}{\partial \phi'} \right) - \frac{\partial f_{tot}}{\partial \phi} &= 0 \end{aligned} \right\} \quad (3.20)$$

Combining Eqs. (3.17)-(3.20), gives the system of two second order coupled nonlinear autonomous ordinary differential equations. We show the system what we have actually used in our simulations of the pure twist case:

$$\left. \begin{aligned} \Theta'' &= \frac{\sin \Theta \cos \Theta}{1 + \kappa \sin^2 \Theta} \left[ (\phi')^2 p (1 - q \sin^2 \Theta) + r \sin^2 \phi - (\Theta')^2 \kappa \right] \\ \phi'' &= -\frac{\Theta' \phi' (a - 1) (1 - q \sin^2 \Theta)}{\cos^2 \Theta (1 + a \sin^2 \Theta)} - s \frac{\sin \phi \cos \phi}{1 + a \sin^2 \Theta} \end{aligned} \right\} \quad (3.21)$$

where  $\kappa = \frac{K_{33} - K_{11}}{K_{11}}$ ,  $p = \frac{K_{33} - 2K_{22}}{K_{11}}$ ,  $q = \frac{2(K_{33} - K_{22})}{K_{33} - 2K_{22}}$ ,  $r = \frac{\chi_a B^2}{\mu_0 K_{11}}$ ,  $a = \frac{K_{33} - K_{22}}{K_{22}} - 1$ , and  $s = \frac{\chi_a B^2}{\mu_0 K_{22}}$ . The boundary conditions for Eqs. (3.20)-(3.21) are:  $\Theta(z)|_{z=0} = \Theta(z)|_{z=d} = \Theta_0$ ,  $\phi(z)|_{z=0} = \phi(z)|_{z=d} = 0$ ,  $\Theta'(z)|_{z=d/2} = 0$  and  $\phi'(z)|_{z=d/2} = 0$ . We solved the system numerically in Matlab.

In the case of the splay geometry (Sec. 3.2.1), the director configuration was connected to experimentally accessible quantities, such as  $\varepsilon_{eff}$  and  $\Delta\varphi$ . Here we can also use Eq. (3.8) to calculate the effective dielectric constant  $\varepsilon_{eff}$  for a given director deformation, because the capacitance of the cell is sensitive only for the tilt angle  $\Theta$ .

The simulation of the optical response in the twist geometry, however, needs a different approach than that was discussed above in Sec. 3.2.1. The transmittance of the cell placed between crossed polarizers is calculated with the Mueller-matrix method presented in Sec. 1.2.6 [31, 32, 33]. If the director is deformed, the cell is inhomogeneous

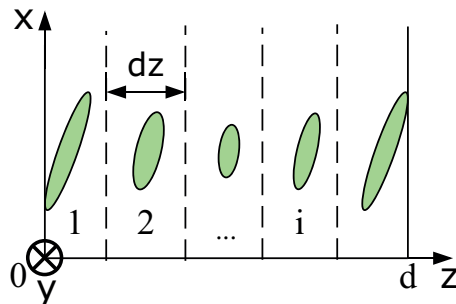


**Fig. 3.6:** A planar cell that is split into thin slabs of thickness  $dz$  for optical calculations.

in the  $z$ -direction, therefore we split it into thin slabs of thickness  $dz$  as illustrated in Fig. 3.6.

If  $dz$  is set to be small enough, the twist ( $\phi$ ) and tilt ( $\Theta$ ) angles can be approximated as constant in one slab. Then each slab is considered a birefringent waveplate with the slow axis oriented at an angle of  $\phi_i$  with respect to the  $x$ -axis, performing a phase shift  $\Delta\varphi_i$ . The retardation of the  $i$ th slab originates from its birefringence, thus considering Eqs. (3.10)-(3.11), it is given by:

$$\Delta\varphi_i = \frac{2\pi}{\lambda} \left( \frac{n_e}{\sqrt{1 + \nu \sin^2 \Theta_i}} - n_o \right) dz, \quad (3.22)$$

where  $\Theta_i$  is the tilt angle at the position of the  $i$ th slab. Taking it all round, the Mueller-matrix of the  $i$ th slab is  $\mathbf{M}_{wp}(\phi_i, \Delta\varphi_i)$ . Our liquid crystal cell is placed between polarizers. The angles between the  $x$ -axis and the polarizing direction of the polarizer and of the analyzer are  $\varsigma_p$  and  $\varsigma_a$ , respectively. The cell is illuminated with an incident monochromatic light characterized by the Stokes-vector  $\mathbf{s}_{in}$ , thus the Stokes-vector of the outgoing light,  $\mathbf{s}_{out}$ , can be calculated as

$$\mathbf{s}_{out} = \mathbf{M}_{pol}(\varsigma_a) \left( \prod_{i=1}^n \mathbf{M}_{wp}(\phi_i, \Delta\varphi_i) \right) \mathbf{M}_{pol}(\varsigma_p) \mathbf{s}_{in}. \quad (3.23)$$

The actual matrices of  $\mathbf{M}_{wp}$  and of  $\mathbf{M}_{pol}$  were presented in Eq. (1.30). The optical transmittance is given by the ratio of the 0th elements of  $\mathbf{s}_{out}$  and of  $\mathbf{s}_{in}$ .  $\mathbf{s}_{in}$  was chosen to be linearly polarized in the direction parallel to the polarizer. We set  $\varsigma_p = 0$  and  $\varsigma_a = 90^\circ$ , thus the transmittance is assumed to be proportional to the expected depolarization.

### 3.2.3 Experimental technique

Our experiments were done in two different experimental setups (referred to as S1 and S2) capable of performing similar measurements (Fig. 3.7). Both setups could be used to measure simultaneously the capacitance and the transmitted intensity through a planar liquid crystal cell placed between crossed polarizers, as a function of the applied magnetic inductance  $B$ . The effective dielectric constant  $\varepsilon_{eff}$  was calculated as the ratio of the filled and the empty cell capacitances (see Sec. 3.1). The scanning of the  $B$ -range was performed in discrete steps in the order of 1 mT. After each step, the measurement system waited for a predefined amount of time (in the order of 10 s), in order to let the liquid crystal to be stabilized in a new equilibrium state. The adequateness of the waiting time was tested by running a field-scan with increasing, then immediately with decreasing fields. If our data did not show hysteresis, we considered the waiting time as properly selected. The experiments could be carried out in both the splay (Fig. 3.4) and the twist (Fig. 3.5) geometries, by rotating the sample holders to the proper positions. The optical transmittance measurements could be also done with applied voltages of different magnitudes. The samples were put between crossed polarizers. In the splay geometry, the polarizer was adjusted to  $45^\circ$  with respect to the initial director to get the highest intensity according to Eq. (1.32), while this angle was set to zero in the other case where only the depolarization had to be measured.

We assembled setup S1 (Fig. 3.7(b)) in the laboratory of Prof. Dr. James T. Gleeson in the Department of Physics of the Kent State University in the USA. The studied liquid crystal cell was kept in a custom-made heat stage driven by a PID controller. The temperature stability of the system was better than  $0.1^\circ\text{C}$ . The applied magnetic inductance was generated by an electromagnet in the range of  $B = 0 - 1.3$  T. A Hall-probe was used to measure  $B$ . The capacitance was measured by a high precision Andeen-Hagerling 2500A capacitance/loss analyzer at  $f = 1$  kHz using a 4-wired technique. A 4 mW high stability He-Ne laser ( $\lambda = 633$  nm) was used as a monochromatic light source. In order to determine the transmitted laser intensity, the voltage signal of a Thorlabs PDA55 photodetector was measured by an Agilent 34401A digital multimeter. We note that in the twist geometry, where the low transmittance is expected to originate from a weak scattered light, the intensity signal was tried to be measured using a chopper with a lock-in detector, but the results were similar to those obtained by the simpler

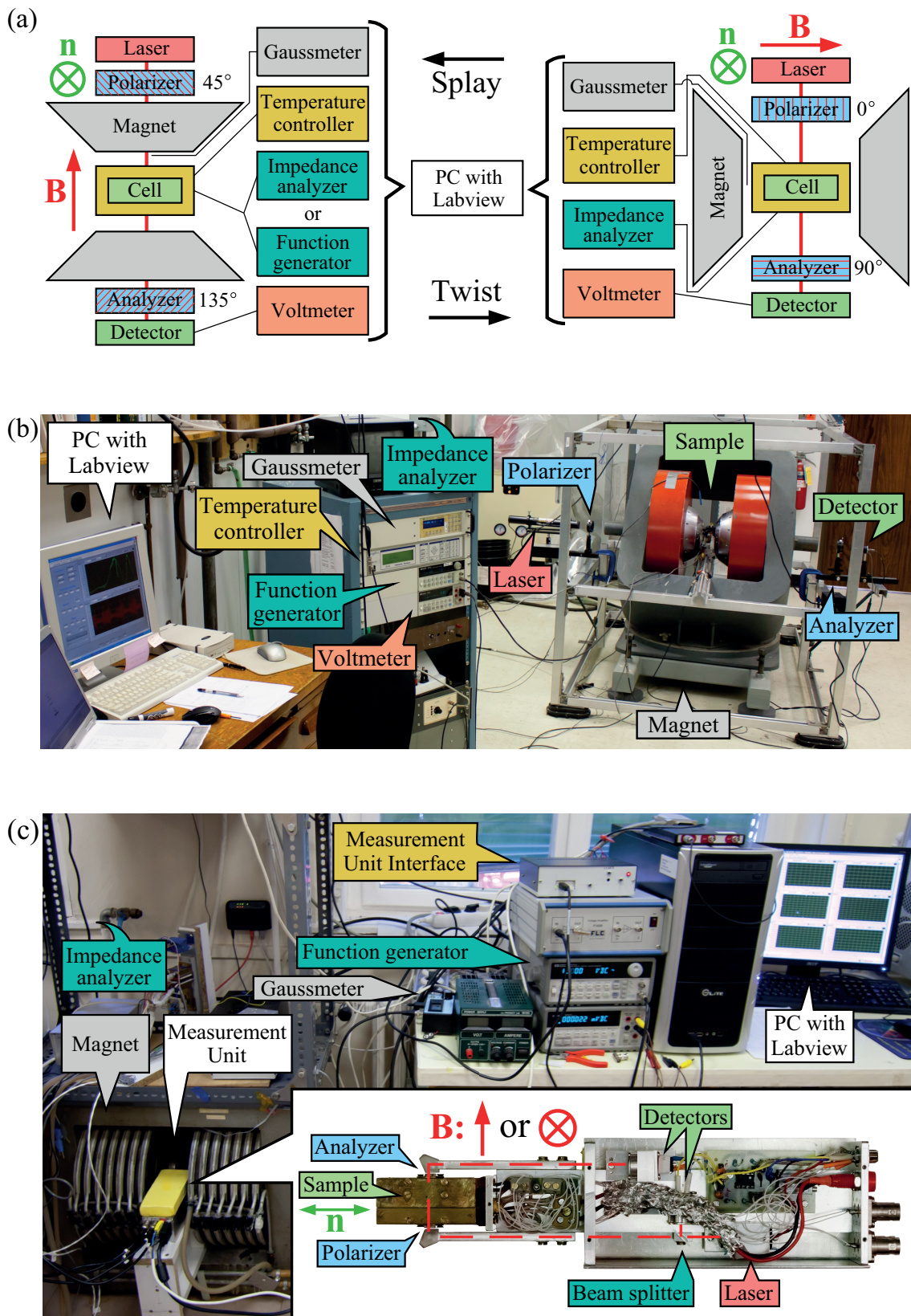


**Fig. 3.7:** (a) The schematic illustrations of the splay and twist Fredericksz-transition experiments. (b) Images of setup S1, and of S2 (c) assembled in the splay geometry.

technique presented above. The optical measurements in the case of the splay and the twist geometries could be done in two perpendicular light paths. Interestingly, the light path of the splay measurement crossed the magnet through the holes on the poles, since in that case the light propagation direction has to be parallel to the magnetic field (Fig. 3.7(b)).

Setup S2 (Fig. 3.7(c)) was put together in the Wigner Research Centre for Physics (formerly the Research Institute for Solid State Physics and Optics) in Budapest. There were no electromagnets available with holes on the poles, thus a different geometry had to be applied. In order to provide the conditions for a number of electromagneto-optical and -dielectric measurements, including the splay and twist Fredericksz-transitions, we designed and built a new experimental system. Instead of using space-consuming optical rails as in the case of setup S1, we planned to create a compact measurement unit that includes a temperature controlled sample holder and the whole optical system with the laser, the polarizers, and the photodetector(s). The following requirements were settled for the system: 1) the heat-stage should allow to use temperatures up to 200 °C with minimal  $T$  gradients and with a precision better than 0.1 °C; 2) the size of the sample holder should be compatible with the rotation inside the 49 mm wide air gap between the poles of an electromagnet; 3) the materials of the unit should be non-magnetic; 4) simultaneous optical transmittance and four wired impedance measurements should be possible. The final form of the instrument met all requirements: the brass heat-stage was equipped with symmetric heating realized by two custom-made bifilar heater coils. The inside temperature was determined by measuring the resistance of a Pt100 sensor using the 4-wired technique. An analog circuit generated a voltage signal proportional to the resistance that was measured by a National Instruments NI USB-6009 multi-functional I/O device (placed in the 'Measurement Unit Interface' - see Fig. 3.7(c)). The heater current was controlled by a voltage signal from the NI USB-6009. The temperature control was ensured by a PID algorithm implemented in Labview, providing a precision better than 0.05 °C. The beam of a red diode laser ( $\lambda = 657.3$  nm) is turned 90° twice by two pentaprisms (see the inset in Fig. 3.7(c)), thus the splay and twist geometries can be simply changed by rotating the whole measurement unit in the magnet by 90°. The beam was split immediately after the light source in order to monitor the laser intensity in real-time by an amplified signal of a photodiode. The second photodiode

measured the intensity transmitted through the cell. The two intensity signals and the voltage proportional to  $B$  obtained from an Alphaslab 100 Gaussmeter were measured at different input channels of the NI USB-6009 device. Two adjustable polarizers were attached to the heat-stage. All parts were selected to be made of brass, aluminium or other non-magnetic materials. In the splay geometry, the impedance of the cell was measured by a Hioki 3522 impedance analyzer, using the 4-wired technique. In the twist geometry, where very small changes of the cell capacitance are expected, a different method was used. A 1 kHz sinusoidal voltage signal with 30 mV amplitude was switched to the cell using the function generator output of a TiePie Handyscope HS3 instrument. The current in the circuit was converted to a voltage signal with an Ithaco Model 1642 current sensitive preamplifier. The applied voltage and the signal proportional to the current was measured as the function of time by the two oscilloscope channels of the TiePie Handyscope HS3 device. The complex impedance of the system was calculated using the operation principle of the dual-phase lock-in detector (see Appendix C for details). The impedances of the cables and of the open circuit were also measured, and the values were used for corrections of the results on the liquid crystal cell. Using the corrected impedance of the cell, the capacitance could be determined. This method gave more stable and reliable results than using the impedance analyzer in cases where only very small changes in the cell capacitance were expected.

### 3.2.4 The materials

The compound CIPbis10BB was used first in our investigations [P2] of the bent-core nematic elasticity with setup S1. Earlier studies that revealed some extraordinary properties of CIPbis10BB, were presented in Sec. 2.1. The molecular structure of CIPbis10BB was shown in Fig. 3.3. We determined all elastic constants and a number of other material parameters at  $\Delta T = T - T_{NI} = -2$  °C, using a  $d = 27$   $\mu\text{m}$  thick planar cell.

Later we extended our studies [P3] of elasticity on a different kind of bent-core nematic compound synthesized recently [81]: a thiadiazol with a pyridine arm with two hexyloxy chains and an ester arm with two lateral hexyloxy chains, where the ethyl ester is connected via a hexamethylene spacer (DT6PY6E6). The chemical structure of DT6PY6E6 is presented in Fig. 3.8.

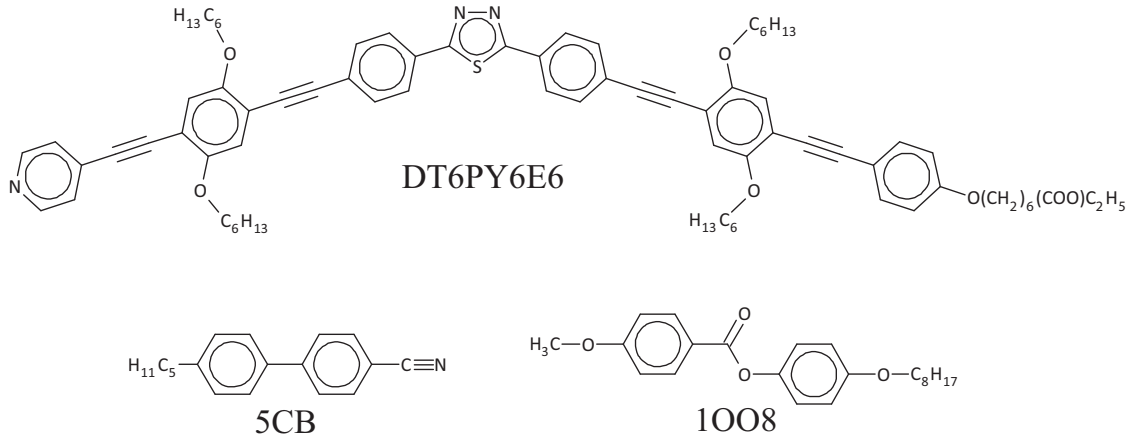


**Fig. 3.8:** The chemical structures of DT6PY6E6, 5CB and 1008.

DT6PY6E6 exhibits a nematic phase in a relatively wide temperature range. The nematic-isotropic phase transition temperature is  $T_{NI} = 149$  °C, the melting point in heating is 93 °C, however, the nematic phase can be supercooled down to room temperature. Our measurements of elastic constants were done at  $\Delta T = T - T_{NI} = -24$  °C, using a  $d = 27.3$   $\mu\text{m}$  thick custom made planar cell with setup S1.

In order to test and verify our measurement and evaluation systems, the textbook standard rod-like compound 4-pentyl-4-cyanobiphenyl (5CB) was used in planar cells with thicknesses of  $d = 27$   $\mu\text{m}$  in setup S1 [P2], and of  $d = 26$   $\mu\text{m}$  in setup S2 [P3]. The chemical structure of 5CB is presented in Fig. 3.8. The clearing point of 5CB is  $T_{NI} = 35$  °C, and our measurements were performed at  $\Delta T = -12$  °C, and  $\Delta T = -8$  °C.

Another rod-like compound, 4-n-octyloxyphenyl 4-n-methoxybenzoate (1008) was characterized in setup S2 [P7], due to the need of the material parameters for our studies on pattern formation discussed in Sec. 4.3. 1008 is a member of the same family of mesogens as 6008; the difference is in the length of one terminal alkyl chain (Fig. 3.8). 1008 melts to the nematic from the crystalline phase in heating at 63.5 °C, and the nematic-isotropic phase transition temperature is  $T_{NI} = 76.7$  °C. The nematic phase can be supercooled down to 53 °C.

For all compounds, standard planar sandwich cells with rubbed polyimide orienting layers were used. The thicknesses of the empty cells were determined from interferometry. The mesogens were filled into the cells by capillarity in the isotropic phase, then they were cooled down slowly to the nematic phase in order to have well-aligned samples. The good qualities of the planar configurations were confirmed by polarizing microscopy.

### 3.3 Time resolved pattern imaging

#### 3.3.1 Experimental technique

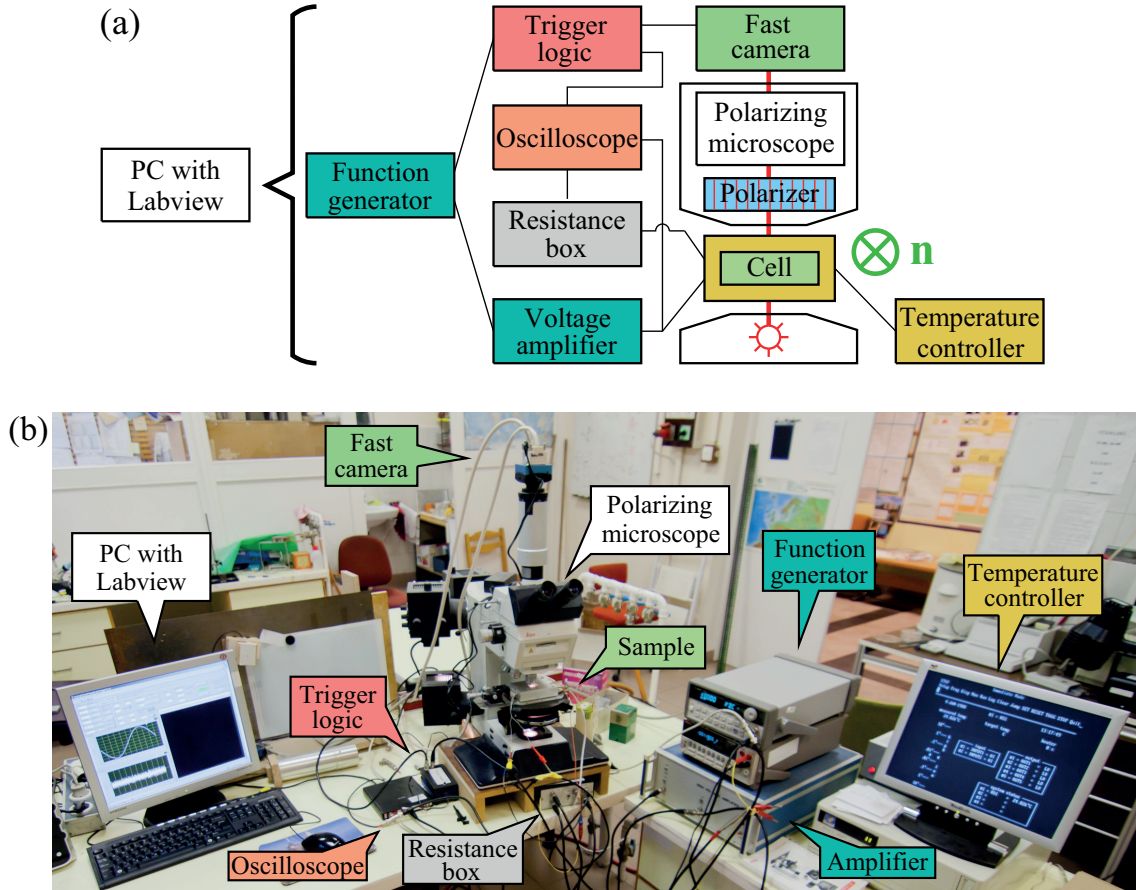


**Fig. 3.9:** The schematic diagram (a) and a photo (b) of the measurement system for studying the temporal behavior of the low frequency pattern forming mechanisms in nematic liquid crystals.

The schematic diagram and a photo of the measurement system can be seen in Fig. 3.9(a), and b, respectively. The liquid crystal cells were studied in a temperature stabilized environment in an Instec HSi heat stage driven by an mK-1 controller with a precision better than 0.01 °C. The amplified voltage signals of an Agilent 33120A function generator were switched to the samples. The electric field induced patterns were observed in a Leica DM RX polarizing microscope in transmission mode with white light illumination using the shadowgraph technique (the polarizer was removed, while the analyzer was set to be parallel with the rubbing direction). The image acquisition system consisted of an EoSens MC1362 high speed camera connected to an Inspecta-5

frame grabber card. Before recording the images, the pattern forming system was let to be stabilized for one or two periods of the driving signal (or for 5 seconds at frequencies higher than 0.2 Hz). After the time of waiting, a sequence of maximum 1000 images was recorded with different rates depending on the frequency (maximum 2000 frames/s at  $512 \times 520$  resolution with 256 grey levels). A custom-designed trigger logic was used to synchronize the image recording with the driving voltage. The acquisition of the first image was triggered by the zero crossing (from negative to positive) of the applied voltage.

Before the optical observations of pattern formation, the electric current through the cell was determined by measuring the voltage drop on a small, known resistance connected in series with the sample [P5, P6]. A TiePie Handyscope HS3 oscilloscope recorded simultaneously the driving voltage and the signal proportional to the current as the function of time, for a set of frequencies. Later, the measurement system was improved to be capable of performing triggered current measurements simultaneously to the image recording [P7]. The experimental systems were controlled by Labview, thus fully automated measurements were possible to be performed as the function of voltage and of frequency. The resulting large amount of data was processed in Matlab.

### 3.3.2 The used compounds

The first set of experiments [P5, P6] were performed on the nematic mixture Phase 5 (made by Merck & Co. Inc.) that is considered a reference compound for studying standard electroconvection [43, 50]. Phase 5 has a wide temperature range of the nematic phase; its clearing point is at  $T_{NI} = 75$  °C, and it remains nematic even at  $-5$  °C [82]. Our studies were done at 30 °C. Phase 5 exhibits  $\varepsilon_a < 0$  and  $\sigma_a > 0$  with sufficiently low magnitudes, thus it is one of the few compounds that can show both standard electroconvection and flexodomains as well.

Our studies of pattern formation were extended to the rod-like compound 1008 [P7] presented in Sec. 3.2.4 (Fig. 3.8). Finally we investigated the characteristics of flexodomains shown by the bent-core nematic liquid crystal ClPbis10BB (see Sec. 2.1 and Fig. 3.3).

All compounds were studied in standard planar cells (made by E.H.C. Co.) with the thickness of  $d = 11.3 \mu\text{m}$ ,  $d = 10.4 - 10.8 \mu\text{m}$ , and  $d = 11 \mu\text{m}$  in the case of Phase 5, 1008, and ClPbis10BB, respectively.

## 4. Results and discussion

### 4.1 Dielectric studies

#### 4.1.1 Thermal characterization of the phase behavior

In order to have the chance to compare appropriately the properties of liquid crystals with different phase behavior, all transition temperatures had to be determined. Most of the physical parameters in the nematic phase are scaled by the order parameter  $S$  that depends mainly not on the absolute  $T$ , but on the temperature relative to the clearing point. Thus a proper comparison between our LCs with different compositions had to be performed on similar relative temperatures ( $\Delta T = T - T_{NI}$ ).

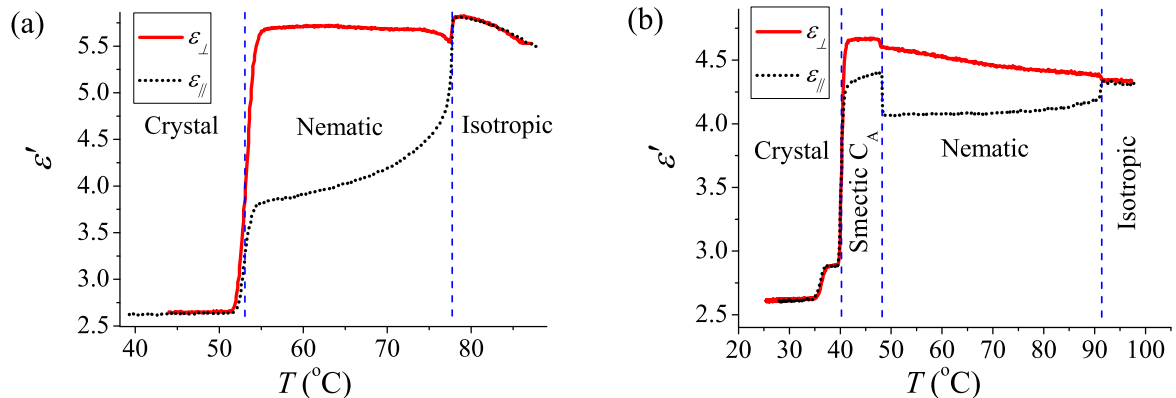


**Fig. 4.1:** The temperature dependence of  $\epsilon'_{\parallel}$  and of  $\epsilon'_{\perp}$  measured at  $f = 10$  kHz in the case of: (a) CIPbis10BB and (b) 6OO8. The phases were identified based on [79].

As representative examples, the temperature dependence of  $\epsilon'_{\parallel}$  and of  $\epsilon'_{\perp}$  measured at  $f = 10$  kHz are shown in the case of CIPbis10BB and of 6OO8 in Fig. 4.1(a) and (b), respectively. The phase transition temperatures can be precisely read from the data, since the dielectric constant depends strongly on the phases, however, the identification of the mesophases cannot be done using this dielectric technique. We marked the phases based on previous studies of the same compounds [79]. One can directly see in Fig. 4.1(a) that

CIPbis10BB exhibits a single (nematic) mesophase with a negative dielectric anisotropy, because  $\varepsilon_{\perp} > \varepsilon_{\parallel}$  stands in the whole nematic temperature range. In the case of 6OO8,  $\varepsilon_a$  is also negative and in addition to the isotropic-nematic transition, another first order phase transition could be observed from the nematic to the smectic-C mesophase at lower temperatures.

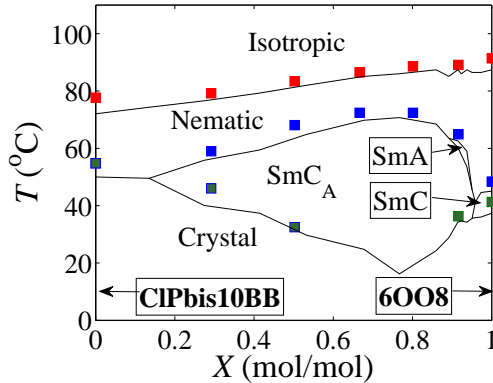


**Fig. 4.2:** The phase diagram of the CIPbis10BB-6OO8 binary system. The phase transition temperatures were determined from the dielectric studies (symbols) and by earlier investigations [79] using polarizing microscopy (solid lines). The phase identification is given according to [79].

The phase transitions were characterized similarly for all the different mixtures of 6OO8 and CIPbis10BB (Fig. 4.2). The phase diagram of the 6OO8-CIPbis10BB binary system can be seen in Fig. 4.2, where the molar fraction of 6OO8 in CIPbis10BB is denoted by  $X$ .  $X = 0$  corresponds to the pure bent-core compound CIPbis10BB and  $X = 1$  denotes the calamitic liquid crystal 6OO8. We note that the mixtures exhibit most probably the  $SmC_A$  phase below the nematic temperature range. ('A' refers to anticlinic that means the in-layer tilt direction is the opposite for neighboring SmC layers.) The phase diagram obtained shows good agreement with the previous studies [79] performed using polarizing microscopy on the same binary systems.

#### 4.1.2 Dielectric relaxations in the pure bent-core compound

The frequency dependence of  $\varepsilon'_{\parallel}$  and of  $\varepsilon''_{\parallel}$  in the case of the pure bent-core material (CIPbis10BB) is presented in Figs. 4.3(a) and 4.3(b), respectively, at different relative temperatures  $\Delta T = T - T_{NI}$  in the nematic phase [P1, P4].

Two relaxations can clearly be observed in the spectra: there are two inflection points in the  $\varepsilon'_{\parallel}(f)$  (Fig. 4.3(a)) at the same frequencies where two overlapping peaks are present in the dielectric loss spectra (Fig. 4.3(b)). The lower frequency (200 Hz - 100 kHz) one is referred to as  $BM_{\parallel 1}$ , while the one at higher frequencies (100 kHz - 4 MHz) is called  $BM_{\parallel 2}$  ( $BM$  refers to bent-core mode).

The increase in the dielectric loss at the lowest frequencies is due to the DC conductivity of the sample (see. Sec. 1.2.5 and Fig. 1.7). This effect is more prominent at higher temperatures, since the conductivity of the liquid crystal increases with the temperature. In Fig. 4.3(c), the dielectric spectra are presented in a Cole-Cole diagram, where the two relaxations appear as two arcs.

The spectra were fitted using Eq. (1.21) and Eq. (1.22) assuming  $k = 2$  (solid lines in Fig. 4.3). The complex nonlinear least squares method (see. Sec. 1.2.5) was used in order to get the values of the relevant parameters of the relaxations. Preliminary fitting results showed that  $BM_{\parallel 1}$  can well be described by an ideal Debye-type relaxation ( $\alpha_{BM_{\parallel 1}} \approx 0 \pm 0.05$ ), thus for the sake of the fit's stability, the parameter  $\alpha_{BM_{\parallel 1}}$  was later fixed to zero. In contrast to  $BM_{\parallel 1}$ ,  $BM_{\parallel 2}$  is clearly different, the corresponding symmetrical distribution parameter  $\alpha_{BM_{\parallel 2}} \approx 0.26 - 0.31$  that means it is Cole-Cole type: the relaxation is a sum of processes with slightly different relaxation frequencies.

The dielectric increment of  $BM_{\parallel 1}$  and  $BM_{\parallel 2}$  are also considerably different:  $\Delta\varepsilon_{BM_{\parallel 1}} \approx 0.27 - 0.36$  and  $\Delta\varepsilon_{BM_{\parallel 2}} \approx 1.3 - 2.3$ . Furthermore, both  $\Delta\varepsilon_{BM_{\parallel 1}}$  and  $\Delta\varepsilon_{BM_{\parallel 2}}$  become smaller with decreasing temperatures.

At higher frequencies, the fitted curves deviate from the experimental data points that indicates the onset of an additional relaxation ( $BM_{\parallel 3}$ ) lying above the frequency range of our measurements.

The existence of the relaxation  $BM_{\parallel 3}$  is further supported by the fact that the value of  $\varepsilon_{\parallel}(\infty)$ , obtained from the fit assuming two relaxations, is too high compared to  $n_e^2$ . Assuming  $n_e = 1.6$ ,  $\varepsilon_{\parallel}(\infty) - n_e^2 \simeq 1.3$  (at  $\Delta T = -13$  K). Relevant processes in the infrared regime contribute to the dielectric constant usually up to 5-10 % of  $n^2$  [83] in calamitics, thus the value of 1.3 is too high to attribute it only to the infrared modes.

The perpendicular components  $\varepsilon'_{\perp}(f)$  and  $\varepsilon''_{\perp}(f)$  are presented in Figs. 4.4(a) and 4.4(b), respectively, for several temperatures. The corresponding Cole-Cole plots can be seen in Fig. 4.4(c). Here the experimental data show only one relaxation ( $BM_{\perp 1}$ ) in

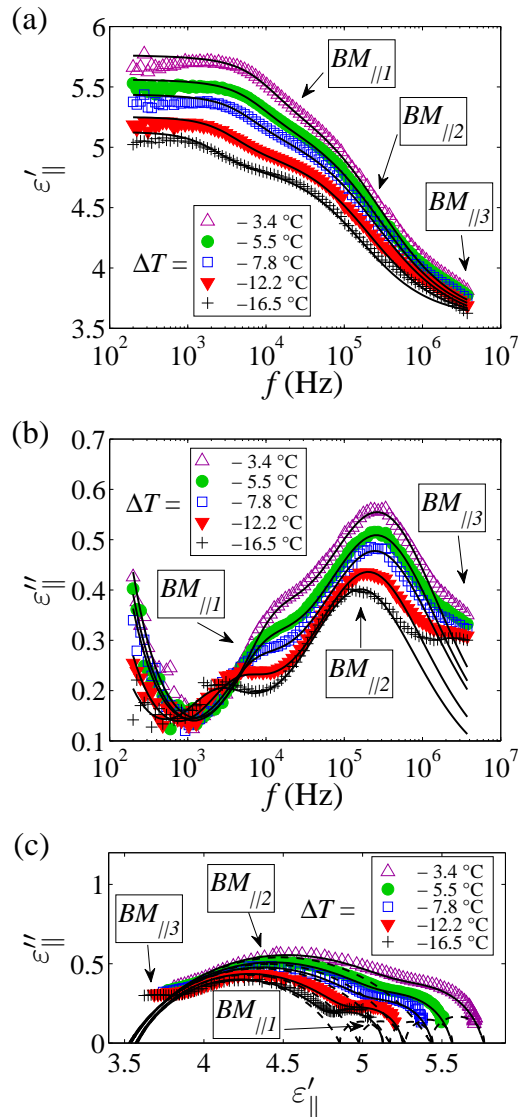


**Fig. 4.3:** (a) The parallel component of the relative dielectric permittivity ( $\epsilon'_{||}$ ) and (b) the dielectric loss ( $\epsilon''_{||}$ ) as the function of frequency in the nematic phase of the bent-core compound CIPbis10BB at different  $\Delta T = T - T_{NI}$  temperatures. (c) The Cole-Cole plot of the dielectric spectra. The symbols are measured values, the solid lines correspond to fits with two relaxations. The dashed lines show the two fitted relaxations separately.

the higher frequency part (100 kHz - 4 MHz) of the measurement range. In contrast to the relaxation  $BM_{||2}$ , the dielectric increment of  $BM_{||1}$  does not decrease significantly towards lower temperatures. The maximum of the loss peak for  $BM_{||1}$  is significantly larger than that of  $BM_{||2}$ . The onset of an additional relaxation ( $BM_{||2}$ ) above 4 MHz is also visible here, similarly to the case of the parallel component. The deviations of the fitted curves from the measurement data are more spectacular at lower temperatures,

in accordance to that  $f_{BM\parallel 2}$  decreases and approaches the studied  $f$ -range. Moreover  $\varepsilon_{\perp}(\infty) - n_o^2 \simeq 2$  (at  $\Delta T = -13$  K) here is even larger than in the  $\parallel$  component. Furthermore,  $\varepsilon_a$  was found to be negative even at 4 MHz, while at optical frequencies the anisotropy should have the opposite sign ( $n_a > 0$ ).

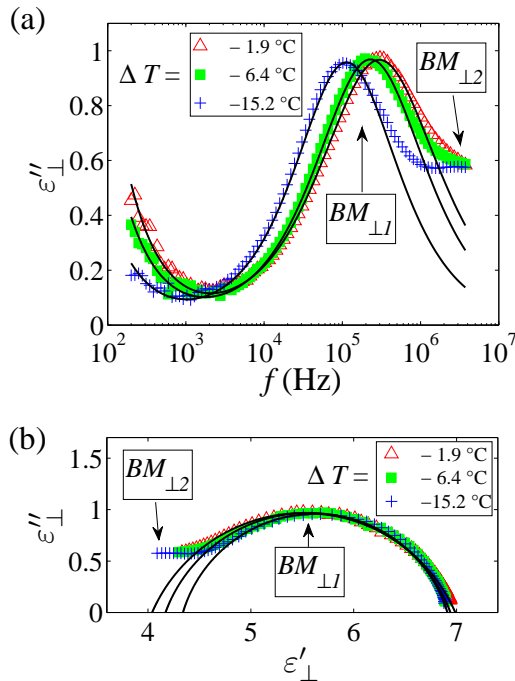


**Fig. 4.4:** (a) The perpendicular component of the dielectric loss ( $\varepsilon''_{\perp}$ ) as the function of frequency in the nematic phase of the bent-core compound CIPbis10BB at different  $\Delta T = T - T_{NI}$  temperatures. (b) The Cole-Cole plot of the dielectric spectra. The symbols are measured values, the solid lines correspond to fits with one relaxation.

The static dielectric anisotropies at different temperatures could be calculated using the fit parameters of the dielectric spectra.  $\varepsilon_a$  as the function of temperature is presented in Fig. 4.5. It can well be seen that  $\varepsilon_a$  is negative, and decreasing at lower temperatures.

The dynamic dielectric behavior was studied also in the isotropic phase of CIPbis10BB. The results can be seen in Fig. 4.6. The spectra show one strong relaxation ( $BM_{iso1}$ ) with the characteristic frequency increasing with the temperature from 200 kHz to 500 kHz in the measured  $T$ -range, while  $\Delta\varepsilon_{BM_{iso1}}$  reduces from 3.7 to 2.8.  $BM_{iso1}$  is of Cole-Cole type:  $\alpha_{BM_{iso1}}$  is decreasing from 0.38 to 0.23 when increasing the temperature above the clearing point.

The relaxation frequencies of  $BM_{iso1}$  lie in an unusually low range for an isotropic relaxation. High frequency deviations from the fit curves of  $BM_{iso1}$  are also present, how-

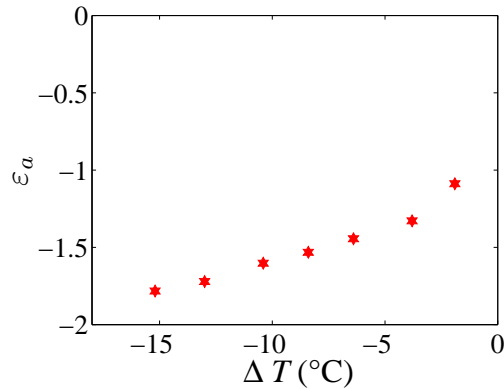


**Fig. 4.5:** The static dielectric anisotropy  $\varepsilon_a$  as the function of the relative temperature  $\Delta T = T - T_{NI}$  in the nematic phase of the bent-core compound ClPbis10BB.

ever, the effect is not as strong as it was experienced in the nematic phase. Nevertheless the deficiency in the dielectric constant appears not to be negligible:  $\varepsilon_{iso}(\infty) - n_{iso}^2 \simeq 1.4$  (at  $\Delta T = 5$  K). This refers to the presence of an additional relaxation ( $BM_{iso2}$ ) at frequencies higher than 4 MHz.

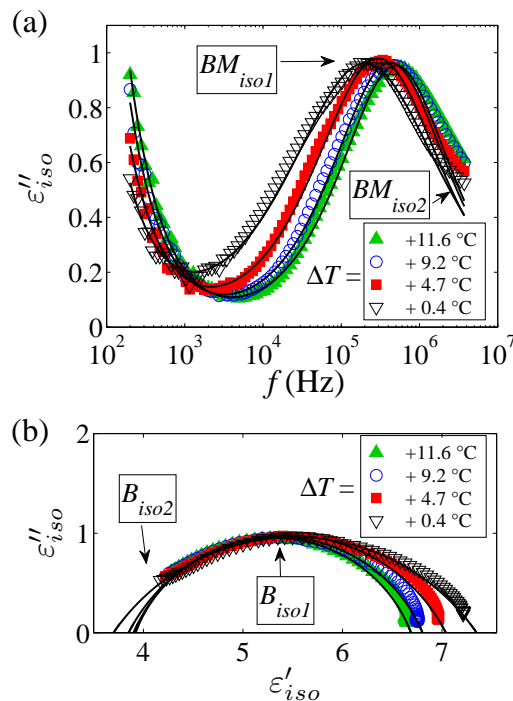


**Fig. 4.6:** (a) The dielectric loss ( $\varepsilon''_{iso}$ ) as the function of frequency in the isotropic phase of the bent-core compound ClPbis10BB at different  $\Delta T = T - T_{NI}$  temperatures. (b) The Cole-Cole plot of the dielectric spectra. The symbols are measured values, the solid lines correspond to fits with one relaxation.

The temperature dependence of the relaxation frequencies in both the isotropic and the nematic phase can well be described by the Arrhenius-equation (Eq. (1.26)) that is visualized in the Arrhenius-plot. In Fig. 4.7, the relaxation frequencies of the different modes (in logarithmic scale) are plotted as the function of the inverted absolute temperature ( $1/T$ ). The linear dependences in this representation support the Arrhenius-behavior of the relaxations. Nevertheless one might notice a slight nonlinear tendency in the case of  $BM_{\parallel 2}$ . The activation energies ( $E_A$ ) could be obtained by fits (straight lines in Fig. 4.7), resulting 1.1 eV, 0.4 eV, 0.7 eV, and 0.9 eV for  $BM_{\parallel 1}$ ,  $BM_{\parallel 2}$ ,  $BM_{\perp 1}$ , and for  $BM_{iso1}$ , respectively. The values are relatively high (especially the 1.1 eV for  $BM_{\parallel 1}$ ), but they fall in the regular ranges compared to calamitics.

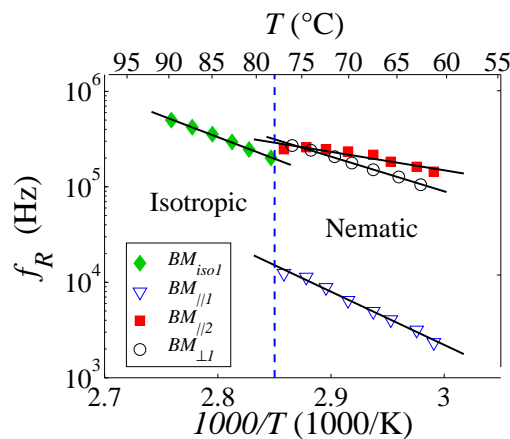


**Fig. 4.7:** The temperature dependence of the relaxation frequencies in the isotropic and nematic phases of the bent-core compound ClPbis10BB. The symbols are measured values, the solid lines correspond to fits with Eq. (1.26).

The fit parameters of the different relaxation modes in ClPbis10BB at selected temperatures ( $\Delta T = +5$  K in the isotropic and  $\Delta T = -13$  K in the nematic phase) are collected in Table 4.1. The activation energies determined for each relaxation are also shown in Table 4.1.

### 4.1.3 Dielectric relaxations in the mixtures

In order to explore the transition from the unusual dielectric behavior of the bent-core to the regular characteristics of a common rod-like compound, the dielectric spectra of the binary mixtures of 6OO8 and ClPbis10BB were studied [P1]. The frequency

Relaxations	$\Delta\varepsilon$	$f_R$ (kHz)	$\alpha$	$\varepsilon(\infty)$	$E_A$ (eV)
$BM_{iso1}$	3.2	310	0.3	3.8	0.9
$BM_{iso2}$	$<1.4$ ( $\simeq \varepsilon_{iso1}(\infty) - n_{iso}^2$ )	$>4000$	-	$> n_{iso}^2$	-
$BM_{\parallel 1}$	0.27	3.7	0		1.1
$BM_{\parallel 2}$	1.4	210	0.3	3.6	0.4
$BM_{\parallel 3}$	$<1.3$ ( $\simeq \varepsilon_{\parallel}(\infty) - n_e^2$ )	$>4000$	-	$> n_e^2$	-
$BM_{\perp 1}$	2.7	140	0.2	4.3	0.7
$BM_{\perp 2}$	$<2$ ( $\simeq \varepsilon_{\perp}(\infty) - n_o^2$ )	$>4000$	-	$> n_o^2$	-

**Table 4.1:** The fitted values of the dielectric increment  $\Delta\varepsilon$ , the relaxation frequency  $f_R$ , the symmetrical distribution parameter  $\alpha$ , the asymptotic permittivity  $\varepsilon(\infty)$ , and the activation energy  $E_A$  for the relaxation modes found in the bent-core compound ClPbis10BB. The values were determined at  $\Delta T = T - T_{NI} = +5$  °C in the isotropic and at  $\Delta T = -13$  °C in the nematic phase.

dependence of  $\varepsilon'_{\parallel}$  and of  $\varepsilon''_{\parallel}$  for different concentration but at the same  $\Delta T = -13$  °C relative temperature are presented in Figs. 4.8(a) and 4.8(b), respectively.

The dielectric permittivities at the lowest frequencies ( $f \sim 200$  Hz) of our measurement range equal to the static dielectric constant with a good approximation. In Fig. 4.8(a), it can be followed that  $\varepsilon'_{\parallel}(200 \text{ Hz})$  changes monotonically with  $X$  in the mixtures from one pure compound to the other.

The different relaxations can easier be distinguished by looking at the loss spectra. The  $\parallel$  and  $\perp$  components of the dielectric loss as the function of frequency can be seen in Figs. 4.8(b) and 4.9, measured at  $\Delta T = -13$  °C, for the different concentrations.

The parameters of the dielectric relaxations were determined from fits (solid lines in the spectra) using the same technique described previously. The fit parameters  $\Delta\varepsilon$ ,  $\alpha$ , and  $f_R$ , are plotted as the function of  $X$  in Figs. 4.10(a), (b), and (c), respectively. The role of the lines in these figures will be discussed later.

In the mixtures, the dielectric studies were extended to the  $\text{SmC}_A$  phase as well, in order to see the relations between the relaxations observed in the different mesophases. As an example, the parallel and perpendicular dielectric loss spectra measured in the  $\text{SmC}_A$  phase at  $X = 0.5$  concentration are shown in Fig. 4.11. One strong relaxation ( $MM_{\text{Sm}\parallel}$ ) ( $M$  refers to the relaxations in the mixtures) can be seen in the  $\parallel$  component around 30 kHz. The  $\perp$  spectrum, however, shows only a very small absorption peak at the same  $f$ , which is assumed to be a crosstalk of  $MM_{\text{Sm}\parallel}$ . Beginning from 1 MHz,

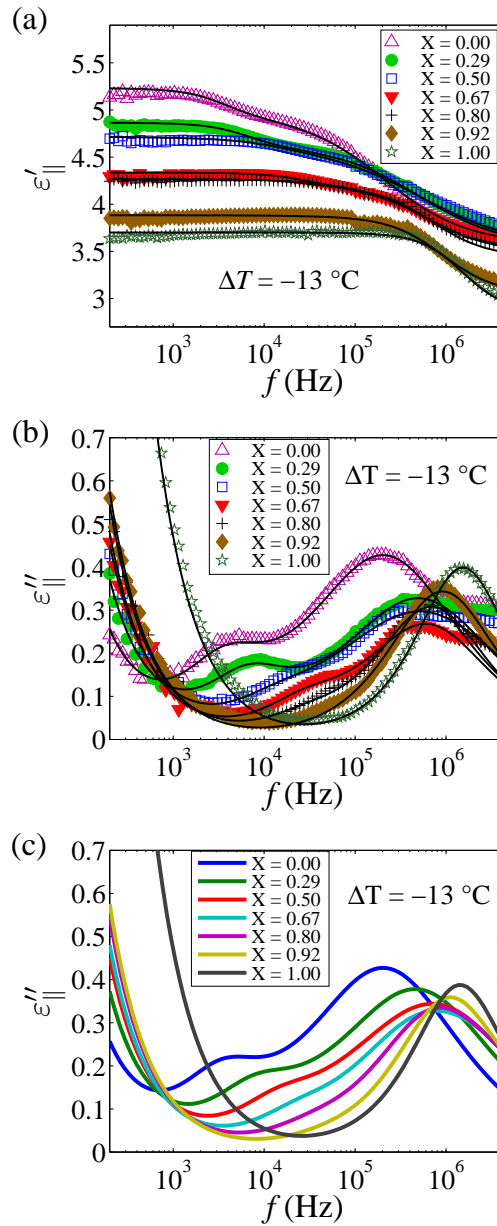


**Fig. 4.8:** (a) The parallel component of the relative dielectric permittivity ( $\epsilon'_{||}$ ) and (b) the dielectric loss ( $\epsilon''_{||}$ ) as the function of frequency in the nematic phase at  $\Delta T = T - T_{NI} = -13$  °C in the CIPbis10BB-6OO8 mixtures at various molar concentrations ( $X$ ) of the rod-like compound. The symbols are measured values, the solid lines correspond to fits with two relaxations. (c) The synthesized spectra of  $\epsilon''_{||}$  at various  $X$  concentrations assuming three relaxations. Detailed description can be found in the text.

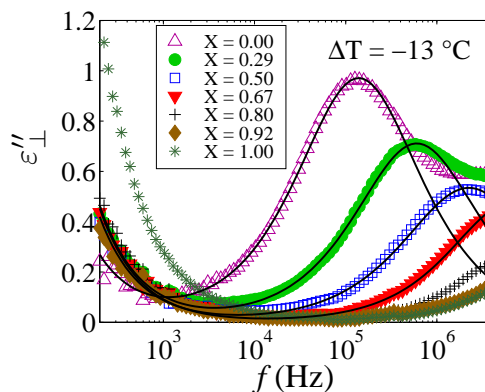


**Fig. 4.9:** The perpendicular component of the dielectric loss ( $\varepsilon''_{\perp}$ ) as the function of frequency in the nematic phase at  $\Delta T = T - T_{NI} = -13$  °C in the ClPbis10BB-6008 mixtures at various molar concentrations ( $X$ ) of the rod-like compound. The symbols are measured values, the solid lines correspond to fits with one relaxation.

the increase of  $\varepsilon''$  indicates the presence of relaxations at higher frequencies beyond the measurement range in both the  $\parallel$  and  $\perp$  components.

For the selected concentration  $X = 0.5$ , the Arrhenius-plot of the different relaxations is presented in Fig. 4.12. Similarly to the case of ClPbis10BB, all relaxation modes follow the Arrhenius-behavior; the fits of Eq. 1.26 are represented by solid lines in Fig. 4.12. The activation energy was found to be 0.5 eV for the relaxation in the isotropic phase ( $MM_{iso}$ ), similarly for the perpendicular mode in the nematic phase ( $MM_{\perp}$ ). The lower ( $MM_{\parallel 1}$ ) and higher ( $MM_{\parallel 2}$ ) frequency mode in the parallel component of the nematic phase exhibit  $E_A = 1.6$  eV and  $E_A = 0.8$  eV, respectively. The activation energy of  $MM_{Sm\parallel}$  is also relatively large: 1.3 eV. It is noticeable that the isotropic relaxation  $MM_{iso}$  of the mixture with  $X = 0.5$  shows five times lower activation energy than that of the pure bent-core material ( $BM_{iso1}$ ). The activation energies of  $MM_{\parallel 1}$  and of  $MM_{\parallel 2}$  were found to be larger compared to those of  $BM_{\parallel 1}$  and  $BM_{\parallel 2}$ .

The fit parameters of the different relaxations in the case of the mixture with  $X = 0.5$  at  $\Delta T = +5$  K in the isotropic,  $\Delta T = -13$  K in the nematic, and  $\Delta T = -30$  K in the  $SmC_A$  phase are collected in Table 4.2. The corresponding activation energies are also presented in Table 4.2.

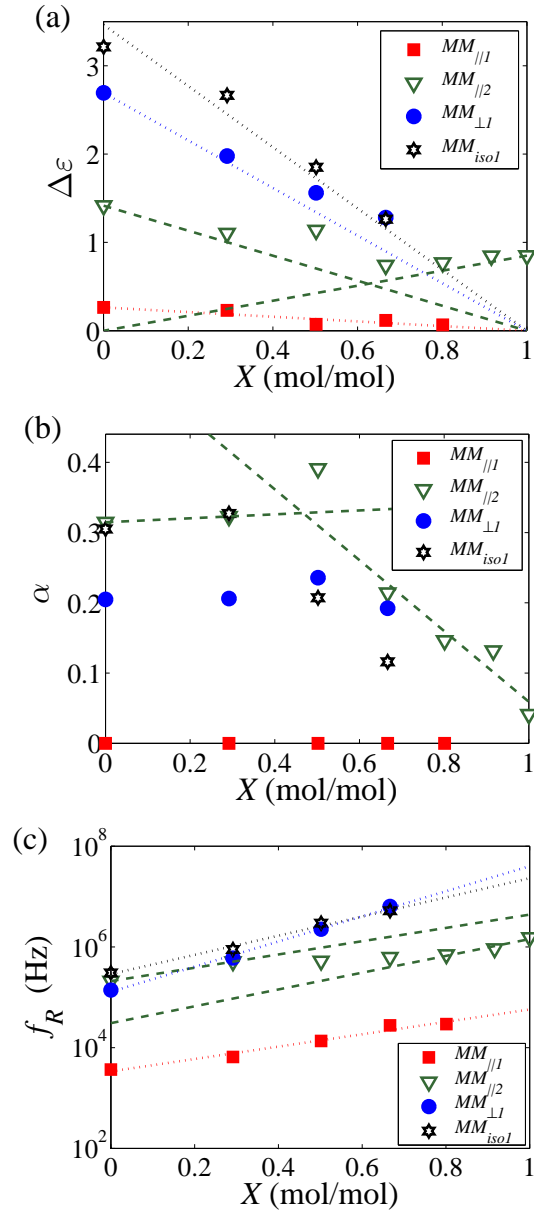


**Fig. 4.10:** The molar concentration ( $X$ ) dependence of (a) the dielectric increments  $\Delta\varepsilon$ , (b) the symmetric distribution parameters  $\alpha$ , and (c) the relaxation frequencies  $f_R$  of the relaxation modes ( $MM$ ) in the mixtures of CIPbis10BB-6008 at the relative temperatures  $\Delta T = T - T_{NI} = +5$  °C and  $-13$  °C, in the isotropic and in the nematic phase, respectively. The dotted lines show linear extrapolations for the  $X$ -dependence. The two dashed lines indicate a decomposition of  $MM_{//2}$  into two relaxations discussed in Sec. 4.1.5.

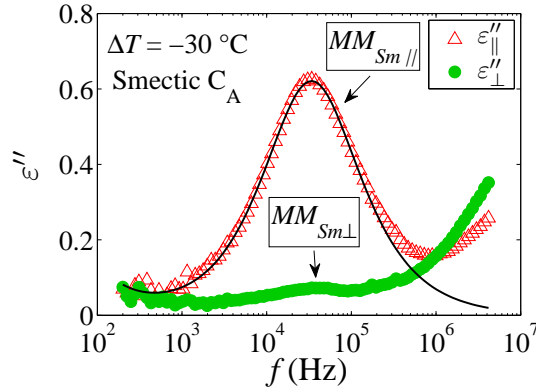


**Fig. 4.11:** The frequency dependence of the perpendicular ( $\varepsilon''_{\perp}$ ) and the parallel ( $\varepsilon''_{\parallel}$ ) components of the dielectric loss in the  $\text{SmC}_A$  phase of the mixture with  $X = 0.5$  molar fraction of 6OO8 in ClPbis10BB at  $\Delta T = T - T_{NI} = -30$  °C. The symbols are measured values and the solid line corresponds to a fit with one relaxation.

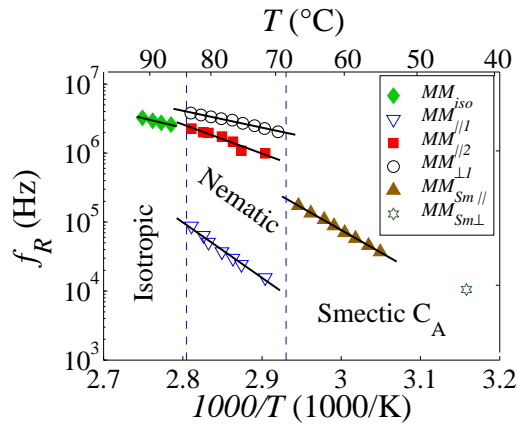


**Fig. 4.12:** The temperature dependence of the relaxation frequencies in the isotropic, nematic, and the smectic phases of the mixture with  $X = 0.5$  molar fraction of 6OO8 in ClPbis10BB. The symbols are measured values, the solid lines correspond to fits with Eq. 1.26.

#### 4.1.4 Calculations of molecular dipole moments

In Sec. 1.2.4 and Sec. 1.2.5, the theoretical formulae were presented that could be used to compare our experimental findings with molecular properties. All available theories were created to describe media consisting of rigid molecules with relatively high symmetry, namely spherical (Onsager, Debye) or uniaxial (Maier-Meier) ones. In the case of the Maier-Meier molecular theory (Eq. 1.11), where the molecules are considered as elongated ellipsoids of revolution, fixed single dipoles (the net dipole moment) were assumed that are bound to the ellipsoids at an angle of  $\beta_m$  with respect to the long axis.

Relaxations	$\Delta\varepsilon$	$f_R$ (kHz)	$\alpha$	$\varepsilon(\infty)$	$E_A$ (eV)
$MM_{iso}$	1.9	3000	0.2	3.8	0.5
$MM_{\parallel 1}$	0.1	14	0		1.6
$MM_{\parallel 2}$	1.1	530	0.4	3.5	0.8
$MM_{\perp 1}$	1.6	2200	0.2	4	0.5
$MM_{Sm\parallel}$	1.5	37	0.1	4.1	1.3

**Table 4.2:** The fitted values of the dielectric increment  $\Delta\varepsilon$ , the relaxation frequency  $f_R$ , the symmetric distribution parameter  $\alpha$ , the asymptotic permittivity  $\varepsilon(\infty)$ , and the activation energy  $E_A$  for the relaxation modes found in the mixture with  $X = 0.5$  molar fraction of 6OO8 in CIPbis10BB. The values were determined at  $\Delta T = T - T_{NI} = +5$  °C in the isotropic, at  $\Delta T = -13$  °C in the nematic, and at  $\Delta T = -30$  °C in the smectic phase.

Equation (1.11) connects  $\beta_m$  with  $\varepsilon_a$ , and at least one could check if the sign of the measured dielectric anisotropy is compatible with the calculated one or not. Furthermore, the Onsager-equation (Eq. 1.24) could be used to check the consistency between the measured dielectric increment of the relaxation in the isotropic phase and the absolute value of the molecular dipole moment.

In order to perform the comparison with the theories presented above, one has to calculate the absolute value of the dipole moment and the direction of it with respect to the long molecular axis. We performed the calculations by using the Hyperchem 8 software made for quantum chemical calculations, and Matlab [P1].

The bent-core molecule CIPbis10BB has seven polar groups related to the Cl-, -COO-, and the -O- bonds. Various parts of the molecules can easily rotate around the numerous sigma bonds, thus not only the net dipole moment, but even the molecular shape (and thus  $\beta_m$ ) depends strongly on the actual conformation of the molecule.

Defining the long axis of the bent-core molecules is more problematic than in the case of calamitics. In order to have consistency, we employed a general method for the determination of the long molecular axis that can be applied to bent-cores and to rod-like molecules as well. First the inertial tensor of the molecule is calculated using the atomic masses and positions in a given conformation. Then the long molecular axis is assigned to the eigendirection that belongs to the smallest eigenvalue of the inertial tensor. This definition consistently results in the usual long axis direction for rod-like molecules.

The different molecules were assembled in Hyperchem using their known configuration of atoms. The energy of a given molecular geometry was calculated by the semi-

empirical quantum-chemical method RM1. Then the Polak-Ribiere conjugate gradient optimization algorithm was used to find the local energy minimum that corresponds to a molecular conformation. Since the optimization method is sensitive to the initial conditions, namely the initially given molecular structure, the following procedure was utilized to explore the conformational space in order to find conformers with lower energies. Torsions by random angles in the range of  $\pm 60^\circ - 120^\circ$  were introduced into the molecules at predefined bonds: for ClPbis10BB at 4 places around the 4 bonds between the oxygen of the carboxyl-group and the carbon of the neighboring benzene ring; for 6OO8 at 2 places around the bonds that connect the aromatic rings to the central carboxyl-group. After the torsions, a geometry optimization was performed that resulted in a conformer. Then the loop with the new set of random torsions was continued. After each cycle, the conformation (with all the parameters, e.g. atomic positions, dipole moments) was saved if its energy and geometry was different than the others saved previously. The algorithm was stopped after 1000 different conformers were found. The long molecular axis was determined for the set of conformers, thus  $\beta_m$  could be obtained for each conformation. An average  $\beta_m$  and  $\mu_m$  was calculated by Boltzmann-averaging over all the conformations at a given temperature.

The results of the conformational calculations showed that besides the lowest energy conformer there are other conformations with the energy differences within the range of the thermal energy  $k_B T$ . Though the energies of these conformers are close to each other, the resulting dipole moments could be significantly different in their magnitudes ( $\mu_m \approx 3 - 7$  D) and their directions with respect to the long molecular axis ( $\beta_m \approx 60^\circ - 88^\circ$ ) as well. Since these conformers can coexist at a given temperature due to the relatively small energy difference, a Boltzmann-average is thought to give a better value for  $\mu_m$  and  $\beta_m$ , than considering only the lowest energy conformer that is usually done in the literature (e.g. [59]). Nevertheless, using the  $\mu_m$ ,  $\beta_m$  values of only a single conformation instead of an average can be adequate in the case of simple rod-like molecules with much lower conformational freedom [24].

In the case of ClPbis10BB, the calculations with Boltzmann-averaging of the longitudinal and transversal dipole moments performed at  $T = 360$  K ( $\Delta T \approx 10$  K) resulted in  $\mu_m = 5.5$  D and  $\beta_m = 74^\circ$ . As an illustration, the three dimensional structure of the lowest energy conformer of ClPbis10BB is presented in Fig. 4.13.

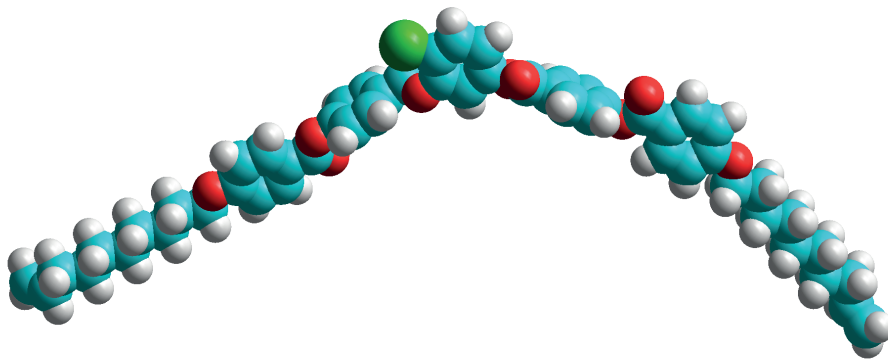


**Fig. 4.13:** The lowest energy conformer of ClPbis10BB calculated by Hyperchem 8.

Earlier calculations [59] considered only the most stable conformer of ClPbis10BB, and the resulting  $\mu_m$  and  $\beta_m$  were found to be significantly smaller, than the values given above by the Boltzmann-averaging. The smaller values of  $\mu_m$  and of  $\beta_m$  are not compatible with the large negative dielectric anisotropy ( $\varepsilon_a \simeq -1.7$ ) shown by the dielectric measurements presented in Sec. 4.1.2. The present calculations are assumed to be more precise due to usage of a more sophisticated quantum-chemical method (the RM1 instead of the AM1) combined with the Boltzmann-averaging over a number of conformers. Indeed, the value of  $\beta_m = 74^\circ$  determined from the Boltzmann-averaging is in accordance with the requirement for  $\varepsilon_a < 0$  of Eq. (1.11) ( $\beta_m > 54.7^\circ$ ).

The dipole moment calculations were done for the rod-like compound 6OO8 as well, at the same  $T = 360$  K ( $\Delta T \approx -4$  K) resulting in  $\mu_m = 2.7$  D and  $\beta_m = 63^\circ$ .

It has to be noted, however, that the quantum-chemical calculations were done *in vacuo*, meaning that all molecular interactions were neglected. More realistic calculations could be done by taking into account the interaction of the molecules that would probably affect the conformations especially in the anisotropic (meso)phases.

#### 4.1.5 Discussion

The characteristic frequency of the relaxation in the isotropic phase in 6OO8 and in the mixtures with large concentrations of the rod-like compound ( $X > 0.67$ ) lies above 4 MHz, thus only the onset of the corresponding loss peak could be detected in our measurements [P1]. In the case of smaller values of  $X$ , however, the isotropic relaxation frequency shifts gradually down to  $f_{B_{iso1}} \approx 300$  kHz, until it reaches the concentration of the pure ClPbis10BB ( $X = 0$ ) as it can be seen in Fig. 4.10(c). Such low  $f_R$  is unusual

in the isotropic phase, though it can be understood by considering that the isotropic viscosity of the bent-core compound is about 1-2 orders of magnitude larger than that of the usual rod-like compounds [71]. Furthermore, the significantly larger size of the bent-core molecule can also have a reducing effect on the relaxation frequency according to Debye's theory discussed in Sec. 1.2.5.

The relation between the dielectric increment of  $BM_{iso1}$  and the calculated molecular dipole moment is analyzed using the Onsager-equation (Eq. (1.24)) at  $\Delta T = +5$  K. The number density of the molecules ( $N$  in Eq. (1.24)) can be calculated using the molar weight and assuming that the density equals to  $1000 \text{ kg/m}^3$ . The experimental results indicated that there are two relaxations in the isotropic phase of ClPbis10BB. The one at lower frequencies ( $BM_{iso1}$ ) lies around 0.3 MHz and exhibits  $\Delta\epsilon_{BM_{iso1}} = 3.2$  and  $\alpha_{BM_{iso1}} = 0.3$ . Using these values, the Onsager-equation gives 3.6 D for the effective dipole moment contributing to the relaxation mode  $BM_{iso1}$ . The value of 3.6 D is lower than the  $\mu_m$  obtained from the quantum-chemical calculations, thus the resulting Kirkwood-Fröhlich factor (Eq. (1.25)) is  $g = 0.4$ .

The dielectric increment of the relaxation at higher frequencies, above our measurement range ( $BM_{iso2}$ ), is approximated by considering all the contributions in the dielectric constant up to the optical frequencies. In such way the value  $\Delta\epsilon_{BM_{iso2}} \simeq 1.4$  is obtained. This relaxation might account for the intramolecular rotations of the 7 polar groups within the bent-core molecule. The sum of two increments  $\Delta\epsilon_{BM_{iso1}} + \Delta\epsilon_{BM_{iso2}} = 4.6$  results in  $\mu_{eff} = 5.6$  D, which is very close to the calculated  $\mu_m$ .

The measurements on 6OO8 at  $\Delta T = -13$  °C clearly showed a Debye-type relaxation ( $\alpha_{CM_{\parallel 1}} = 0.04$ ) with  $f_{CM_{\parallel 1}} = 1.5$  MHz. This mode can be attributed to the reorientation around the short axis of the molecule ( $CM_{\parallel 1}$ ) without any doubt. The additional calamitic relaxations ( $CM_{\parallel 2}$  and  $CM_{\perp}$ ) are expected to occur at higher frequencies in accordance with our experiments, where we found only the onset of these at the highest part of the frequency range used.

Results of dielectric studies on 6OO8 can be found in the literature [84] as well, however, there mainly the findings in the SmC phase were emphasized. The data published showed one relaxation at 1.6 MHz in the parallel component, 10 °C below the nematic isotropic phase transition that is in good agreement with our results.

Relaxation phenomena in 6OO8 were not investigated at frequencies higher than 10 MHz. Nevertheless, a similar compound 4-n-decyloxyphenyl 4-n-hexyloxybenzoate (10OO6 or DOBHOP) was the subject of dielectric spectroscopy measurements up to the GHz range [85]. The difference between 10OO6 and 6OO8 is only in the length of the terminal alkyl chains, thus the physical properties of these compounds are assumed to be very similar. In the studies of 10OO8, all characteristic calamitic modes ( $CM_{\parallel 1}$ ,  $CM_{\parallel 2}$ , and  $CM_{\perp 1}$ ) were found with the following parameters measured at  $\Delta T = -4K$ :  $f_{CM_{\parallel 1}} \approx 1.8$  MHz (Debye type),  $f_{CM_{\parallel 2}} \approx 500$  MHz (Cole-Cole type), and  $f_{CM_{\perp}} \approx 400$  MHz (Cole-Cole type). Our findings on 6OO8 are also in good agreement with these. The dielectric parameters from our measurements and from the literature are collected in Table 4.3 for the rod-like mesogens 6OO8 and 10OO6.

Relaxations	$\Delta\varepsilon$	$f_R$ (MHz)	$\alpha$	$\varepsilon(\infty)$	$E_A$ (eV)
$CM_{\parallel 1}$	0.85	1.5 (1.6 <sup>†</sup> and 1.8 <sup>‡</sup> )	0	2.9	1
$CM_{\parallel 2}$	-	(500 <sup>‡</sup> )	-	-	-
$CM_{\perp}$	-	(400 <sup>‡</sup> )	-	-	-

<sup>†</sup> Approximate value for 6OO8 at  $\Delta T = -10$  K from [84]

<sup>‡</sup> Approximate values for 10OO6 at  $\Delta T = -4$  K from [85]

**Table 4.3:** The dielectric increment  $\Delta\varepsilon$ , the relaxation frequency  $f_R$ , the symmetric distribution parameter  $\alpha$ , the asymptotic permittivity  $\varepsilon(\infty)$ , and the activation energy  $E_A$  for the relaxations of 6OO8 measured at  $\Delta T = -13$  °C. The literature data for the relaxation frequencies of 6OO8 [84] and of 10OO6 [85] are also presented.

The dielectric behavior of the pure ClPbis10BB is quite different from the case of the rod-like compounds. The most obvious difference is that five relaxations ( $BM_{\parallel 1}$ ,  $BM_{\parallel 2}$ ,  $BM_{\parallel 3}$ ,  $BM_{\perp 1}$ , and  $BM_{\perp 2}$ ) can be observed separately in the nematic phase of ClPbis10BB instead of the usual three ( $CM_{\parallel 1}$ ,  $CM_{\parallel 2}$ , and  $CM_{\perp 1}$ ). Furthermore, some of the modes (e.g.  $BM_{\parallel 1}$ ) occur in an unusually low frequency range [P1, P4].

The unusual behavior of ClPbis10BB might be explained by its different molecular symmetry compared to that of calamitics. The theoretical models [23, 24, 27, 28, 29] developed to describe the relaxation modes in calamitics are in agreement with the experiments using rod-like compounds. Nevertheless, the basic assumptions of the polar rod models, namely the molecules are considered as rigid and uniaxial ellipsoids, are not satisfied in the case of bent-cores. The conformational studies of ClPbis10BB (see. Sec. 4.1.4) showed that such bent-core molecule is not rigid at all, since several signif-

icantly different conformations exist with relatively small energy differences, moreover the polar groups in the structure can rotate that results in a conformation dependent net dipole moment. The other important argument against the applicability of polar rod models on CIPbis10BB is that the symmetry of the bent-core molecules is rather biaxial, not uniaxial. Consequently the number of equivalent rotation axes are decreased compared to calamitics, which could lead to the appearance of more dielectric relaxations.

The arguments above make clear that a new theoretical description should be developed to explain the unusual dielectric properties of CIPbis10BB, just as it happened for the case of liquid crystalline dimers [86, 87].

Nevertheless, alternative explanations for especially the lowest frequency relaxation  $BM_{\parallel 1}$  could be also imagined. The frequency range of  $BM_{\parallel 1}$  coincides to that of the collective modes observed in smectics. Recent small angle x-ray studies [66, 88, 89, 90] showed polar smectic-like clusters in bent-core nematics that could exhibit dielectric relaxations at around a few kHz. Their volume concentration was estimated as around a few percents, however that might be enough to produce a relaxation with a low dielectric increment such as  $BM_{\parallel 1}$ .

The activation energies of the relaxation modes in the nematic phase of CIPbis10BB (see Table 4.1) are considerably different, indicating that a distinct process accounts for each relaxation. Due to the lack of an adequate theoretical description, it is not clarified, what kind of molecular, intramolecular or collective motions are exactly responsible for the relaxations observed. Consequently, neither the temperature dependence of the relaxation frequencies of the different modes can be interpreted clearly. The  $BM_{\parallel 2}$  mode exhibits a minor deviation from the Arrhenius-rule (See Fig. 4.7) in the vicinity of the isotropic-nematic phase transition, where the nematic order parameter has the highest temperature dependence. This might indicate that  $BM_{\parallel 2}$  includes a molecular process, which depends more on the nematic order than the ones contributing in the other relaxations.

In order to understand the relaxations in the mixtures, it has to be assumed that the bulk properties, like the static dielectric constant and the viscosities, change monotonically with the concentration. The approximately linear concentration dependence of the dielectric constant at 200 Hz can be seen in Fig. 4.8(a). The viscosities of the mixtures, however, show a stronger exponential dependence on the molar fraction if the

difference between the viscosities of the pure components is large [91]. This requirement is absolutely fulfilled in our system, since the viscosity of the bent-core is 1-2 orders of magnitude larger than that of the rod-like compound.

The characteristic frequencies of relaxation modes connected to molecular motions are strongly affected both by properties of the bulk (e.g. viscosities) and of the individual molecules (e.g. size, dipole moment) according to the qualitative description of Debye (see Sec. 1.2.5). Equation (1.23) shows that the relaxation frequency is lower in the case of larger molecular size and higher viscosity. Qualitatively the results of Debye are easy to understand: a larger molecule can be reoriented by a lower rate, because it needs to pass a higher energy barrier to move; the higher viscosity corresponds to an environment that also makes the molecular motions more hindered.

In the binary system of 6OO8-CIPbis10BB, the molecular sizes of the components are significantly different, thus the relaxations originated from 6OO8 and CIPbis10BB might be observed separately. This idea of interpreting relaxations in a mixture as the superposition of the different modes originating from the various components was considered in earlier studies of rod-like liquid crystals [91, 92]. In mixtures of calamitics, however, the relaxations from the different components could not be observed separately, because the corresponding relaxation frequencies lay in the same range. In the rod-like - bent-core mixtures, however, the characteristic frequencies of the relaxations originating from the various components are very different, thus the dielectric spectra of the mixtures can be interpreted as superpositions of the bent-core and calamitic relaxations.

Considering the pure 6OO8 ( $X = 1$ ), there were no relaxations detected in the measurement range in the isotropic phase and in the  $\perp$  component of the nematic phase, in contrast to CIPbis10BB, where one relaxation was found in each of those cases:  $BM_{iso1}$  and  $BM_{\perp1}$ , respectively. In the mixtures at lower concentrations of 6OO8, also one relaxation of each could be seen in the isotropic and in the perpendicular nematic cases:  $MM_{iso}$  and  $MM_{\perp1}$ , respectively (see Table 4.2). The dielectric increments of  $MM_{iso}$ , and of  $MM_{\perp1}$  decreases with the decreasing amount of CIPbis10BB in the mixtures (Fig. 4.10(a)), thus these relaxations are assumed to originate from the bent-core modes  $BM_{iso1}$  and  $BM_{\perp1}$ , respectively. As a first approximation, the dielectric increments exhibit a linear dependence with the molar fraction of the bent-core compound:  $\Delta\epsilon_{MM_{iso}} \propto (1 - X)$  and  $\Delta\epsilon_{MM_{\perp1}} \propto (1 - X)$  (see the dotted lines in Fig. 4.10(a)).

The relaxation frequencies  $f_{MMiso}$  and  $f_{MM\perp 1}$  increase linearly with the concentration using a logarithmic scale of  $f$  (Fig. 4.10(c), dotted lines), meaning  $\log f_{MMiso} \propto X$  and  $\log f_{MM\perp 1} \propto X$ . At higher concentrations of the rod-like compound,  $f_{MMiso}$  and  $f_{MM\perp 1}$  became too high to be directly detected in the used frequency range. The increase of the relaxation frequencies with the increasing molar fraction of the rod-like compound is in agreement with the exponential concentration dependence of the viscosity discussed above [91].

The parallel dielectric spectra in the nematic phase of 6OO8 show one relaxation in the measurement range:  $CM_{\parallel 1}$ . In the case of ClPbis10BB, two relaxations were found in the same range:  $BM_{\parallel 1}$  and  $BM_{\parallel 2}$ . In the mixtures also two relaxations were directly detected, namely  $MM_{\parallel 1}$  and  $MM_{\parallel 2}$ . The dielectric increment of  $BM_{\parallel 1}$  decreases linearly with the increasing concentration of the rod-like compound (see the dotted line in Fig. 4.10(a)), and it becomes undetectable at  $X > 0.8$ . Consequently  $MM_{\parallel 1}$  corresponds to the same process that accounts for the bent-core mode  $BM_{\parallel 1}$ , similarly to the cases of  $MM_{iso}$  and  $MM_{\perp 1}$ . The relaxation frequency  $f_{MM_{\parallel 1}}$  also increases exponentially with  $X$  (Fig. 4.10(a)), due to strong decrease of the viscosity with  $X$ . The symmetrical distribution parameter  $\alpha_{MM_{\parallel 1}}$ , however, is zero in the whole concentration range, meaning that the relaxation remains clearly Debye-type. Interestingly, the mode  $MM_{\parallel 1}$  becomes undetectable at around the same concentration range ( $X > 0.8$ ), where the presence of smectic clusters could not be observed in small angle X-ray studies using the binary system of ClPbis10BB and 6OO8 [90]. This coincidence might support that the lowest frequency relaxation originated from the bent-core compound is connected to the polar smectic clusters.

In contrast to the relaxations discussed so far,  $MM_{\parallel 2}$  exhibits different behavior as the function of  $X$ . In Fig. 4.8(b), the flattening of the loss peaks for  $MM_{\parallel 2}$  is spectacular at medium concentrations that is quantified by the fit results of  $\alpha_{MM_{\parallel 2}}$  showing a maximum at  $X = 0.5$ . The explanation of this effect can be given by considering two relaxations originating from 6OO8 and ClPbis10BB that gradually overlap, then merge at an intermediate concentration. Mathematically, the sum of two relaxations with close characteristic frequencies can be well approximated by one Cole-Cole type relaxation with an increased  $\alpha$  parameter. The obtained maximum in the symmetrical distribution parameter of  $MM_{\parallel 2}$  thus supports the assumption of the merging of relaxations. Obvi-

ously the broad relaxations around  $X = 0.5$  cannot be decomposed unambiguously to the constituent components.

According to the discussion above,  $MM_{\parallel 2}$  is most probably composed of two modes:  $MM_{\parallel 2a}$  and  $MM_{\parallel 2b}$ , originating from  $BM_{\parallel 2}$  and  $CM_{\parallel 1}$ , respectively. At low  $X$ ,  $MM_{\parallel 2a}$  dominates, while closer to the concentration of the pure 6OO8, mainly  $MM_{\parallel 2b}$  contributes in  $MM_{\parallel 2}$ , because the corresponding dielectric increments should vary proportionally with the concentrations of the relevant compounds:  $\Delta\varepsilon_{MM_{\parallel 2a}} \propto (1 - X)$  and  $\Delta\varepsilon_{MM_{\parallel 2b}} \propto X$  (see crossing dashed lines in Fig. 4.10(a)). The characteristic frequency of  $BM_{\parallel 2}$  is only slightly lower than  $f_{CM_{\parallel 1}}$ , and due to the decrease of the viscosity at higher  $X$ , both  $f_{MM_{\parallel 2a}}$  and  $f_{MM_{\parallel 2b}}$  are expected to be higher at concentrations closer to  $X = 1$ . For the  $X$  dependence of  $\alpha$  and that of the logarithmic relaxation frequencies, a linear extrapolation was performed using the values of the pure compounds and that of the closest mixtures: namely  $X = 0$  and  $X = 0.29$  for  $MM_{\parallel 2a}$  and  $X = 1$  and  $X = 0.92$  for  $MM_{\parallel 2b}$ . The extrapolation lines are illustrated as the dashed lines in Figs. 4.10(c) and 4.10(b).

The dielectric spectra of the mixtures could then be synthesized as a superposition using the extrapolated values for  $MM_{\parallel 2a}$  and  $MM_{\parallel 2b}$ , and the experimentally fitted parameters for  $MM_{\parallel 1}$  and the DC conductivity. The resulting synthesized loss spectra of the mixtures are presented in Fig. 4.8(c) that qualitatively show well all important features of the experimental spectra shown in Fig. 4.8(b). A quantitative agreement, however, could not be expected due to the roughness of the extrapolations. Furthermore, the contributions of the relaxations above the used frequency range were not possible to include into the superposition.

## 4.2 Studies of elasticity

### 4.2.1 Elasticity of a typical bent-core nematic compound

The effective dielectric constant  $\varepsilon_{eff}$  as the function of the applied magnetic inductance  $B$  for a planar cell filled with ClPbis10BB in the splay geometry is presented in Fig. 4.14.

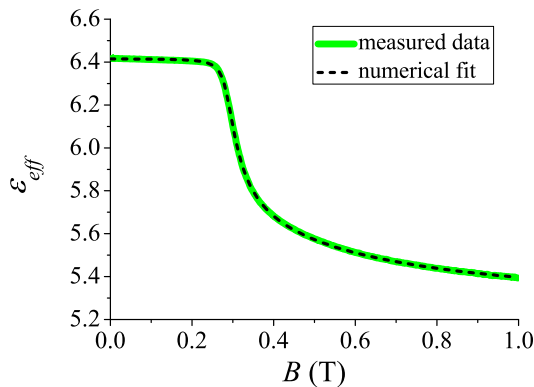


**Fig. 4.14:** The effective dielectric constant  $\varepsilon_{eff}$  as the function of the applied magnetic inductance  $B$  measured in the splay geometry on ClPbis10BB at  $\Delta T = -2$  °C (solid line). The dashed line is a fit using Eq. (3.9).

The experimental data recorded with high point density are plotted in Fig. 4.14 (solid line). The measurement was performed at  $\Delta T = -2$  °C using setup S1 [P2] (see Sec. 3.2.3). The main characteristics of the obtained curve are quite typical. At low applied fields,  $\varepsilon_{eff}$  is seemingly constant at the value of  $\varepsilon_{\perp} \approx 6.4$  with a good approximation. Then slightly below 0.3 T, where the field exceeds the splay Freedericksz threshold ( $B_{ts0}$ ), it starts to decrease sharply. The (negative) slope of  $\varepsilon_{eff}(B)$ , increases at higher fields, showing the expected saturation to  $\varepsilon_{\parallel}$  at very high  $B$ . The occurrence of the Freedericksz-transition in the splay geometry supports the initial assumption of  $\chi_a > 0$ . Moreover the important information about the negative sign of the dielectric anisotropy  $\varepsilon_a$  is also indicated immediately by the negative slope of the measured curve above the threshold field.

The dashed line in Fig. 4.14 shows the numerical fit of the measurement data using the fit method described in Sec. 3.2.1. Seemingly the fit is very good, serving the four fit parameters:  $B_{ts0} = 0.3$  T,  $\kappa = -0.72$ ,  $\Theta_0 = 3.4^\circ$ , and  $\varepsilon_{\parallel} = 5.2$ .

The transmitted normalized optical intensity versus  $B$ , measured simultaneously with the dielectric data shown above, is presented in Fig. 4.15(a).

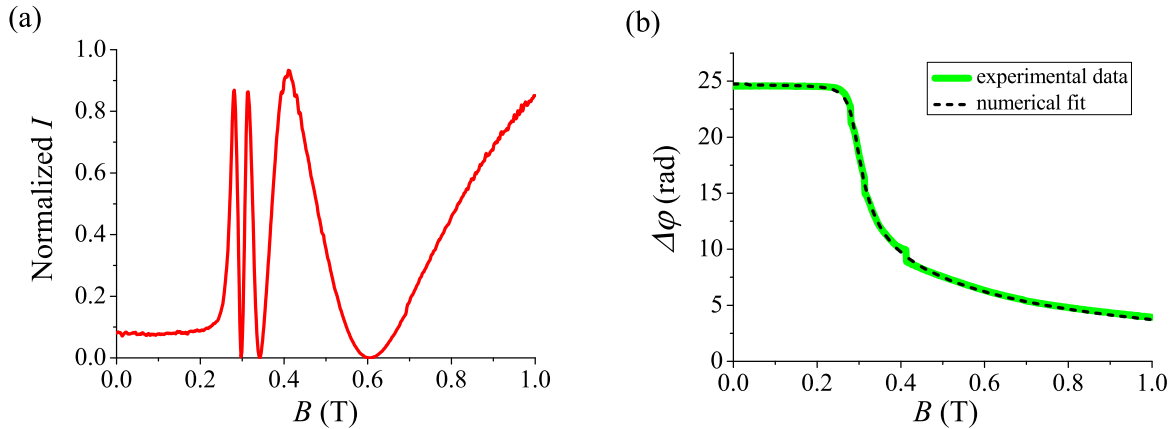


**Fig. 4.15:** (a) The normalized light intensity transmitted through the sample of CIPbis10BB between crossed polarizers as the function of the applied magnetic inductance  $B$  measured in the splay geometry at  $\Delta T = -2$  °C. (b) The phase difference  $\Delta\varphi$  between the ordinary and extraordinary components of the transmitted light as the function of  $B$  calculated from the intensity data using Eq. (1.32) (solid line). The dashed line is a fit using Eq. (3.12).

It can be seen in Fig. 4.15(a) that the intensity oscillates above the Freedericksz-threshold, as expected. The magnetic field dependence of the optical phase difference ( $\Delta\varphi(B)$ ) calculated from the intensity data is presented in Fig. 4.15(b) as the solid line. The resulting curve of  $\Delta\varphi(B)$  is qualitatively very usual. Below the threshold field, the phase difference is constant and equals to  $\Delta\varphi_0 = \frac{2\pi}{\lambda} dn_a$  (defined in Sec. 1.2.6 as Eq. (1.28)). Above  $B_{ts0}$ , it starts to decrease sharply, then it saturates to 0 at higher fields. One might notice small jumps at the magnetic field values, where the extrema of the intensity curve are. Those are the consequence of that the measured intensity extrema are not at the same level in the case of the different applied magnetic fields.

The numerical fit of  $\Delta\varphi(B)$  is shown as the dashed line in Fig. 4.15(b). The quality of the fit here is also very good. The obtained fit parameters are:  $B_{ts0} = 0.3$  T,  $\kappa = -0.72$ ,  $n_e = 1.64$ , and  $n_o = 1.55$ . The fit values for  $B_{ts0}$  and  $\kappa$  were similar to those obtained independently in the dielectric case, showing the reliability of the fitting methods.

In order to obtain the actual values of  $K_{11}$  and  $K_{33}$ , the magnetic field threshold as the function of constantly applied ( $f = 1$  kHz, sinusoidal) voltages ( $B_{ts}(U_{ts})$ ) had to be determined. The result is plotted in Fig. 4.16.

The experimental data are fitted by Eq. (3.15) (solid line in Fig. 4.16), with the only fit parameter  $U_{ts0}$ . With the resulting  $U_{ts0} = 1.7$  V,  $K_{11} = 3.1$  pN could be determined using

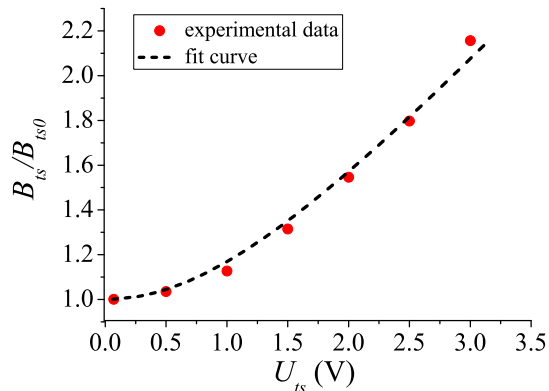


**Fig. 4.16:** The relative magnetic inductance threshold  $B_{ts}/B_{ts0}$  as the function of the applied voltage  $U_{ts}$  measured in the splay Fredericksz-transition geometry on ClPbis10BB at  $\Delta T = -2$  °C (symbols). The solid line is a fit using Eq. (3.15).

the known value of  $\varepsilon_a$ . Combining  $K_{11}$ ,  $\kappa$ ,  $B_{ts0}$  yielded additional material parameters:  $K_{33} = 0.88$  pN and  $\chi_a = 5.5 \times 10^{-7}$ .

The result of the optical depolarization measurement in the twist geometry (see Sec. 3.2.2) is presented in Fig. 4.17, where the transmitted intensity is plotted as the function of the applied magnetic field. It is clearly visible that the transmitted intensity

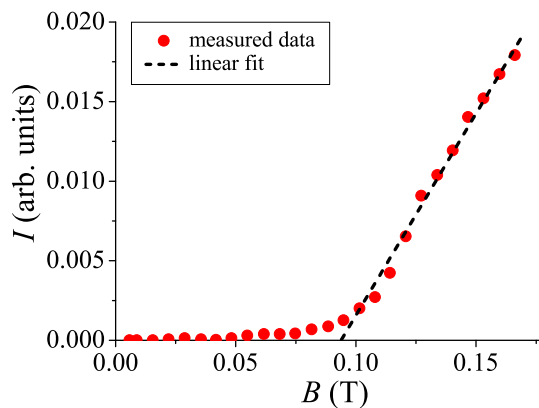


**Fig. 4.17:** The light intensity transmitted through the sample of ClPbis10BB between crossed polarizers as the function of the applied magnetic inductance  $B$  measured in the twist geometry at  $\Delta T = -2$  °C (symbols). The dashed line shows the determination of the twist Fredericksz-threshold  $B_{tt0}$  by linear extrapolation.

is zero at low fields until  $B = B_{tt0}$ , where it starts to increase due to the small depolarization. The twist Fredericksz-threshold was determined from linear extrapolation, giving the value of  $B_{tt0} = 0.094$  T that combining with  $\chi_a$  yields  $K_{22} = 0.31$  pN. All

obtained material parameters for ClPbis10BB are collected in Table 4.4, shown later in Sec. 4.2.5.

### 4.2.2 Simulations of the twist geometry

The basis of the present studies that aimed to reach a better understanding of the twist Fredericksz-measurements is the calculation of the director field including the effect of pretilt [P3]. The solution of the system of differential equations introduced in Sec. 3.2.2 is presented in Fig. 4.18, where the director field is visualized by the twist and tilt angles as the function of the cross section direction of the cell ( $\phi(z)$  and  $\Theta(z)$ , respectively). The simulations were performed using several values of  $B$  counted in units of  $B_{tt0}$ . The

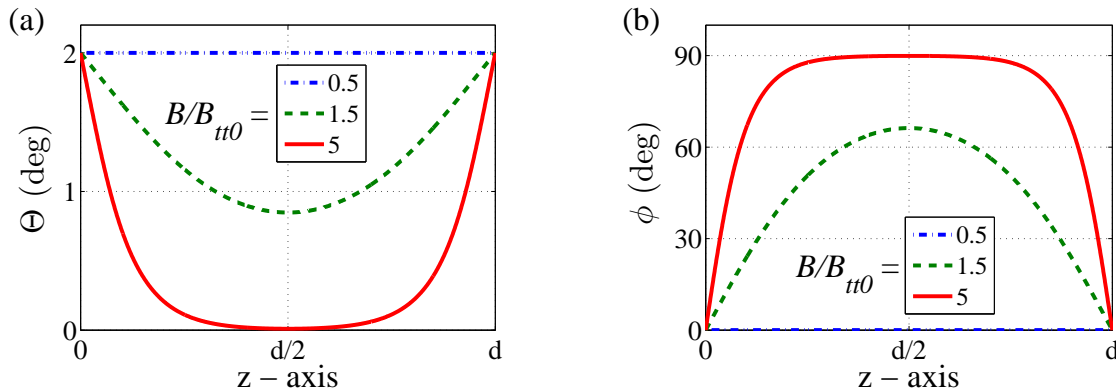


**Fig. 4.18:** The simulated variation of (a) the director tilt  $\Theta$  and of (b) the director twist  $\phi$  along the  $z$ -direction of the cell at different applied magnetic inductances in the twist Fredericksz-transition with  $\Theta_0 = 2^\circ$  pretilt.

material parameters of a standard rod-like compound 5CB [P2] were used, with the pretilt of  $\Theta_0 = 2^\circ$ . The dash-dotted lines show the case of the magnetic field below the threshold ( $B/B_{tt0} = 0.5$ ), where there is no deformation, thus both the twist and tilt angles remain unaffected everywhere inside the cell:  $\phi = 0^\circ$  and  $\Theta = \Theta_0$ . Above the threshold at  $B/B_{tt0} = 1.5$ , the director is reoriented with the largest deformation in the middle of the cell, according to the condition of the strong anchoring at the cell boundaries (dashed lines). The effect of the magnetic field results in the increase of the twist angle  $\phi$ , and the slighter decrease of the tilt angle  $\Theta$ . Much above the threshold ( $B/B_{tt0} = 5$ ), the director is parallel with the magnetic field in the most part of the cell; thus  $\phi \approx 90^\circ$  and  $\Theta \approx 0^\circ$ , except in the vicinity of the substrates.

Using the ability to calculate the director profiles for different applied magnetic fields, the next step is to derive experimentally accessible quantities as the function of  $B$ . First, the effective dielectric constant is calculated versus the magnetic field applying Eq. (3.8). The effect of a small misalignment of  $\mathbf{B}$  was also studied in order to model experimental imperfections. For the sake of this,  $\beta$  is defined as the angle between  $\mathbf{B}$  and the  $y$ -direction in the  $yz$ -plane, thus  $\tan \beta = B_z/B_y$  and  $B_x = 0$  (see Fig. 3.5). In Fig. 4.19, the reduced effective dielectric constant  $(\varepsilon_{eff} - \varepsilon_{\perp})/\varepsilon_a$  is shown as the function of  $B/B_{tt0}$  for two examples. The solid line in Fig. 4.19 shows the perfectly adjusted geometry with pretilt ( $\Theta_0 = 2^\circ$ ,  $\beta = 0^\circ$ ) and the dashed line presents the case of the misaligned magnetic field with no pretilt ( $\Theta_0 = 0^\circ$ ,  $\beta = 2^\circ$ ). A transition could be observed in both

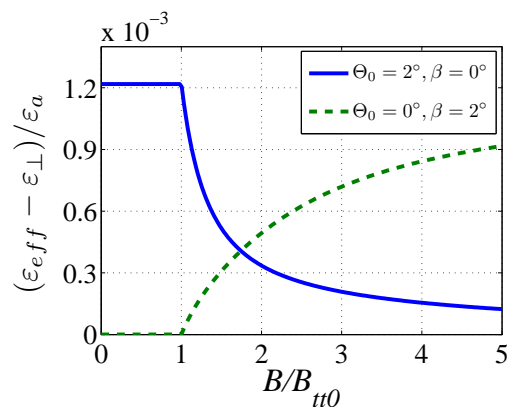


**Fig. 4.19:** The calculated reduced dielectric constant as the function of relative magnetic inductance during the twist magnetic Fredericksz-transition. Solid line: untilted field and director pretilt of  $\Theta_0 = 2^\circ$ ; dashed line: tilted field and no director pretilt.

cases by a small change in the effective dielectric constant. It is important to realize that in a perfectly aligned twist geometry with zero pretilt ( $\Theta_0 = 0^\circ$ ,  $\beta = 0^\circ$ ), the transition would not be detectable dielectrically, because the tilt angle with respect to the cell plane would not change during the reorientation of the director.

In the case of  $\Theta_0 \neq 0$  (Fig. 4.19 solid line), the Fredericksz-transition can be observed with sharp threshold characteristics. The sharpness is due to the fact that the initial director is perpendicular to the magnetic field even in the presence of a nonzero pretilt, in contrast to the splay geometry, where the pretilt makes the threshold smoother. The dielectric detection of the twist Fredericksz-transition offers a novel measurement technique to determine  $K_{22}$  that could be widely applied, since a well defined pretilt is

always present due to the rubbed polyimide alignment layers of a planar cell. In Fig. 4.19, the apparent threshold on the simulated curves is basically identical with  $B_{tt0}$ , which can be expected for the cases of small  $\Theta_0$ . With no applied  $B$ , the effective dielectric constant is  $\varepsilon_{eff} = \varepsilon_{\perp} + \varepsilon_a \sin^2 \Theta_0$ . At high fields, it converges to  $\varepsilon_{\perp}$ , thus the maximum change of  $\varepsilon_{eff}$  is in the order of 0.1 % of  $\varepsilon_a$  for usual  $\Theta_0$ . This is a small value, especially for mesogens with low dielectric anisotropy, however, a good impedance analyzer has a resolution in the order of parts per million (or better), thus the realization of such experiments is possible.

In the case of  $\Theta_0 = 0$  and  $\beta \neq 0$  (Fig. 4.19 dashed line), the transition can also be detected dielectrically due to the change of the tilt angle  $\Theta$ , since the misaligned magnetic field has a small component  $B_z$  that is not parallel with the substrates. Nevertheless, here  $\mathbf{B}$  is also perpendicular to the initial director, thus a sharp transition can be seen. An important difference is, however, that the relative change of  $\varepsilon_{eff}$  is of opposite sign compared to the case with the nonzero pretilt discussed above. More generally, where both  $\Theta_0 \neq 0$  and  $\beta \neq 0$ , the two effects work against each other thus reducing the change in  $\varepsilon_{eff}$ . Moreover the observable transition is expected to appear less sharp, since the magnetic field would be then not perpendicular to the initial director. Consequently, the misalignment of the magnetic field in an experiment should be reduced as much as possible in order to obtain usable data. This can be achieved by positioning the sample holder with appropriate mechanical constraints with respect to the poles of the magnet.

The precise knowledge of the director field allows to study the optical characteristics of the cell as well. The Mauguin-condition for the adiabatic light propagation (see Sec. 1.2.6) in a continuously twist deformed director field in cholesterics is given by:  $\lambda \ll P n_a$ , where  $P$  is the cholesteric pitch [2]. In order to apply this to our twist geometry for the sake of some qualitative analysis, the Mauguin-condition is expressed in terms of the twist angle gradient ( $\phi'$ ):  $\lambda \ll \frac{2\pi}{\phi'} n_a$ . The dimensionless quantity  $\eta$  is introduced in order to measure how well the Mauguin-condition is satisfied:  $\eta = \frac{2\pi}{\lambda \phi'_{max}} n_a$ . As a conservative estimate,  $\phi'$  was replaced by its maximum ( $\phi'_{max}$ ) in the cell, since in contrast to the cholesterics,  $\phi'$  is not constant in a deformed sample in the twist geometry. The decrease of  $\eta$  indicates that the condition for the adiabatic light propagation is less satisfied, therefore a larger transmittance is expected. Although this effect increases continuously with the stronger twist deformation, in order to analyze qualita-

tively the influence of  $B$ ,  $\Theta_0$ , and the thickness  $d$ , an arbitrary large number ( $\eta_c = 20$ ) of  $\eta$  was selected as a discriminating value. Consequently  $\eta > \eta_c$  corresponds to the regime, where the light can perfectly follow the changes in the director, thus no transmittance is expected in the twist geometry.

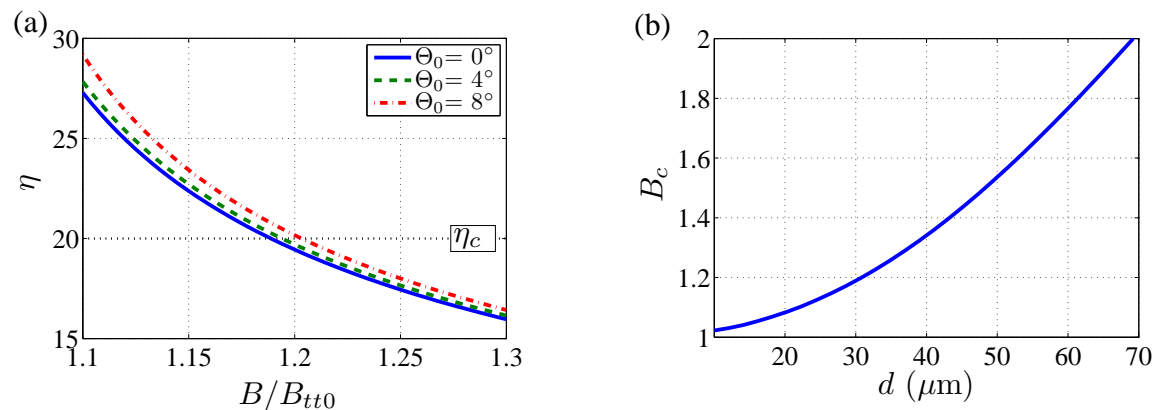


**Fig. 4.20:** (a) The parameter  $\eta$ , that indicates how well the Mauguin-condition is satisfied in the twist Fredericksz-transition, is plotted as the function of the relative magnetic inductance  $B/B_{tt0}$  for three pretilt values with the cell thickness  $d = 30 \mu\text{m}$ . (b) The thickness dependence of the critical relative magnetic inductance  $B_c$ .

The magnetic field dependence of  $\eta$  is presented in Fig. 4.20(a) calculated for a  $d = 30 \mu\text{m}$  thick cell with different pretilt angles. The monotonic decrease of  $\eta(B/B_{tt0})$  indicates that the depolarization of the transmitted light increases at higher relative magnetic field; this is due to larger gradients of  $\phi$  in the vicinity of the substrates as could be seen in Fig. 4.18(a).

The critical (relative) magnetic inductance  $B_c$  is formally introduced as  $\eta(B_c) = \eta_c$ . At the relative magnetic fields larger than  $B_c$  ( $B/B_{tt0} > B_c$ ), the twist Fredericksz-transition is considered to be detectable by the depolarization measurements. Below  $B_c$ , however, the light propagation is in the adiabatic regime, thus the optical transmittance is expected to be too small to detect the transition. It can be seen in Fig. 4.20(a) that the curves of  $\eta(B/B_{tt0})$  and thus  $B_c$  shifts towards higher values of the relative magnetic fields if larger pretilts are present, because the pretilt has a reducing effect on the gradient of the twist angle.

The thickness dependence of  $B_c$  is presented in Fig. 4.20(b). It can be seen that  $B_c$  significantly increases with  $d$ , indicating that the usage of a thinner cell is suggested for the more precise determination of the twist Fredericksz-threshold by depolarization

measurements. It should be emphasized, however, that the concept of  $\eta_c$  and  $B_c$  was created only for a qualitative analysis to reveal the tendencies of how the characteristics of the adiabatic light propagation depend on some relevant parameters such as the thickness, magnetic field and pretilt. It is also important to note that the analysis above could be performed using exclusively the calculations of the director field inside the cell.

The optical transmittance versus  $B$  was calculated using the Mueller-matrix method (see Sec. 1.2.6 and Sec. 3.2.2) in the case of the twist geometry for several values of the cell thickness  $d$  without pretilt. The results can be seen in Fig. 4.21(a). The optical

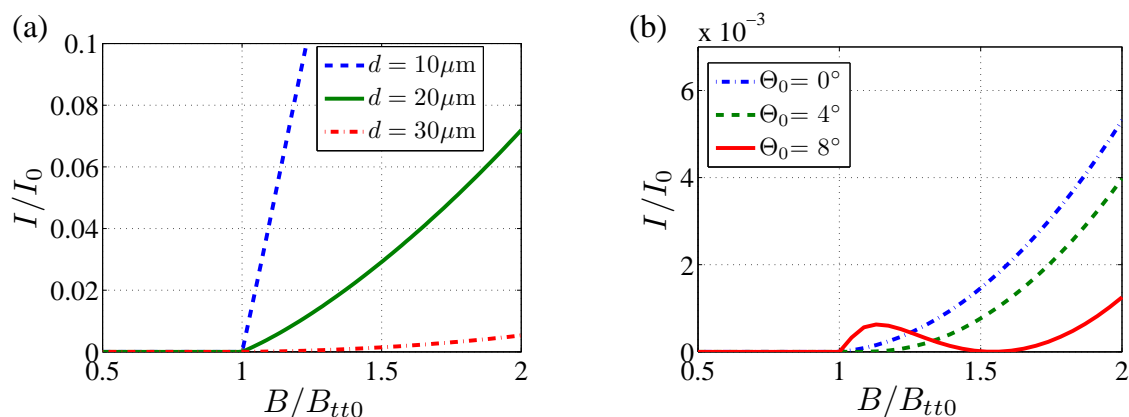


**Fig. 4.21:** The magnetic inductance dependence of the calculated optical transmittance for: (a) three different cell thickness with no pretilt; (b) three distinct pretilt ( $\Theta_0$ ) values at the thickness  $d = 30 \mu\text{m}$  in the twist Freedericksz-transition geometry.

calculations confirmed the tendencies predicted by the qualitative analysis discussed above, namely the transmittance signal at  $B > B_{tt0}$  is much higher for thinner cells in the twist geometry. In conclusion, the adiabatic light propagation induced problems of the optical threshold detection in the twist geometry can be overwhelmed by using relatively thin cells. The disadvantage of the small thickness, however, is the increased Freedericksz-threshold, since  $B_{tt0} \propto d^{-1}$ . For example in the case of a  $10 \mu\text{m}$  thick planar cell filled with 5CB, the threshold is  $B_{tt0} = 0.6 \text{ T}$  that can be achieved by common laboratory electromagnets. Nevertheless, higher thickness values are more favorable for the measurements in the splay geometry, because in that case, it is important to have the experimental data obtained in the high field regime ( $B \gg B_{ts0}$ ). In practise, in order to reduce material consumption, the usage of a single planar cell is preferred that can be used in both geometries, requiring a compromise in selecting the cell thickness.

The effect of the pretilt on the optical behavior of a planar cell was also studied in the twist geometry. It was shown above that considering a nonzero pretilt, besides the change of the twist angle, additionally the tilt angle also varies. Consequently, the resulting optical transmittance during the Fredericksz-transition is affected by not only the depolarization, but the birefringence-effect as well. In the case of three different pretilt values, the transmittance was calculated as the function of  $B$  using  $d = 30 \mu\text{m}$ . The results are shown in Fig. 4.21(b). Increasing the pretilt to  $4^\circ$  (dashed line), the transmittance curve is still monotonic and it is shifted towards higher magnetic fields. At an even higher value of the pretilt ( $\Theta_0 = 8^\circ$ , solid line in Fig. 4.21(b)), the transmittance versus  $B$  is not monotonic, a hump that is attributed to the effect of birefringence appears above the threshold. Oscillations in the transmitted intensity can be observed at higher pretilt and/or thickness, and their characteristics depend strongly on the parameters of the cell (e.g. thickness, material constants). In order to avoid the more difficult analysis of the measurements giving such data, the application of thin cells should be preferred.

### 4.2.3 The case of an unconventional bent-core compound

The effective dielectric constant  $\varepsilon_{eff}$  as the function of the applied magnetic inductance  $B$  was measured on DT6PY6E6 in the splay geometry using setup S1 [P3]. The result recorded at  $\Delta T = -24 \text{ }^\circ\text{C}$  can be seen in Fig. 4.22(a) (solid line) that is apparently similar to the case of ClPbis10BB (see Fig. 4.14), except that here  $\varepsilon_{eff}$  increases above the Fredericksz-threshold from  $\varepsilon_\perp \approx 4.1$  due to the positive dielectric anisotropy. The quality of the numerical fit (dashed line) on the experiment here is also very good. The fit parameters were obtained as:  $B_{ts0} = 0.35 \text{ T}$ ,  $\kappa = 0.93$ ,  $\varepsilon_\parallel = 5.9$ , and  $\Theta_0 = 2.8^\circ$ .

Due to the positive dielectric anisotropy of DT6PY6E6 ( $\varepsilon_a = +1.84$  at  $\Delta T = -24 \text{ }^\circ\text{C}$ ), the electric Fredericksz-transition could be observed optically in the splay geometry. After the measurement of the transmitted intensity as the function of the applied voltage ( $U$ ), the  $U$ -dependence of the optical phase difference ( $\Delta\varphi(U)$ ) was determined and fitted, as it can be seen in Fig. 4.22(b) (solid and dashed lines, respectively). The numerical fit based on the calculations presented in Sec. 3.2.1, here also nicely matches the experimental data. Providing the input parameters of  $\varepsilon_\parallel$ ,  $\varepsilon_\perp$ ,  $\kappa$ ,  $d$ ,  $\lambda$ , and  $n_a$  (this latter was determined from the maximal phase difference  $\Delta\varphi_0$ , see Eq. (1.28)), the fit

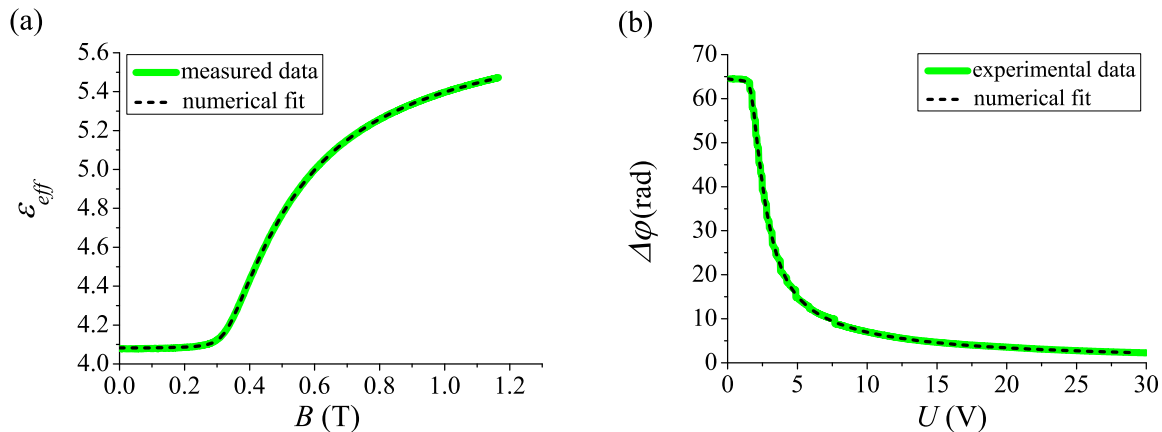


**Fig. 4.22:** (a) The effective dielectric constant  $\epsilon_{eff}$  as the function of the applied magnetic inductance  $B$  measured in the splay geometry on DT6PY6E6 at  $\Delta T = -24$  °C (solid line). The dashed line is a fit using Eq. (3.9). (b) The phase difference  $\Delta\phi$  between the ordinary and extraordinary components of the transmitted light as the function of the applied voltage  $U$  calculated from the intensity data using Eq. (1.32) (solid line). The dashed line is a fit using Eq. (3.14).

resulted in  $U_{ts0} = 1.8$  V (rms) and  $n_o = 1.54$ . The following material parameters could then be calculated:  $K_{11} = 5.4$  pN,  $K_{33} = 10$  pN,  $\chi_a = 7.4 \times 10^{-7}$ ,  $n_a = 0.24$ .

The usability of the new dielectric technique to determine  $K_{22}$  in the twist geometry was first demonstrated on the bent-core compound DT6PY6E6 using setup S1 [P3]. Later the same method was applied on the well-known compound 5CB using setup S2 in order to confirm its precision by comparing the results of  $K_{22}$  with the literature data. The effective dielectric constant as the function of the magnetic inductance is plotted for DT6PY6E6 and 5CB in Fig. 4.23(a) and (b), respectively. In the case of DT6PY6E6, the result of the intensity measurements is also shown.

The experimental data clearly show that the measurement based on the novel principle could be carried out in practice. The magnetic field thresholds of the twist Fredericksz-transition can be observed dielectrically, thus this new method can be used to determine the twist elastic constant  $K_{22}$ . In both cases,  $\epsilon_{eff}$  decreases above the threshold, showing that the effect originates mainly from the presence of pretilt, and not from the misalignment of the magnetic inductance (see Fig. 4.19). In Fig. 4.23(a), the optical intensity is noisier than the dielectric data in spite of that the relative change in  $\epsilon_{eff}$  is in the order of  $10^{-3}$  only. Moreover, the intensity data show the threshold less unambiguously compared to the curve of  $\epsilon_{eff}(B)$ . Nevertheless, the noise free dielectric

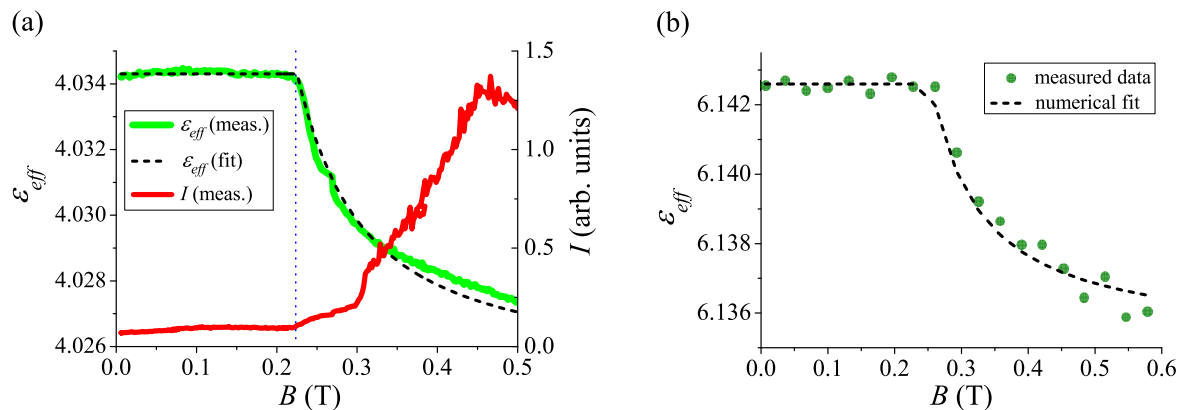


**Fig. 4.23:** (a) The magnetic inductance ( $B$ ) dependence of the effective dielectric constant  $\varepsilon_{eff}$  (measured data: green solid line, fit: dashed line) and of the transmitted intensity (red solid line) measured on DT6PY6E6 in the twist geometry at  $\Delta T = -24$  °C. (b)  $\varepsilon_{eff}$  as the function of  $B$  measured on 5CB at  $\Delta T = -8$  °C in the twist Freedericksz-transition geometry using setup S2. The symbols are experimental data points; the dashed line is a numerical fit.

data could be achieved by a state-of-the-art impedance analyzer. In the case of 5CB,  $\varepsilon_{eff}$  suffers by a much higher level of noise, since in setup S2 the dielectric constant was measured by an ordinary oscilloscope.

The numerical fits of the dielectric data are shown by the solid lines. In the case of the bent-core compound, the previously determined material parameters were used in the fit. For 5CB, the necessary values were taken from the literature ( $K_{11} = 5.9$  pN and  $K_{33} = 8.9$  pN [80],  $\varepsilon_{||} = 17.5$  [93] and  $\chi_a = 1.2 \cdot 10^{-6}$  [94]).

In the case of DT6PY6E6 and 5CB, the fitted values of the twist Freedericksz-threshold are  $B_{tt0} = 0.23$  T and  $B_{tt0} = 0.25$  T that yield  $K_{22} = 2.2$  pN and  $K_{22} = 4.2$  pN, respectively. The literature value of the twist elastic constant for 5CB is  $K_{22} = 3.9$  pN [80] that deviates less than 10 % from the parameter obtained by the novel method under scope.

#### 4.2.4 Characterization of a rod-like compound

The material parameters of the rod-like nematic liquid crystal 10O8 was measured as the function of temperature [P7]. Due to the negative dielectric anisotropy, the methods used were completely similar to those applied in the case of ClPbis10BB (see Sec. 4.2.1). The measurement procedure was repeated in each temperature using setup S2 with only a single planar cell. Here the final results are presented that will be used later in Sec. 4.3.

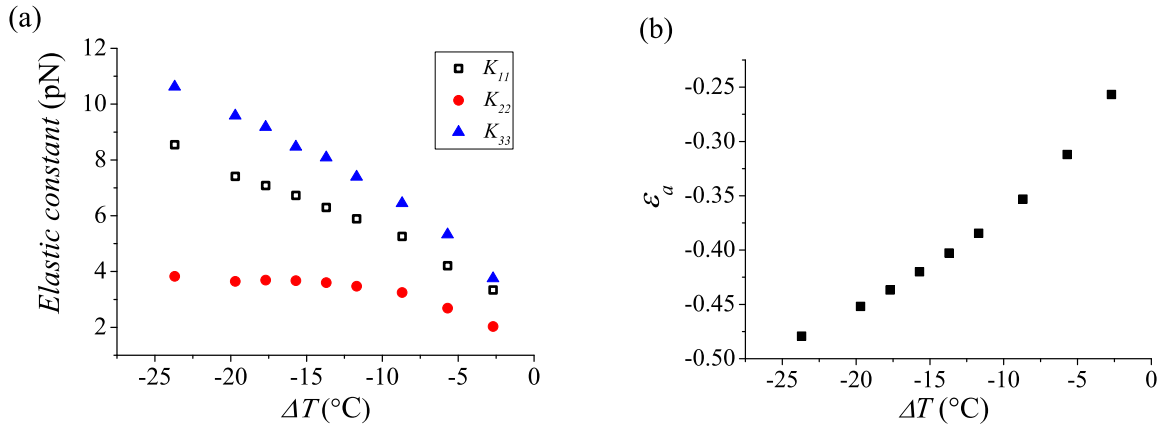


**Fig. 4.24:** (a) The elastic constants and (b) the dielectric anisotropy of 10O8 as the function of temperature.

The three elastic constants of 10O8 are plotted as the function of  $\Delta T$  in Fig. 4.24(a). Fig. 4.24(b) presents the temperature dependence of  $\epsilon_a$ . The measured values of the elastic constants and their temperature dependences are typical for rod-like nematic liquid crystals. The most special property of 10O8, however, is the low magnitude of the dielectric anisotropy that allowed the appearance of flexodomains in this compound.

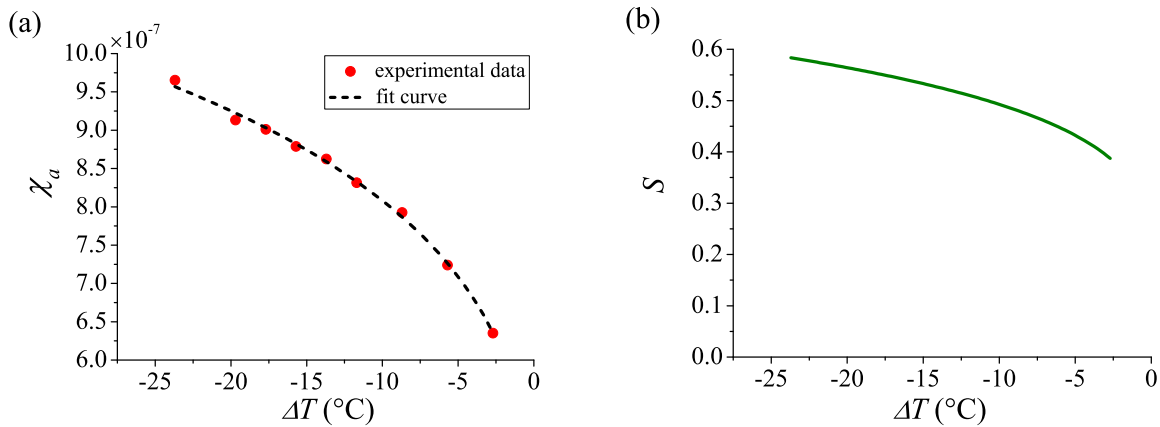


**Fig. 4.25:** (a) The diamagnetic susceptibility anisotropy (symbols: experimental data, dashed line: fit) and (b) the order parameter of the compound 10O8 as the function of temperature.

The temperature dependence of  $\chi_a$  is presented in Fig. 4.25(a). The diamagnetic susceptibility anisotropy is one of the few bulk parameters, which is directly coupled to the nematic scalar order parameter:

$$\chi_a(T) = \hat{\chi}S(T), \quad (4.1)$$

where  $\hat{\chi}$  is a constant. The order parameter can well be approximated (except in the vicinity of  $T_{NI}$ ) by the empirical Haller-formula [11, 95]:

$$S(T) = \left(1 - \beta_H \frac{T}{T_{NI}}\right)^\gamma, \quad (4.2)$$

where  $\beta_H$ ,  $\gamma$  are constants, and the temperature data ( $T$ ,  $T_{NI}$ ) is measured in the Kelvin-scale. Combining Eq. (4.1) and Eq. (4.2) gives the opportunity to fit the experimental data of  $\chi_a(T)$  and determine  $S(T)$ . The resulting fit curve can be seen in Fig. 4.25(a) (solid line). The best fit could be obtained by the fit parameters:  $\hat{\chi} = 1.64 \times 10^{-6}$ ,  $\beta_H = 1$ , and  $\gamma = 0.2$  that fall in the range of earlier results [11] obtained for different compounds with two aromatic rings. The actual values of the order parameter as the function of  $\Delta T$  are presented in Fig. 4.25(b).

#### 4.2.5 Discussion

The important material parameters of the studied compounds are summarized in Table 4.4.

	CIPbis10BB <sup>†</sup>	DT6PY6E6 <sup>†</sup>	1O08 <sup>‡</sup>	5CB <sup>†</sup>	5CB <sup>*</sup>
$\Delta T$ (°C)	-2	-24	-23.7	-10	-10
$K_{11}$ (pN)	3.1	5.4	8.5	5.9	6
$K_{22}$ (pN)	0.3	2.4	3.8	3.7(4.2 <sup>‡</sup> )	3.9
$K_{33}$ (pN)	0.9	10	10.6	8.7	8.3
$\varepsilon_a$	-1.2	+1.8	-0.48	+11.3	+11.2
$n_a$	0.09	0.24	0.13	0.18	0.18
$\chi_a$	$5.5 \times 10^{-7}$	$7.4 \times 10^{-7}$	$9.7 \times 10^{-7}$	$14 \times 10^{-7}$	$13 \times 10^{-7}$

**Table 4.4:** The important material parameters of the studied compounds measured by setup S1 (marked by <sup>†</sup>), and setup S2 (marked by <sup>‡</sup>). The literature data (marked by <sup>\*</sup>) of  $K_{11}$ ,  $K_{33}$ ,  $n_a$  [96],  $K_{22}$  [80],  $\varepsilon_a$  [93], and  $\chi_a$  [94] for 5CB. The twist elastic constant measured on setup S2 at a different temperature ( $\Delta T = -8$  °C) is marked by <sup>‡</sup>.

The representative bent-core compound CIPbis10BB qualitatively behaved similarly to the regular rod-like nematic mesogens in the experiments of Fredericksz-transitions [P2]. The measurement data of CIPbis10BB could be fitted perfectly using the classical continuum description of nematics, the experimental curves of dielectric constant and the optical parameters seemed to be quite normal for the first glance. The detailed evaluation of the data, however, showed that the extraordinary properties of CIPbis10BB lie in the

unusual values of its material constants. In Table 4.4, the important parameters of ClPbis10BB are presented next to the typical values for calamitics (10O8, 5CB). The splay elastic constant  $K_{11}$  is only slightly lower than that of the rod-like compounds, but severely different values were found for  $K_{22}$  and  $K_{33}$ . The twist and bend elastic constants are approximately one order of magnitude lower than in the case of regular calamitic nematics. Moreover, the ratio of  $K_{33}/K_{11}$  is reversed compared to ordinary nematics, where that is predominantly larger than one.

The reduction of  $K_{33}$  compared to  $K_{11}$  for bent-shaped molecules was discussed in the frame of a molecular statistical model by Helfrich [97]. The bend elastic constant decreases due to the bent molecular shape as:

$$K_{33} = \frac{\bar{K}_{33}}{1 + \hat{\beta}^2 \bar{K}_{33} / (\sqrt[3]{N} 2k_B T)}, \quad (4.3)$$

where  $\bar{K}_{33}$  is the non-decreased bend elastic constant that corresponds to the rod-like molecules;  $\hat{\beta}$  is the molecular bend angle that is zero for calamitics, and  $N$  is the number density of molecules. Assuming  $\hat{\beta} = 1 \text{ rad} \approx 57^\circ$ ,  $N = 10^{27} \text{ m}^{-3}$ ,  $T = 350 \text{ K}$  and  $\bar{K}_{33} = 10 \text{ pN}$ , Eq. (4.3) yields  $K_{33} \approx \bar{K}_{33}/2$ , thus the model of Helfrich could explain only a small part of the decrease in the bend elastic constant that is far from a complete explanation of the very low value measured for ClPbis10BB. Moreover, this theory does not account for the decrease of  $K_{22}$  at all; therefore it is not able to help understanding the unusually low  $K_{22}$  of ClPbis10BB.

Since the extraordinary elasticity of ClPbis10BB cannot be explained by the classical molecular statistical theory, the nematic phase of this bent-core compound might be more significantly different than that of calamitics. A structural difference can exist only on a mesoscopic level, because the bulk symmetries observed on a microscopic scale are identical to that of rod-like nematics. The concept of smectic clusters was discussed previously in Sec. 2.1 and in Sec. 4.1.5. Some extraordinary properties of bent-core nematics were explained by the presence of these nano-structures for a number of phenomena, including giant flexoelectricity, flow birefringence, NMR-studies, etc. Small angle X-ray studies [66, 88, 89, 90] served the first direct evidence for the existence of short-range molecular correlations with the symmetries of tilted smectics, identified as the clusters in ClPbis10BB and in other bent-core nematic liquid crystals. The evaluation

of the temperature independent correlation lengths showed that the size of these objects is about a few times of the molecular length. It was mentioned in Sec. 1.1.2 that achiral bent-core molecules can form polar phases [4]. This could be achieved so that the bulk liquid crystal consists of chiral domains with opposite handedness [5, 6]. The tilted smectic symmetry of the clusters allows to assume that these local structures are chiral and ferro- or antiferroelectric. The dilute dispersion of them with the equal probabilities of right and left handedness would also let the bulk nematic symmetries to prevail. The easier twisting and bending of the nematic director then could be explained by that the structure of the polar clusters involves molecular twists and bends similarly to the ferro- or antiferroelectric bulk phases [98]. In such way the low values of  $K_{22}$  and of  $K_{33}$  measured in the case of ClPbis10BB can be understood.

In contrast to ClPbis10BB, the elastic constants of DT6PY6E6 are rather similar to those of rod-like nematics [P3] (see Table 4.4). The features of the anomalous elasticity indicated for several bent-core nematic compounds by independent research groups [P2] [75, 99, 100] were not shown by DT6PY6E6. The ratio of  $K_{33}/K_{11}$  is larger than 1, the actual values of  $K_{33}$  and  $K_{11}$  are very close to that of 10O8 or 5CB. Although the twist elastic constant is relatively low, but still it is almost one order of magnitude larger than the  $K_{22}$  of ClPbis10BB.

The non-bent-core behavior of DT6PY6E6 is attributed to the presence of the four alkyl chains connected to the intermediate core rings (see Fig. 3.8). The hydrocarbon chains with single bonds are not rigid; they can easily change their shape because the  $\sigma$ -bonds allow rotations, thus many conformers are available with a small energy difference. Due to the steric repulsion, these alkyl chains obstruct the rigid bent-shaped cores of the molecules to interact. Consequently, without the tight molecular packing, the formation of the short-range correlations associated with the polar smectic clusters is not likely; thus the bent-core characteristics cannot arise. Small angle X-ray scattering studies on DT6PY6E6 [81] also support this idea, since the distance between the bent-shaped cores of the molecules was found to be unusually large; that could prohibit the appearance of the bent-core properties such as the anomalous elasticity, due to the lack of the polar smectic clusters.

## 4.3 Pattern formation at low frequencies

### 4.3.1 The transition to the low frequency regime

The threshold characteristics of the conductive electroconvection in the case of Phase 5 was studied [P5, P6] in the unexplored low-frequency regime, where the director relaxation time is expected to be smaller than the period of the sinusoidal AC driving voltage defined as  $\tilde{U}(t) = \sqrt{2}U \sin(2\pi ft)$  ( $\tau_d < \tau = 1/f$ , see Sec. 1.2.7 and Sec. 2.2).

The threshold voltage of the electroconvection ( $U_{cEC}$ ) was determined in a wide frequency range (10 mHz - 250 Hz) in order to see how the behavior changes from the well known high-frequency regime towards ultra-low frequencies. In Fig. 4.26, the  $U_{cEC}$  can be seen as the function of  $f$  on a logarithmic scale.

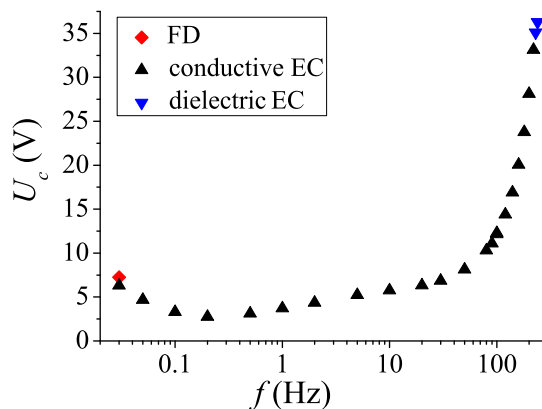


**Fig. 4.26:** The threshold voltage of electroconvection (EC) and flexodomains (FD) as the function of frequency.

The characteristics of electroconvection (EC) at higher frequencies are quite typical. At the highest frequencies in the studied  $f$ -range, the dielectric mode of the standard electroconvection could be observed as dielectric rolls that are perpendicular to the rubbing direction of the planar cell. Below the crossover frequency  $f_c \approx 230$  Hz, the threshold of the conductive mode is lower, thus the conductive electroconvection appears as normal rolls that are also perpendicular to the initial director, but with a much larger periodicity compared to dielectric rolls. Below the Lifshitz-frequency  $f_{Lif} \sim 150$  Hz, the roll direction becomes gradually tilted from the normal direction, thus a zig-zag structure, known as oblique rolls can be seen. The typical snapshots for different modes of standard electroconvection observed in Phase 5 was already presented in Fig. 1.12.

The morphology of EC basically remains the same even at ultra-low frequencies, just with larger angles of obliqueness.

The threshold voltages of electroconvection decrease monotonically as expected from higher frequencies until a minimum found at around 200 mHz. At the lowest frequencies,  $U_{cEC}$  is seemingly increased, and additionally the appearance of flexodomains were found, separated from electroconvection in time within the driving period. A typical snapshot of FDs found in Phase 5 could be seen in Fig. 1.13(a). The threshold voltage for flexodomains ( $U_{cFD}$ ) is also shown in Fig. 4.26 for the specific frequency of 30 mHz, where it was studied in detail. At  $f = 30$  mHz,  $U_{cFD}$  was found to be slightly higher than  $U_{cEC}$ . In the case of applying DC voltage, however, only flexodomains could be observed, indicating a crossover between the threshold voltages of electroconvection and of flexodomains below 30 mHz. This phenomenon could be deeply investigated in the case of a different calamitic compound (1008) presented later.

Previous studies of electroconvection at very low frequencies [78] used a compound (Phase 4) that exhibits dielectric electroconvection in the entire  $f$ -range. According to the time symmetry of the dielectric mode (see. Sec. 1.2.7), the director component perpendicular to the substrates ( $n_z$ ) oscillates with the applied electric field. This could be observed by the oscillation of the dielectric pattern with the double frequency of the driving signal, since the rolls for  $n_z$  and  $-n_z$  appears to be the same. Due to the sign reversal of  $n_z$ , the system has to go through the states where  $n_z = 0$ , when no pattern is visible at all. It was shown that at lower frequencies, where the director relaxation time  $\tau_d$  becomes comparable with the voltage period  $\tau$ , the presence of the homogeneous state where  $n_z = 0$  lasts not only for short time instants, but for longer. Moreover, at ultra-low frequencies the homogeneous state is visible predominantly in a driving period, and the dielectric pattern appears only at short time instants as flashes.

In the case of Phase 5, the conductive mode is visible below 230 Hz that exhibits basically a constant  $n_z$  (with a small  $2f$  modulation), due to the different time symmetry compared to the dielectric mode. Consequently the pattern contrast is expected to be almost constant within the driving period at high frequencies.

In order to quantify the patterns, the contrast was defined as the mean square deviation of the image intensities:  $C_s = \langle (\Phi_{ij} - \langle \Phi_{ij} \rangle)^2 \rangle$ , where  $\Phi_{ij}$  is the intensity of a single pixel and  $\langle \rangle$  denotes averaging over the whole image. This definition of contrast does not

allow to distinguish different pattern morphologies, but it is simple and effectively discriminates the undistorted homogeneous and the patterned state. Naturally, even in the basic state, where no voltage is applied on the cell, the contrast is not zero ( $C_{s0} \neq 0$ ) due to several reasons: e.g. the thermal fluctuations of the director, the optical aberrations of the imaging system, dust particles, etc. After switching the voltage to the cell, one or two complete driving periods were waited before the recording of the image sequences was started at the frequencies below 200 mHz. Experiments were performed to test how the results depend on the number of driving periods waited. It has turned out that completely similar contrast curves could be obtained after waiting 1, 10 or 50 periods, consequently there is no memory effect in the system at such low frequencies, which is in contrast to the high frequency electroconvection, where in most cases a number of cycles has to be waited until the steady state patterns become visible. Therefore, above 200 mHz five seconds of waiting time was applied independently of the used frequency.

In order to compare the image sequences recorded at various frequencies, the background subtracted normalized contrast was used with the definition:  $(C_s - C_{s0})/(C_{sm} - C_{s0})$ , where  $C_{sm}$  is the maximal contrast in an image sequence for a specific frequency. The background subtracted normalized contrast as the function of time within one driving period is plotted for different frequencies in Fig. 4.27(a), where  $t/\tau = 0$  corresponds to the time when the applied sinusoidal voltage changes its sign from positive to negative, thus the intervals of  $0 \leq t \leq \tau/2$  and  $\tau/2 \leq t \leq \tau$  refer to the negative and the positive half periods of the applied sine voltage. Nevertheless, the sign of the voltage is not relevant, since the cell is assumed to be symmetric.

It can well be seen that the contrast at 100 Hz is almost constant as it was expected; the small  $2f$  modulation is just perceptible. At one decade lower  $f$ , the contrast modulation becomes larger, but the pattern is still present in the entire time range. Decreasing the frequency to 1 Hz, however, gives rise to a qualitatively different behavior, namely the pattern is not always visible, since the contrast reaches the background value twice in a driving period. At even lower frequencies (100 mHz), the electroconvection patterns appear only in narrow time windows as short flashes. It can be observed that the height of the peaks are not equal in the positive and negative half periods. Theoretical calculations [P6] showed that this phenomenon may originate from the sensitive nature of the flashing electroconvection, namely a small DC offset in the applied voltage can brake

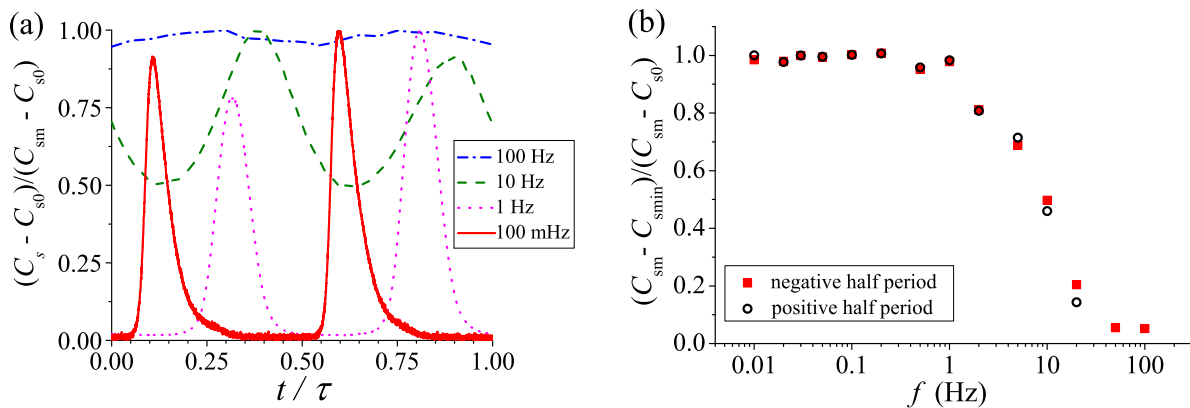


**Fig. 4.27:** (a) The time dependence of the normalized contrast within one voltage period ( $\tau$ ) at different driving frequencies measured for electroconvection in the compound Phase 5. (b) The frequency dependence of the relative contrast modulation.

the symmetry, resulting contrast peaks of different height in the positive and negative half periods of driving.

The relative contrast modulation can be defined as  $(C_{sm} - C_{smmin}) / (C_{sm} - C_{s0})$ , where  $C_{smmin}$  is the minimum contrast after a contrast maximum. This quantity is depicted as the function of  $f$  in Fig. 4.27(b), evaluated for the positive and negative half periods as well. The change of the pattern characteristics was illustrated in the examples of four distinct frequencies in Fig. 4.27(a), while plotting the relative contrast modulation for a number of frequencies (Fig. 4.27(b)) can give more information about how the transition from the regular to the flashing conductive electroconvection occurs as the function of frequency. It can be seen that the high and the low frequency limits correspond to the contrast modulations of almost zero and one, respectively. A gradual transition from the constant contrast to the flashing regime takes place at intermediate frequencies, from 30 Hz to 1 Hz. Using the known material parameters of Phase 5 [50, 101], the director relaxation time could be calculated by Eq. 1.33, resulting in  $\tau_d = 0.147$  s that corresponds to the frequency of  $\tau_d^{-1} = 6.8$  Hz. This frequency falls approximately in the middle of the transition, where  $(C_{sm} - C_{smmin}) / (C_{sm} - C_{s0}) = 0.5$  (see Fig. 4.27(b)), implying that the director relaxation time plays an important role in this effect.

In order to observe the time and voltage dependence of the flashing patterns, the image contrast ( $C_s(t)$ ) within the driving period at  $f = 30$  mHz is presented in Fig. 4.28(a) for several voltages. It can be seen that at the lowest voltage ( $U = 2.6$  V, red solid line),

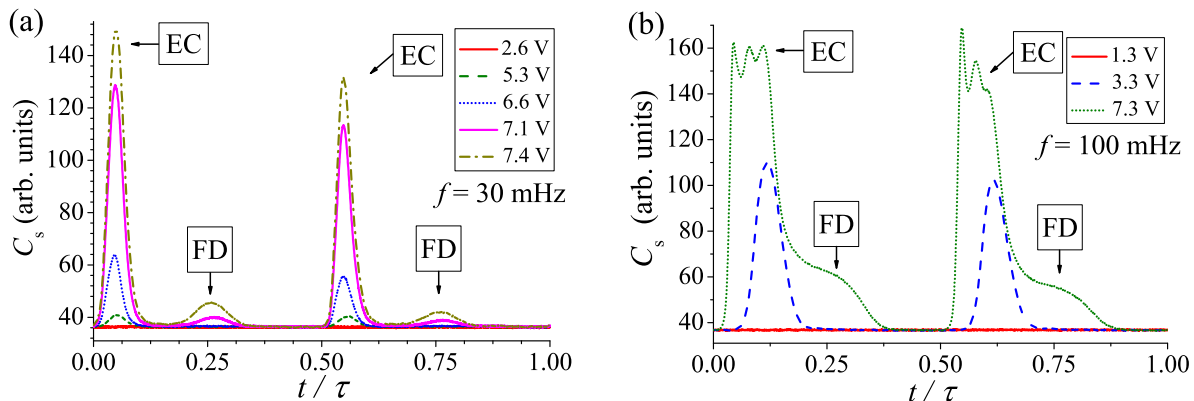


**Fig. 4.28:** The time dependence of the pattern contrast within one voltage period ( $\tau$ ) measured at (a)  $f = 30$  mHz and (b)  $f = 100$  mHz at various driving voltages on the compound Phase 5.

there are no patterns: the contrast is constant, it equals to the background value. Increasing  $U$  up to 5.3 V (dashed line), small humps appear around  $t \approx 0.05\tau$  and  $t \approx 0.55\tau$ , indicating the emergence of electroconvection. At  $U = 6.6$  V (dotted line), the contrast peaks of the electroconvection are further increased, then at even higher voltage ( $U = 7.1$  V, magenta solid line), other peaks appear at around  $t \approx 0.25\tau$  and  $t \approx 0.75\tau$ , corresponding to flexodomains. In the case of the top voltage presented ( $U = 7.4$  V, dash-dotted line), all peaks are increased, but still separated by time ranges where the contrast is at the background level.

In Fig. 4.28(b), the time dependence of the image contrast can be seen for different applied voltages at 100 mHz. The solid line corresponds to  $U = 1.3$  V that is below the thresholds of the patterns, thus the contrast is constant at the value of the background. The dashed line ( $U = 3.3$  V) shows the data for a state, where the electroconvection peaks are already well observable, but in different time instants compared to the case of  $f = 30$  mHz discussed above. This is apparently due to the frequency dependence of the times when the patterns emerge within a driving period. At a significantly increased voltage ( $U = 7.3$  V, dotted line), the convective instability can be seen much above its threshold in the highly nonlinear regime, where the corresponding contrast peaks do not show unambiguous maxima. Shoulders on the EC peaks can also be observed at this voltage level that correspond to the flexodomains. Nevertheless, the usual morphology of parallel stripes cannot be clearly identified in such cases, due to the perturbation by the electroconvection that has not yet completely decayed by the time when the flex-

odomains emerge. Due to the different  $f$ -dependence of the time instants of appearance, the separated flashes of electroconvection and flexodomains can be observed around  $f = 30$  mHz, and below only.

The  $C_s(t)$  curves for 30 mHz and 100 mHz indicated that the time instant (relative to  $\tau$ ), which characterizes the contrast peak of EC ( $t_{EC}/\tau$ ) depends on the frequency. In order to investigate this effect,  $t_{EC}/\tau$  is depicted as the function of  $f$  in Fig. 4.29(a), considering only one half period. Analogously,  $t_{FD}/\tau$  is defined as the relative time instant, when the peak of flexodomains reaches its maximum. The frequency dependence of  $t_{FD}/\tau$  can be also seen in Fig. 4.29(a), though in a much narrower  $f$ -range, since flexodomains could not be detected at higher frequency. In Fig. 4.29(a) it is immediately

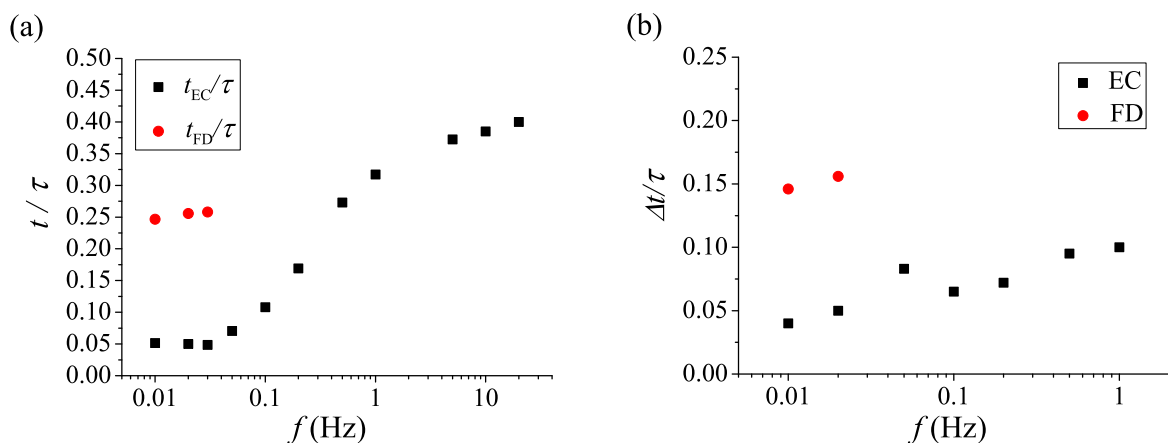


**Fig. 4.29:** (a) The relative time instant of the pattern flashes in the first half of the driving period  $\tau$  as the function of the driving frequency. (b) The half width of the contrast peak of the patterns versus the frequency.

seen that  $t_{EC}/\tau$  exhibits a significant dependence on the frequency. The values of  $t_{EC}/\tau$  decrease gradually from around 0.4, while  $f$  decreases from 10 Hz towards the ultra-low frequency regime. Below 50 mHz,  $t_{EC}/\tau$  is seemingly saturated to approximately 0.05. The few points, which could be measured for flexodomains, show that  $t_{FD}/\tau$  lies close to 0.25 that corresponds to time instant when the magnitude of the applied voltage is the highest.

The duration of a flashing pattern is characterized by the time interval  $\Delta t$  that equals to the half width of the corresponding contrast peak. The frequency dependence of  $\Delta t$  for electroconvection and flexodomains are presented in Fig. 4.29(b) for the low frequency regime, where the patterns can decay to the homogeneous state. It was found that  $\Delta t/\tau$

of electroconvection decreases slightly at lower frequencies, and the half width for the flexodomains is considerably larger than that of the electroconvection.

### 4.3.2 Flashing contrast and current

Similar characteristics of low frequency pattern formation were observed in the case of a different rod-like compound 1008 [P7]. Applying a sinusoidal voltage with a sufficiently low  $f$  and a high enough amplitude, the alternating flashes of oblique electroconvection rolls and flexodomains could be seen repeatedly just like in the case of Phase 5 presented before. The typical snapshots of EC and FD ( $f = 50$  mHz,  $U = 19$  V) observed using 1008 are shown in Fig. 4.30(a) and (b), respectively. The two dimensional Fourier transforms (power spectra) of the images are presented on the right. The rubbing direction lies horizontally.

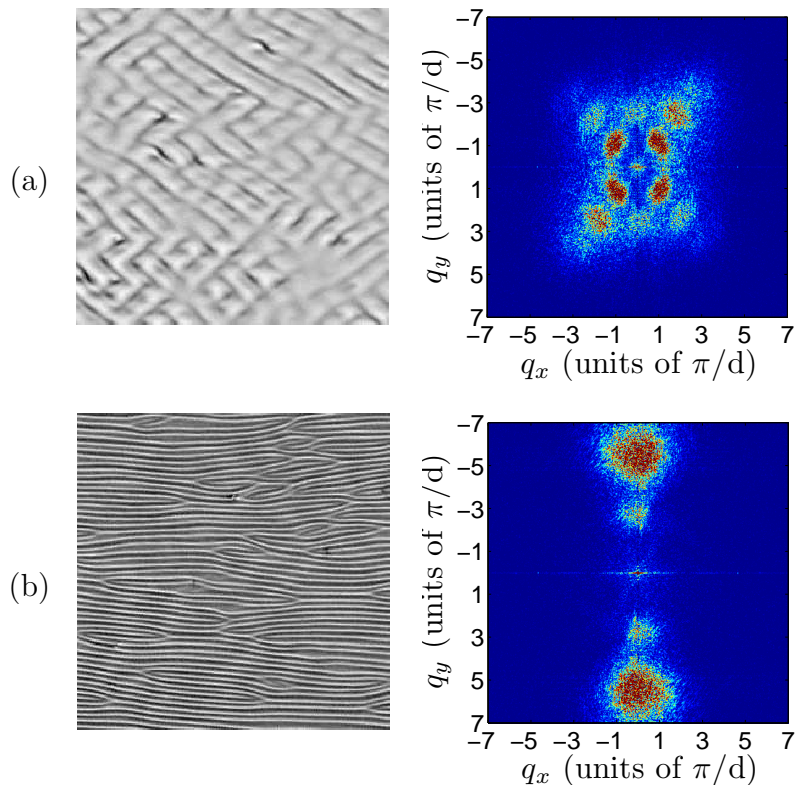


**Fig. 4.30:** Images and their Fourier transforms (a) for electroconvection and (b) for flexodomains recorded at  $f = 50$  mHz and  $U = 19$  V on the compound 1008. The images cover  $200 \mu\text{m} \times 200 \mu\text{m}$  area. The rubbing direction of the planar alignment layers is parallel with the horizontal direction.

In order to analyze the temporal evolution of patterns in the case of 1008, another Fourier transform based contrast definition ( $C_q$ ) was used besides the mean square devia-

tion of images discussed above. The two dimensional Fourier transforms of the snapshots were calculated, thus the characteristic wave vectors  $\mathbf{q}_c = (q_x, q_y)$  of the patterns could be found as the maxima in the Fourier-space. For each image,  $C_q$  was defined as the sum of the spectral intensities in a region around the  $\mathbf{q}_c$  of EC or FD, resulting  $C_{qEC}$  and  $C_{qFD}$ , respectively. The Fourier spectra in Fig. 4.30 clearly shows that  $\mathbf{q}_c$  is different for electroconvection and flexodomains, consequently  $C_{qEC}$  and  $C_{qFD}$  are sensitive only for the appearance of EC and FD, respectively. Therefore the Fourier based contrast definitions allow to distinguish the different patterns not only from the initial homogeneous state, but also between each other. It has to be noted that  $C_s$  and  $C_q$  is equivalent if the summation of the Fourier intensities is made on the range of the entire Fourier-space.

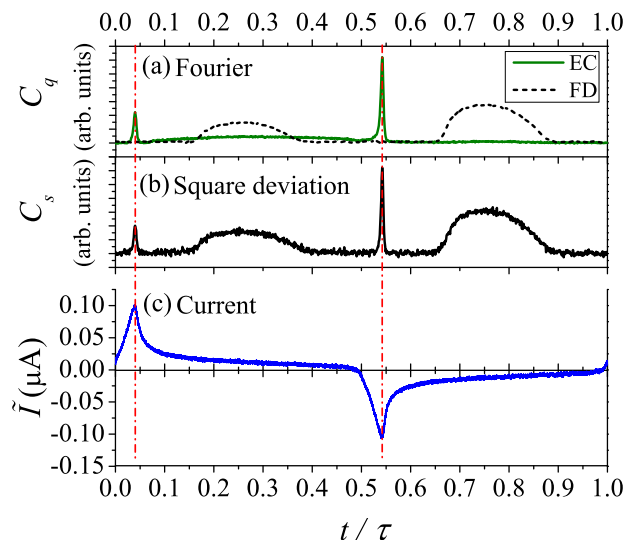


**Fig. 4.31:** The time dependence within a driving period  $\tau$  (a) for the contrast  $C_q$  obtained by Fourier technique; (b) for the contrast  $C_s$  calculated from the mean square deviation; and (c) for the electrical current  $\tilde{I}$  through the liquid crystal 1008.  $t = 0$  corresponds to the zero crossing (from positive to negative) of the applied sinusoidal voltage. The dashed-dotted lines indicate that the peaks of EC and of the current coincide.

In Fig. 4.31(a),  $C_{qEC}$  and  $C_{qFD}$  are presented as the function of  $t/\tau$  measured at  $\Delta T = -21.7$  °C using a  $10.4$   $\mu\text{m}$  thick cell driven by the sinusoidal voltage of  $f = 22$  mHz and  $U = 18$  V. It can be well seen that the curves of  $C_{qEC}$  and  $C_{qFD}$  (solid and dashed lines, respectively) exhibit only one type of peaks that correspond to the different patterns, showing that EC and FD are separated not only in time, but in the Fourier-space as well. In Fig. 4.31(b),  $C_s$  is plotted versus  $t/\tau$ , where both types of pattern peaks are

visible, looking like a quasi superposition of the  $C_{qEC}$  and  $C_{qFD}$  curves. The contrast based on the square deviation ( $C_s$ ) will be used later for simplicity.

The electrical current  $\tilde{I}$  in the driving circuit was measured simultaneously with the recording of the images.  $\tilde{I}$  can be seen as the function of  $t/\tau$  in Fig. 4.31(c). At the present combination of  $f = 22$  mHz and  $U = 18$  V, the current characteristics are far from the ohmic behavior that would result a harmonic response. The measured  $\tilde{I}(t/\tau)$  exhibits rather a strongly nonlinear behavior, showing peaks after each polarity change in the applied voltage. Surprisingly, the current peaks coincide very precisely with the flashes of the electroconvection as indicated by the dashed-dotted vertical lines in Fig. 4.31. In the case of numerous different frequencies, voltages, and temperatures, the peaks in the current and the EC flashes were found to be at the same time instants. Consequently, it can be concluded that their coincidence is not accidental.

It is important to note that the peaks in the current are also present at voltages much below the threshold of the EC, and in the isotropic phase as well, thus they do definitely not originate from the pattern formation. The nonlinear current characteristics is assumed to be a more robust phenomenon explained by the ionic conductivity of the material and the presence of insulating polyimide layers on the electrode surfaces of the cell.

Regular organic liquid crystals are considered weak electrolytes that means their small conductivity is attributed to the low concentration of ionic contaminations. At very low frequencies, the current originates mainly from the ionic contribution, since the capacitive term is very small. Using  $\varepsilon_{\perp} = 4.5$  at  $f = 22$  mHz and  $U = 18$  V, the capacitive current is in the order of 1 nA, which is one order of magnitude smaller than the current scale in Fig. 4.31(c). The ionic conductivity arises due to the low concentration of ions that are accelerated by the applied electric field. If the field changes slowly, the charge carriers have time to accumulate at the boundaries forming double layers, because the charge injection is hindered by the insulating polyimide surfaces. At the polarity reversal, the forces acting on the charges turn to the opposite direction causing a large ionic flow, since the previously formed double layers has to be destroyed and built up on the opposite electrodes.

Several models were developed [102, 103, 104, 105, 106, 107, 108, 109, 110] in order to describe quantitatively the behavior of weak electrolytes in electric fields. Since a

complete description should account for a number of phenomena such as: the generation and recombination of ions; different mobilities, diffusion coefficients and charges of ionic species; surface adsorption; charge injection; chemical reactions; voltage attenuation due to the orienting layers, therefore these theories are very complex. Moreover, their goal is mostly to describe the linear response of the system restricting themselves to the cases of small electric fields that can be accessed experimentally by dielectric spectroscopy.

Nevertheless, there are some recent theoretical studies [102, 103] that presented calculations of the nonlinear current response to low frequency sinusoidal voltage driving showing similar nonlinear  $\tilde{I}(t)$  characteristics that were actually measured on 1O08.

Including the weak electrolyte properties (ionic dissociation and recombination) of nematics to the description of standard electroconvection [111] led to the understanding of the travelling EC rolls observed at around a few 10 Hz. Pattern formation phenomena coupled to electrolytic effects in nematics, however, have not been studied at low frequencies due to the complexity of such systems.

### 4.3.3 Threshold characteristics

The basic characterization of flexodomains and electroconvection involves the analysis of the threshold parameters, namely the threshold voltages  $U_{cFD}$ ,  $U_{cEC}$  and the critical wave numbers  $q_{cFD}$ ,  $q_{cEC}$ , respectively. At high frequencies (e.g. above 10 Hz), the EC patterns appear a few seconds after the driving voltage exceeds  $U_{cEC}$ , thus the thresholds can be conveniently determined manually by looking at the microscopic images. At lower frequencies, however, this method becomes very time consuming and inconvenient, since the driving period can be quite long, and the patterns appear only in narrow time windows as short flashes. Nevertheless, it can be done as one could see in the case of Phase 5 above.

The more precise determination of a threshold voltage in general requires much more data to record and more efforts in the evaluation as well. A plausible solution is to determine the curves of  $C_s(t/\tau)$  as the function of  $U$ . The contrast curves recorded at several voltages were already presented for Phase 5 in Fig. 4.28, however, in order to precisely determine  $U_c$ , much smaller steps in the voltage should be applied. The threshold characteristics of a pattern can be studied by plotting the maximal contrast  $C_{sm}$  in a time window, where the contrast peak emerges, as the function of  $U$ . If a

pattern flash is visible, naturally  $C_{sm}$  corresponds to the height of the contrast peak, while well below  $U_c$ , it equals to the background contrast.

The relation between the modulated director above the threshold of an instability, and the contrast of the resulting shadowgraph image has to be known in order to interpret the experimental data properly. The voltage dependence of the contrast close to the thresholds was given in the literature [78] for electroconvection and flexodomains as well, yielding the relations:  $C_{mEC} \propto U$  and  $C_{mFD} \propto U^2$ . Consequently,  $C_{smEC}$  and  $\sqrt{C_{smFD}}$  should increase linearly with the applied voltage in the vicinity of the thresholds.

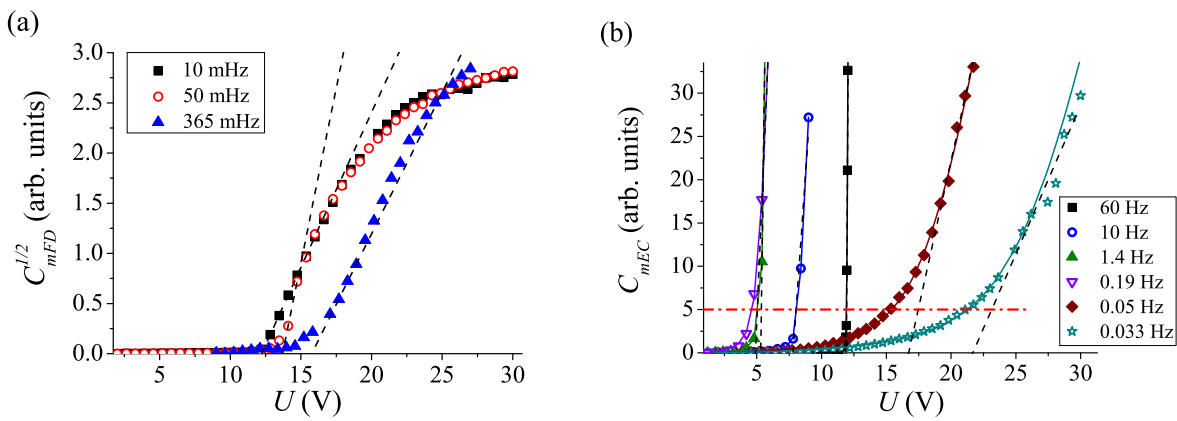


**Fig. 4.32:** (a) The voltage ( $U$ ) dependence of the square root of the flexodomain (FD) contrast peaks for several frequencies (symbols) measured on 1008. The dashed lines indicate the threshold determination by linear extrapolation (method A). (b) The  $U$  dependence of the contrast peaks of electroconvection (EC) for various frequencies (symbols). The dash-dotted line shows the discriminating contrast level for the threshold determination using method B. Solid lines are fits with the imperfect bifurcation model, the dashed lines indicate the linear extrapolation for method A.

The experimental data with subtracted background contrast for  $\sqrt{C_{mFD}}(U)$  are presented in Fig. 4.32(a) in the case of several frequencies. The threshold behavior can well be seen. At lower voltages the contrast equals to the background value; then at  $U_{cFD}$ ,  $\sqrt{C_{smFD}}$  starts to increase that can be fitted by a line. Although the  $\sqrt{C_{mFD}}(U)$  curve barely deviates from the linear behavior at the threshold, slightly above appropriate intervals can be found that are well fitted by the lines. The values of  $U_{cFD}$  then could be determined by taking the voltages where the fitted lines cross the background level. This procedure to obtain the threshold voltages is referred to as method A later.

The maximum contrast of EC as the function of the voltage is presented in Fig. 4.32(b) in the case of different frequencies. It is spectacular that not only the threshold voltage

but the shape of the  $C_{mEC}(U)$  curves is also frequency dependent. At higher  $f$ , the thresholds are quite sharp, but below 1 Hz, this character becomes gradually smoother, therefore in the low frequency regime the linear  $U$  dependence of  $C_{smEC}(U)$  is not satisfied. As a consequence, the threshold determination using method A at low frequencies becomes less adequate, since there are no well defined linear parts of the contrast curves. The fits (see the dashed lines in Fig. 4.32(b)) were performed on the intervals, where the second derivatives of the  $C_{mEC}(U)$  curves were approximately zero.

Method B is an alternative procedure of the threshold estimation based on the actual visibility of the EC patterns. A low discriminating level of contrast  $C_{discr} = 5$  was selected arbitrarily shown by the dashed-dotted line in Fig. 4.32(b). For a given frequency, the threshold voltage  $U_{cECB}$  was chosen as the value, where the contrast curve crossed the discriminating level, thus  $C_{mEC}(U_{cECB}) = C_{discr}$  was satisfied.

The third type of procedure (method C) to obtain information about the EC thresholds uses a phenomenological description of imperfect bifurcations developed by Alexei Krekhov. A general amplitude equation for an imperfect bifurcation is applied for the case of EC:

$$\Upsilon \hat{A} - \hat{g} \hat{A}^3 + \hat{\delta} = 0, \quad (4.4)$$

where  $\hat{A}$  corresponds to the amplitude of the director deformation,  $\Upsilon = U^2/U_{cEC}^2 - 1$  is connected to the (rms) voltage relative to the threshold,  $\hat{g} > 0$  characterizes the saturation of  $\hat{A}$ , and  $\hat{\delta} \geq 0$  accounts for the imperfection of the bifurcation. The perfect case corresponds to  $\hat{\delta} = 0$ . It was shown that Eq. (4.4) has one relevant stable solution for  $\hat{g} > 0$ ,  $\hat{\delta} > 0$ , and  $\Upsilon > -1$  that is given by:

$$\begin{aligned} \hat{A} &= \left(\frac{\hat{\delta}}{2\hat{g}}\right)^{1/3} F(\tilde{\Upsilon}), \\ F(\tilde{\Upsilon}) &= \left(\frac{\tilde{\Upsilon}}{\hat{f}(\tilde{\Upsilon})} + \hat{f}(\tilde{\Upsilon})\right), \text{ for } \tilde{\Upsilon} \leq 1, \\ F(\tilde{\Upsilon}) &= 2\sqrt{\tilde{\Upsilon}} \cos\left(\frac{1}{3} \arctan(\sqrt{\tilde{\Upsilon}^3 - 1})\right), \text{ for } \tilde{\Upsilon} > 1, \\ \tilde{\Upsilon} &= \frac{2}{3} \frac{\Upsilon}{(2\hat{g}\hat{\delta}^2)^{1/3}}, \quad \hat{f}(\tilde{\Upsilon}) = (1 + \sqrt{1 - \tilde{\Upsilon}^3})^{1/3}. \end{aligned} \quad (4.5)$$

The measurable contrast of the EC pattern ( $C_{smEC}$ ) is proportional to  $\hat{A}^2$ . In order to demonstrate the effect of the imperfection, the voltage dependence of  $\hat{A}^2$  is presented

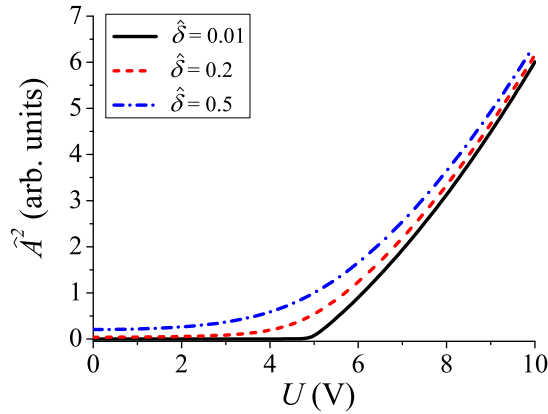


**Fig. 4.33:** The square of the pattern amplitude  $\hat{A}^2$  as the function of the applied voltage  $U$  for  $\hat{\delta} = 0.01$  (solid line),  $\hat{\delta} = 0.2$  (dashed line), and  $\hat{\delta} = 0.5$  (dot-dashed line), calculated using Eq. (4.5) with  $U_{cEC} = 5$  V,  $\hat{g} = 0.5$ .

in Fig. 4.33 using  $U_{cEC} = 5$ ,  $\hat{g} = 0.5$ , with  $\hat{\delta} = 0.01$  (solid line),  $\hat{\delta} = 0.2$  (dashed line), and  $\hat{\delta} = 0.5$  (dash-dotted line). The characteristics of the curves are as expected, namely the larger  $\hat{\delta}$  parameter results in a smoother threshold. In order to perform an adequate fit on the experimental data, the background subtracted contrast  $C_{smEC}$  is connected to  $\hat{A}^2$  by:

$$C_{mEC}(U) = \hat{a} \left( \hat{A}^2(U) - \hat{A}^2(U = 0) \right), \quad (4.6)$$

where  $\hat{a}$  is a proportionality constant depending on the optical parameters of the material and the imaging system. The combination of Eqs. (4.5) and (4.6) gives the opportunity to fit the experimental curves of  $C_{smEC}(U)$  using four fit parameters:  $\hat{a}$ ,  $\hat{g}$ ,  $\hat{\delta}$  and  $U_{cEC}$ .

Assuming that the optical parameters do not depend much on  $f$ , the proportionality factor  $\hat{a}$  determined for  $f = 60$  Hz was used and kept constant for the lower frequencies in order to reduce the number of the fit parameters. The resulting fit curves can be seen in Fig. 4.32(b) as solid lines. Apparently the experimental data could well be fitted using method C in the entire studied  $f$ -range.

In Fig. 4.34, the imperfection parameter is shown as the function of  $f$ . At high frequencies,  $\hat{\delta}$  is close to zero meaning a sharp threshold behavior, as expected. Towards lower frequencies, however, it increases yielding the larger imperfection in accordance with the smoothing of the thresholds observed in the experimental data.

An explanation for the lack of the sharp thresholds at lower frequencies is based on the effect of the nonlinear current characteristics presented above. The massive ionic flow definitely plays an important role in the emergence of the electro-hydrodynamical

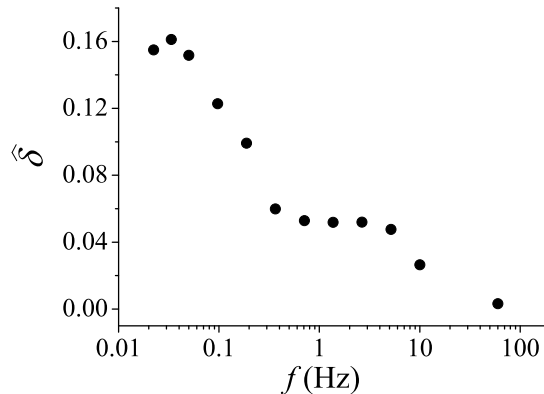


**Fig. 4.34:** The frequency dependence of the imperfection parameter  $\hat{\delta}$  obtained from fits with the imperfect bifurcation model.

instability, since the contrast of the EC pattern is maximal exactly when the largest current is measured. Additionally, the current might have not just strong temporal, but a spatial dependence as well, mainly due to surface inhomogeneities or small variations in the cell thickness. The microscopic unevenness of the substrate can be actually observed in the microscope, and it could originate from e. g. the crystallization of the compound at room temperature. Consequently, in the case of an applied voltage well above the threshold, a two-dimensional current distribution would lead to the modulation of the local contrast, because the EC pattern would be locally more (or less) emerged depending on the larger (or smaller) local currents. Modulations are also observable in Fig.4.30(a) as different patches with larger and smaller contrast. These are definitely not from the inhomogeneities in the imaging system, since the contrast of the image of flexodomains is quite homogeneous (see Fig. 4.30(b)). The contrast inhomogeneities around the onset of the instability naturally result in the softening of the threshold characteristics by having areas only partially covered by the electroconvection pattern. The stronger threshold softening at lower frequencies could be explained by the larger nonlinearities in the current towards low  $f$ .

The frequency dependence of the threshold voltages for electroconvection and flexodomains can be seen in Fig. 4.35, where the values of  $U_{cEC}$  determined from the different procedures, namely the linear extrapolation (method A), the discriminating contrast level (method B), and the imperfect bifurcation fit (method C), are all presented. The data obtained using methods A and B are very similar, while method C gave larger thresholds at lower frequencies, which is due to the fact that the inhomogeneous state

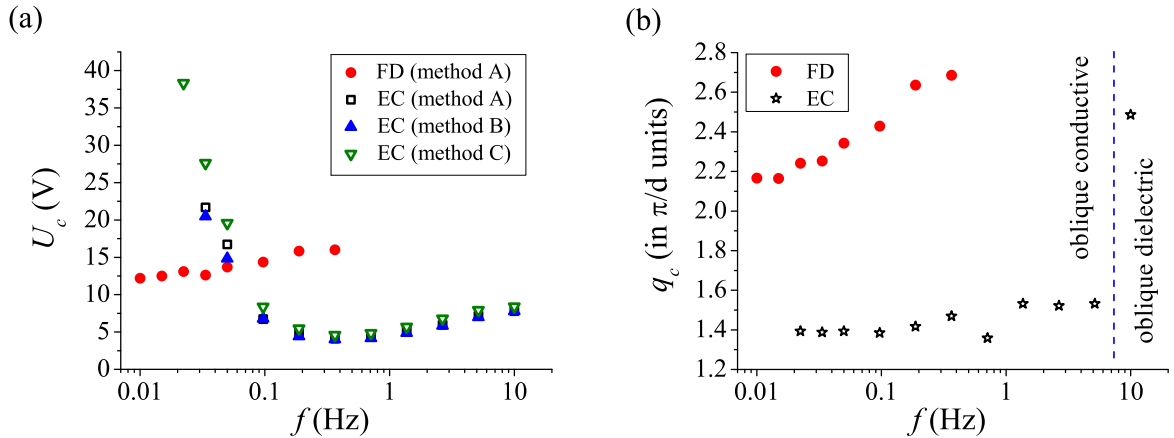


**Fig. 4.35:** (a) The threshold voltage of electroconvection (EC) and flexodomains (FD) determined from various methods as the function of frequency on 10O8. (b) The frequency dependence of the critical wave numbers for EC and FD.

can be observed below the threshold in the case of an imperfect bifurcation, in contrast to the assumptions of method A and method B.

The thresholds of EC decrease while lowering the frequency in the range of  $0.5 \text{ Hz} < f < 10 \text{ Hz}$  that is in accordance with previous theoretical and experimental findings in other liquid crystals [50]. The increase of  $U_{cEC}$  at very low frequencies might be explained by an internal voltage attenuation originating from the insulating polyimide layers, or due to the screening of the ionic double layers close to the substrates. Since there are no theoretical calculations yet that include the crucial effect of ions on the formation of low frequency EC, the precise explanation for the experimental result cannot be given.

The  $f$ -dependence of  $U_{cFD}$  seems to be significantly weaker than that of  $U_{cEC}$  at the low frequency regime. Considering an internal voltage attenuation that is larger at lower frequencies, the actual threshold voltages would decrease towards  $f \rightarrow 0$ . A stronger  $f$ -dependence of  $U_{cFD}$  was shown by recent theoretical calculations [57] as well, though using the material parameters of a different nematic compound.

In Fig. 4.35(a), the thresholds of EC and FD can be seen at the same frequencies in a relatively wide  $f$ -range, showing that the distinct patterns could be observed separately in a much broader frequency range than in the case of Phase 5. The separated appearance of EC and FD could even be detected, when their thresholds were significantly different; that was possible because of the time instants of their emergence within a driving half period were sufficiently different. At frequencies higher than 0.4 Hz, however, a merging

of the corresponding contrast peaks could be observed, similarly to the case of Phase 5 at  $f = 100$  mHz presented in Fig. 4.28(b).

At around 50-70 mHz, the threshold curves for EC and FD cross each other, interestingly, as it can be seen in Fig. 4.35(a). At higher frequencies  $U_{cFD} < U_{cEC}$ , while at lower  $f$  the relation is the opposite. Applying pure DC voltage on the cell filled with 1O08 only flexodomains could be observed, similarly to the case of Phase 5.

The apparent critical wave numbers ( $q_c = |\mathbf{q}_c|$ ) of electroconvection and flexodomains ( $q_{cEC}$  and  $q_{cFD}$ , respectively) were determined slightly above the thresholds at  $U = 1.05U_c$  in order to have sufficient contrast for the evaluation. The values of  $q_{cEC}$  and  $q_{cFD}$  were obtained by fitting the relevant peaks in the two dimensional Fourier intensity spectra (see Fig. 4.30) of the images with Gaussian surfaces. The frequency dependence of the critical wave numbers in units of  $\pi/d$  can be seen in Fig. 4.35(b).

The wave numbers moderately grow for both patterns with increasing frequencies. The relation  $q_{cEC} < q_{cFD}$  holds in the entire  $f$ -range, in accordance with the considerably larger periodicity seen for EC in Fig. 4.30. At around  $f_c \approx 7$  Hz, the sudden change in  $q_{cEC}$  refers to the transition from the conductive to the dielectric electroconvection, further supported by the snapshots taken at 5.2 Hz and 10 Hz, in Fig. 4.36 (a) and (b), respectively. The peculiarity of this transition is that the convection rolls in both the conductive and the dielectric modes are oblique; the Lifshitz-point is reached at  $f_{Lif} \approx 80$  Hz, in the dielectric regime. This is in contrast with the usual characteristic relation of  $f_{Lif} < f_c$ . No previous indications were found in the literature for a situation of  $f_{Lif} > f_c$  that was actually exhibited by 1O08.

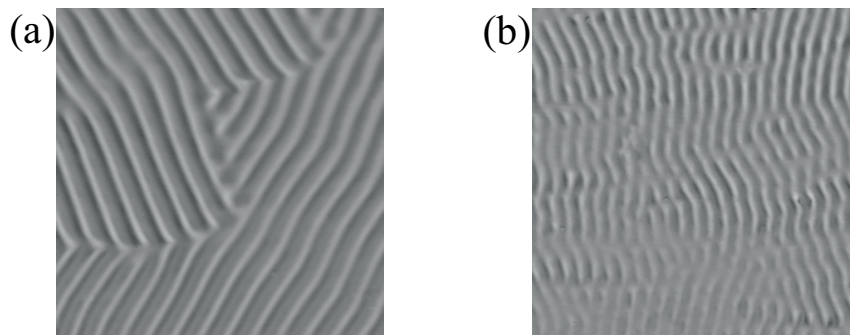


**Fig. 4.36:** The images of (a) oblique conductive and (b) oblique dielectric electroconvection rolls recorded on the compound 1O08 at 5.2 Hz and 10 Hz, respectively. The images cover  $200 \mu\text{m} \times 200 \mu\text{m}$  area. The rubbing direction of the planar alignment layers is parallel with the horizontal direction.

### 4.3.4 Determination of the flexoelectric coefficients

A reliable and precise experimental method for the determination of flexoelectric coefficients does not exist yet. A possible technique is to use the threshold parameters ( $q_{cFD}$ ,  $U_{cFD}$ ) of the flexoelectric instability. The drawback of this is that only a few compounds show FDs, since the material needs to have very low dielectric anisotropy according to the requirement presented in Sec. 1.2.7. Furthermore, the liquid crystal should contain sufficiently low amount of ionic impurities in order to avoid large screening effects, and no other phenomena (e.g. EC or Fredericksz-transition) should influence the homogeneous planar state below the threshold of FD.

The evaluation of  $|e_1 - e_3|$  could be done by using the equation below obtained by combining Eq. (1.35) and Eq. (1.36):

$$|e_1 - e_3| = \sqrt{\varepsilon_0 \varepsilon_a K \frac{1 + q_{cFD}^2}{1 - q_{cFD}^2}}. \quad (4.7)$$

In the case of 10O8,  $q_{cFD}$  and  $U_{cFD}$  were determined as the function of temperature using 10 mHz AC sinusoidal voltage as presented in Fig. 4.37. The frequency of 10 mHz

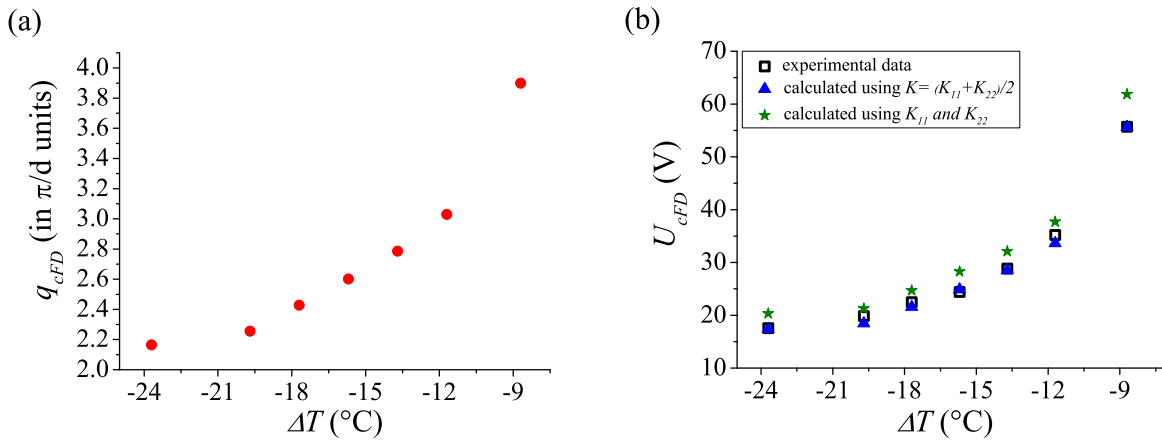


**Fig. 4.37:** The temperature dependence of (a) the critical wave number of flexodomains, and (b) the measured and calculated threshold voltage amplitudes of flexodomains in 10O8.

was assumed to be low enough to be considered as a quasi-static case, thus the results were fitted by the models developed for DC voltages. Consequently the threshold voltages in Fig. 4.37 correspond to the actual voltage values that can be measured in the time instants, when the flexodomains appear that equals to the amplitudes of the sine voltages

with a good approximation. It can be seen in Fig. 4.37 that  $q_{cFD}$  and  $U_{cFD}$  increase with the temperature. Above  $\Delta T = -8$  °C, the FD patterns could not be detected up to 135 V.

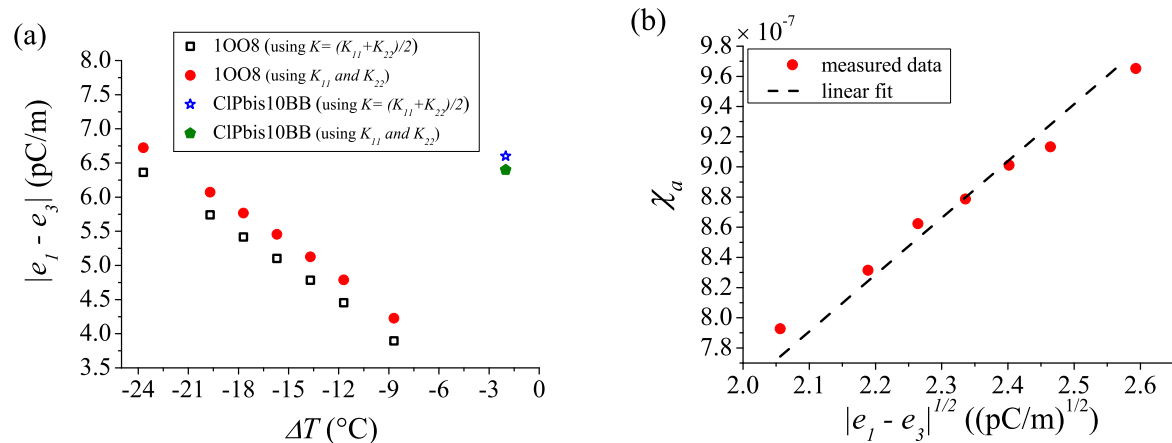


**Fig. 4.38:** (a) The combination  $|e_1 - e_3|$  of the flexoelectric coefficients measured on 1008 as the function of temperature, and on ClPbis10BB at  $\Delta T = -2$  °C. (b) The diamagnetic susceptibility anisotropy as the function of  $\sqrt{|e_1 - e_3|}$  measured on 1008 (symbols). The dashed line corresponds to a linear fit through the origin according to Eq. (4.9).

The temperature dependence of  $|e_1 - e_3|$ , evaluated by two methods using the material parameters of 1008 presented in Sec. 4.2.4 can be seen in Fig. 4.38(a). The first method applied Eq. (4.7) that assumes the one-elastic-constant approximation, thus  $K = (K_{11} + K_{22})/2$  was used (square symbols). The second type of evaluation was done by Alexei Krekhov, using his numerical calculations (circle symbols) that take into account the anisotropic elasticity ( $K_{11} \neq K_{22}$ ), based on the theory published recently [57]. The second technique resulted in values about 7% higher than those obtained by the first method. The values of  $|e_1 - e_3|$  fall in the regular range of that of rod-like nematics.

In order to check the consistency of the models, the corresponding threshold voltages were calculated using  $|e_1 - e_3|$  obtained from  $q_{cFD}$ . The results are shown in Fig. 4.37(b). In average, the first model gave 2% lower, while the second 11% higher values for  $U_{cFD}$  than the experiments.

The knowledge of  $|e_1 - e_3|$  as the function of temperature gives the opportunity to compare the results with the predictions of the molecular theory of flexoelectricity. The

theoretical [62, 112, 113] studies showed that the difference of flexoelectric coefficients should be proportional to the square of the order parameter  $S(T)$ :

$$|e_1 - e_3| = \hat{e}S^2(T), \quad (4.8)$$

where the proportionality constant is denoted by  $\hat{e}$ . The order parameter of 1008 as the function of  $T$  was already determined using  $\chi_a = \hat{\chi}S(T)$  (Eq. (4.1)). The combination of Eq. (4.8) and Eq. (4.1) yields:

$$\chi_a = a\sqrt{|e_1 - e_3|}, \quad (4.9)$$

with  $a = \hat{\chi}/\sqrt{\hat{e}}$ .

In Fig. 4.38(b), the measured values of  $\chi_a$  are plotted versus the calculated  $\sqrt{|e_1 - e_3|}$  for the same temperatures, using the model with anisotropic elasticity. The data points could be well fitted by a line that goes through the origin (dashed line), thus the predicted relation defined in Eq. (4.9) seems to be confirmed. The single fit parameter  $a$  was found to be:  $a = 0.38(C/m)^{-0.5}$  that with  $\hat{\chi}$  determined in Sec. 4.2.4, yields  $\hat{e} = 18.6$  pC/m.

Flexodomains could be observed in the case of the bent-core compound ClPbis10BB, and the characteristics of the low frequency pattern formation was found to be qualitatively similar to those of Phase 5 and 1008, thus a detailed analysis will not be presented. Nevertheless, the appearance of FDs gives the opportunity to determine  $|e_1 - e_3|$  using especially the theory that takes into account the elastic anisotropy, which was found to be very unusual for ClPbis10BB, as presented in Sec. 4.2.1. Using a quasi-DC excitation ( $f = 1$  mHz, square wave) of a  $6.4 \mu\text{m}$  thick planar cell filled with the bent-core compound, the critical voltage and wave number were determined as  $U_{cFD} = 3.3$  V and  $q_{cFD} = 1.6$  (in  $\pi/d$  units) at  $\Delta T = -2$  °C, where the elastic constant values were available. The values of  $|e_1 - e_3|$  calculated by the theories using the one-elastic-constant approximation (6.6 pC/m) and the elastic anisotropy (6.4 pC/m) are shown in Fig. 4.38(a). The first consequence of the results is that the reproduction of the giant flexoelectric coefficient ( $\sim \text{nC/m}$  [60, 61]) was not succeed with the methods used, thus the current findings rather support those electro-optical experiments that gave just slightly larger flexoelectric coefficients, but within the same order of magnitude for bent-cores compared to rod-like nematics [67, 114]. The second consequence is that the values

of  $|e_1 - e_3|$  determined differently were almost the same, yielding that the evaluation using the one-elastic-constant approximation gives sufficiently good results compared to the more precise theory considering elastic anisotropy, even in the range of the unusual elasticity of ClPbis10BB.

### 4.3.5 Conclusions

The time resolved experimental studies of pattern formation revealed how the standard conductive electroconvection turns into a qualitatively different regime by decreasing the frequency in the case of the compound Phase 5 [P5, P6]. The transition from the state with approximately constant contrast to the flashing appearance of EC could well be observed in Fig. 4.27, showing the important role of the different time scales in the system. The frequency dependence of the relative contrast modulation in Fig. 4.27(b) indicated three regimes that are characterized by the relation between the driving period  $\tau$  and the director relaxation time  $\tau_d$ . The well known steady patterns of the conductive EC at high frequencies ( $\tau \ll \tau_d$ ) are observable as short flashes at very low  $f$  ( $\tau \gg \tau_d$ ). Between these two limits, an intermediate regime was found around  $\tau \approx \tau_d$ , where the EC pattern was present in the entire driving period, but with a temporally modulated contrast.

In parallel with the experimental investigations, theoretical calculations [P6] were performed by Alexei Krekhov based on the linear stability analysis of the nemato-electrohydrodynamic equations using the material parameters of Phase 5. These studies [P6] aimed to simulate the characteristics of the pattern formation, including electroconvection and flexodomains as well, in the same wide frequency range that was used in the experiments. The experimental and theoretical findings showed good qualitative agreement in the entire studied frequency range, although quantitative discrepancies were pointed out in the low frequency regime: the time instants of appearance of the patterns in the driving period ( $t_{EC}/\tau$ ,  $t_{FD}/\tau$ ) were found to be larger theoretically than experimentally. The calculations also showed slightly lower threshold voltages than the measurements at very low frequencies. Nevertheless, these discrepancies could be partially reduced by approximating the voltage attenuation and a phase shift of the driving voltage due to the joint effect of the alignment layers and the ionic shielding.

The later measurements on 1008 [P7] showed a direct connection between the appearance of the EC patterns and the nonlinear current peaks, indicating that the ionic flow plays a crucial role in the emergence of the EC flashes. Consequently, the quantitative discrepancies between the experiments on Phase 5 and the theory that considers only ohmic conductance, are not surprising. The complete understanding of the current-pattern coupling could be served by a future theory of low frequency pattern formation that involves ionic effects via the implementation of the weak electrolyte model.

The threshold behavior of electroconvection and flexodomains showed a significant difference at low frequencies in the case of 1008. The voltage dependence of the peak contrasts indicated a softening of the threshold for EC towards low  $f$ , in contrast to FDs that exhibited sharp thresholds in the entire studied frequency range. The flattening of the  $C_{smEC}(U)$  curves could be fitted by an empirical description of imperfect bifurcations, yielding a gradual increase of the imperfection towards low frequencies. A qualitative explanation of this effect was also given by the role of the ions, though a sophisticated model with numerical calculations would be necessary to confirm this hypothesis.

The frequency dependence of  $U_{cEC}$  and  $U_{cFD}$  were found to be different at low frequencies, and a crossover was observed between the two pattern forming mechanisms at around 60 mHz. The experimental findings implied this effect in the case of Phase 5, however, it could be clearly demonstrated on 1008. Moreover on 1008, the time separated flashes of EC and FD could be observed within a half period of driving, in spite of their different thresholds, in a much broader frequency range than in the case of Phase 5.

Additionally, 1008 exhibited a crossover from the conductive to the dielectric electroconvection modes at  $f_c \approx 7$  Hz that was interesting because the convection rolls were found to be oblique in both the conductive and the dielectric regimes. This means that the Lifshitz-frequency is higher than  $f_c$ , which was unprecedented before in the literature. Nevertheless, the first observation of oblique dielectric rolls was reported recently [78], but the compound in that case did not show conductive electroconvection rolls at all.

Determining the critical wave number of FDs gave the opportunity to calculate the flexoelectric parameter  $|e_1 - e_3|$  using the classical theory of flexodomains with one-elastic-constant approximation, and also with the novel theory that takes into account

both  $K_{11}$  and  $K_{22}$ . The calculations were performed on 1O08 as the function of  $\Delta T$ , as well as in the case of the bent-core compound ClPbis10BB at the temperature, where the elastic constants were known.

It has turned out that the values of  $|e_1 - e_3|$  determined from the different theories fall close to each other. This is due to the fact that the relevant material parameters ( $K_{11}$ ,  $K_{22}$  and  $\varepsilon_a$ ) of 1O08 and ClPbis10BB lie in that range, where  $q_{cFD}$  is only slightly sensitive to the elastic anisotropy. The actual values of  $|e_1 - e_3|$  fall in the expected range for regular nematics for both compounds, thus no signs of giant flexoelectricity were found on ClPbis10BB.

The temperature dependent data of 1O08 could be used to confirm the relation  $|e_1 - e_3| \propto S^2$  predicted by the molecular theory of flexoelectricity.

## 5. Summary and outlook

The dielectric spectroscopy measurements (see Sec. 4.1) [P1, P4] showed altogether five relaxations in the nematic phase of ClPbis10BB that is by two more than in the case of the usual rod-like compounds. The larger number of relaxations cannot be explained by the polar rod model that satisfactorily provided the theoretical explanation for the experimental findings in calamitics. Moreover, the relaxation frequencies determined in the case of the bent-core compound are significantly lower compared to rod-like liquid crystals, even in the isotropic phase. The lowest frequency nematic relaxation was detected at around a few kHz in the parallel component. This finding actually confirms the original assumption of the presence of a low frequency relaxation based on earlier measurements of conductivity (see Sec. 2.1).

Without a satisfying match between the measurements and a proper theoretical description, the origin of the relaxations found in ClPbis10BB cannot be given unambiguously. Since there is no theory of dielectric relaxations available currently that could handle bent-shaped molecules, only qualitative explanations can be given. The unusual dielectric behavior of ClPbis10BB might be attributed to the biaxial symmetry of the bent-shaped molecules, that can allow more rotation modes than in the case of calamitics. Moreover, the polar rod model considers the molecules as rigid rods, which is also not true for ClPbis10BB, as it was shown by the conformational calculations. Consequently, the large conformational freedom might also affect the dielectric spectra. It cannot be excluded, that the relaxation found at around a few kHz may originate from the presence of polar smectic clusters.

The findings about such clusters in bent-core nematics has become widely accepted by now. The earlier [66] and the most recent small angle X-ray scattering studies [88, 89, 90], that indicated this spectacular form of short range order, are supported by direct observation of clusters achieved using cryo transmission electron microscopy [115]. The low frequency relaxation observed in the binary system of ClPbis10BB and 6OO8 became undetectable at concentrations  $X > 0.8$ , in accordance with the disappearance of the

smectic clusters studied by X-ray scattering experiments on the same mixtures [90]. The dielectric relaxations measured in the mixtures could be interpreted as the superposition of the modes found in the bent-core and calamitic compounds.

Dielectric spectroscopy studies [100] on a different bent-core compound were published approximately at the same time as [P1]. Similar sequence of relaxations was found as in the case of CIPbis10BB, showing that the unusual dielectric properties are observable not only on the bent-core material that we have studied. Later, a different group using another bent-core nematic liquid crystal could reproduce the results found on CIPbis10BB [116]. Those authors also explained their findings by the conformational freedom and the presence of smectic clusters in bent-cores.

It was shown in Sec. 4.2.1 that not only the dielectric, but the elastic properties of CIPbis10BB are extraordinary as well. The analysis of the Freedericksz-transition experiments allowed to determine all three elastic constants of the bent core compound [P2]. The results revealed that the twist ( $K_{22}$ ) and bend ( $K_{33}$ ) elastic constant are one order of magnitude smaller than in the case rod-like nematics, while the splay elasticity ( $K_{11}$ ) was found to be usual. Similar values of elastic constants were determined by co-workers performing dynamic light scattering experiments [P2]. The findings were explained by the presence of smectic clusters that can be chiral containing twist and bend deformations in their structures. The previous indications of the unusual ratios of elastic constants [75, 76, 77] in bent-core nematic liquid crystals became verified in a direct way.

The magnetic twist Freedericksz-transition was studied by numerical simulations in the presence of director pretilt (Sec. 4.2.2) [P3]. It was shown that the nonzero pretilt allows to determine the twist elastic constant  $K_{22}$  using a dielectric technique that was not utilized before in the twist geometry. The optical transmittance as the function of the applied magnetic field was calculated numerically in the case of a planar cell with various thickness and pretilt values. It has turned out that a considerably high pretilt might result in an oscillating transmittance in contrast to the expectation of a monotonic increase with the magnetic field that stands only for low values of pretilt. It was quantitatively shown how the Mauguin-effect influences the optical perceptibility of the twist Freedericksz-threshold. The simulations revealed that the adverse effect of the adiabatic light propagation can be sufficiently low if thin cells are used.

The applicability of the novel dielectric technique to determine  $K_{22}$  was demonstrated on the standard nematic compound 5CB and on the bent-core liquid crystal DT6PY6E6 in Sec. 4.2.3. The Freedericksz-transition measurements performed in the splay and the twist geometries could be used to determine a number of material parameters, including all elastic constants, using only a single planar cell filled with the compound DT6PY6E6 [P3]. The simpler experimental technique and the clearer evaluation might make this novel dielectric method superior compared to the optical depolarization measurements. The elastic constants of DT6PY6E6 were found to be in the usual range that is characteristic for rod-like nematic compounds. This could be explained by the presence of the intermediate alkyl-chains that increased the distance between the molecules. Consequently, without strong core-core interactions, the bent-core characteristics could not emerge.

Numerous material parameters were determined as the function of temperature for a rod-like compound 1008 (see Sec. 4.2.4) [P7]. The temperature dependent data of the elastic constants, the dielectric anisotropy, and of the diamagnetic susceptibility anisotropy were used in the analysis of low frequency pattern formation.

The studies of pattern formation (Sec. 4.3) in Phase 5 showed that the nature of the standard conductive electroconvection becomes different in the regime, where the period of the applied voltage is larger than the director relaxation time [P5, P6]. At high frequencies ( $f \sim 100$  Hz), the pattern contrast was found to be approximately constant in time, counter to the low frequency behavior, where the convection rolls appear as short flashes, so that in most of the driving period only the homogeneous state can be observed. The relative contrast modulation of the pattern images measured as the function of frequency, revealed that the transition from steady contrast to the flashing regime is continuous and it is characterized by the director relaxation time. At around 30 mHz and below, the appearance of flexodomains could be observed as separated flashes in addition to those of electroconvection.

The experimental findings were compared to the theoretical calculations of Alexei Krekhov in Ref. [P6], where a good qualitative agreement was found. A significant quantitative mismatch, however, was pointed out between the measured and the calculated frequency dependence of the pattern appearance time values within a half period of driving. Nevertheless, the inaccuracy of the theoretical description is not so surprising,

since the model considered only ohmic conductivity, even though ionic effects definitely play an important role at low frequencies.

Further investigations of low frequency pattern formation were performed using another rod-like compound (1008) [P7]. Due to the different material parameters and purity, 1008 could be used to study the time separated flashes of electroconvection and flexodomains in a much wider frequency range, than in the case of Phase 5. The contrast definition based on Fourier-analysis of the microscope images showed that the distinct patterns are separated not only in time but in the Fourier-space as well. The synchronized electric current measurements indicated a direct correlation between the peak in the nonlinear ionic current and the appearance of the electroconvection pattern that clearly shows the importance of ionic effects in the low frequency pattern formation. The absence of sharp thresholds at very low frequencies might be attributed to the effect of ions. Consequently, a precise theoretical description in the future should account for the weak electrolytic character of liquid crystal.

The critical voltages and wave numbers of electroconvection and flexodomains were determined as the function of frequency from 10 mHz to 10 Hz. A crossover was found between EC and FD at around 60 mHz, due to the different frequency dependence of their threshold voltages. A morphological transition from the oblique conductive to the oblique dielectric roll structure could be observed close to 7 Hz, which was an interesting finding, because there were no previous reports of such transition found.

The critical wave vector of flexodomains was determined as the function of temperature, thus the combination of flexoelectric coefficients  $|e_1 - e_3|$  could be obtained versus  $T$ . The calculations were performed analytically, using the model with one elastic constant approximation, and numerically, utilizing the novel theory that considers elastic anisotropy. It has turned out that the  $|e_1 - e_3|$  values obtained by the different methods lie close to each other, because the critical parameters of flexodomains are not sensitive to the elastic anisotropy in the used combination of material constants. The temperature dependence of  $|e_1 - e_3|$  supported the molecular theory of flexoelectricity predicting that  $|e_1 - e_3|$  is proportional to the square of the scalar order parameter.

Flexodomains were also found in the bent-core compound CIPbis10BB. Using the critical wave number of FDs, the difference of the flexoelectric coefficients was calculated by two methods at the temperature, for which the material parameters were determined

before. The model considering one-elastic-constant approximation gave similar result than the theory accounting for anisotropic elasticity, alike to the case of 1O08. The flexoelectric parameter  $|e_1 - e_3|$  of the bent-core compound was found to be larger than that of the rod-like material, compared at the closest relative temperatures. Nevertheless, the giant flexoelectricity of CIPbis10BB, indicated by both direct [60] and converse [61] mechanical flexing experiments and interpreted as the consequence of polar clusters, could not be reproduced by this method. Rather the  $|e_1 - e_3|$  deduced from the properties of flexodomains fits well in the range of the values given by other electro-optical measurements on bent-core nematics [67, 68, 114].

Nevertheless, a complete theoretical explanation for the three orders of magnitude discrepancy between the results of different measurement methods does not exist yet. The problem is that a continuum description of an inhomogeneous system, where nano-scale molecular clusters are dispersed in a nematic matrix, is not straightforward. Qualitative explanations [13], however, suggest that in order to measure giant flexoelectricity, the clusters have to be aligned or activated somehow, which was guaranteed during the direct measurement of the flexoelectric current by the massive mechanical excitation. The electric field induced bending of a flexible cell also indicated giant flexoelectricity [61], but only above a threshold electric field about  $1 \text{ V}/\mu\text{m}$ . This finding also suggests that the giant flexoelectricity does not originate from the classical microscopic mechanism of flexoelectricity that should give a linear response to the electric field. All electro-optical studies [67, 68, 114] that measured regular values of flexoelectric parameters used significantly lower fields than  $1 \text{ V}/\mu\text{m}$ .

It would be interesting to test the apparent strength of flexoelectricity using rod-like and bent-core materials by methods that can operate at adjustable levels of electric fields. This can be achieved in the case of flexodomains by using bias magnetic fields along the rubbing direction of the planar cell. By having a positive magnetic susceptibility anisotropy, the magnetic field stabilizes the homogeneous state, thus an increase of the threshold voltage of flexodomains is expected. Applying a sufficiently large  $B$ , the threshold voltage of FDs could be high enough to reach the critical electric field that might induce an observable transition in the behavior of a bent-core compound by the activation of the polar clusters. An obvious continuation of the work presented in this dissertation could be to perform such studies of flexodomains in magnetic fields.



## Appendix A

# Theoretical description of the splay geometry

In Sec. 3.2.1, the main steps of the continuum theoretical calculations in the splay geometry were presented. Here a more detailed derivation can be found.

Let us consider a planar cell filled with a nematic liquid crystal in the geometry illustrated in Fig. 3.4. The first task is to calculate the director field as the function of the magnetic field  $B$  and the applied voltage  $U$ . The electric and magnetic fields are present along the normal direction of the substrates. Assuming a homogeneous deformation, the director can be described by the  $z$ -dependent tilt angle  $\Theta(z)$ , as  $\mathbf{n} = (\cos \Theta, 0, \sin \Theta)$  shown in Eq. (3.3). The total free energy density of the system is given by the sum of the elastic, the magnetic and the electric terms. In contrast to the magnetic case, the electric field cannot be considered homogeneous in the cell if the director is inhomogeneous (see Sec. 1.2.2). According to the Maxwell equation  $\nabla \mathbf{D} = 0$ , the  $z$ -component of the electric displacement vector is constant in the cell:

$$D_z = \varepsilon_0 \varepsilon_{\perp} E(z) + \varepsilon_0 \varepsilon_a E(z) \sin^2 \Theta. \quad (\text{A.1})$$

Using Eq. (A.1), the experimentally controllable parameter, the voltage ( $U$ ) can be connected to  $D_z$ :

$$U = \int_0^d E(z) dz = \frac{D_z}{\varepsilon_0} \int_0^d \frac{1}{\varepsilon_{\perp} + \varepsilon_a \sin^2 \Theta} dz. \quad (\text{A.2})$$

The total free energy can be calculated by combining Eqs. (1.1), (1.4), (1.6), and (3.3):

$$f_{tot} = \frac{1}{2} (K_{11} \cos^2 \Theta + K_{33} \sin^2 \Theta) (\Theta')^2 - \frac{1}{2} D_z E - \frac{1}{2} \frac{\chi_a}{\mu_0} B^2 \sin^2 \Theta \quad (\text{A.3})$$

In equilibrium,  $f_{tot}$  is minimal, thus the solution of the Euler-Lagrange equation (Eq. (3.4)) gives the equilibrium director configuration. Combining Eqs. (A.1), (A.3) and (3.4), results in an equation that can be transformed into the following:

$$\frac{d}{dz} \left\{ \frac{1}{2} (K_{11} \cos^2 \Theta + K_{33} \sin^2 \Theta) (\Theta')^2 - \frac{D_z}{2\varepsilon_0 \varepsilon_{\perp} + \varepsilon_a \sin^2 \Theta} + \frac{1}{2} \frac{\chi_a}{\mu_0} B^2 \sin^2 \Theta \right\} = 0 \quad (\text{A.4})$$

A trick was used in the derivation, namely both sides of the Euler-Lagrange equation was multiplied by  $\Theta'$ .

The pure magnetic case is considered if  $U = 0$  and  $B \neq 0$ . After the integration of Eq. (A.4) with  $D_z = 0$ , we can get:

$$\Theta' = \sqrt{\frac{c - \frac{\chi_a}{\mu_0} B^2 \sin^2 \Theta}{K_{11} \cos^2 \Theta + K_{33} \sin^2 \Theta}}, \quad (\text{A.5})$$

where the integration constant  $c = \frac{\chi_a}{\mu_0} B^2 \sin^2 \Theta_m$ , is consistent with the symmetry arguments of  $\Theta'(z)|_{z=d/2} = 0$ ,  $\Theta(z)|_{z=d/2} = \Theta_m$  (Eq. 3.6), where  $\Theta_m$  is the maximal tilt angle in the middle of the cell. The next trick of integration results in an important equation:

$$\frac{d}{2} = \int_0^{d/2} dz = \int_{\Theta_0}^{\Theta_m} \frac{1}{\Theta'} d\Theta = \frac{B_{ts0}}{B} \frac{d}{\pi} \int_{\Theta_0}^{\Theta_m} \sqrt{\frac{1 + \kappa \sin^2 \Theta}{\sin^2 \Theta_m - \sin^2 \Theta}} d\Theta, \quad (\text{A.6})$$

where  $\kappa = (K_{33} - K_{11})/K_{11}$ , Eqs. (A.5), (1.7), and the boundary condition  $\Theta(z)|_{z=0} = \Theta_0$  (Eq. 3.5) were used. After performing the variable transformation  $\sin \Theta = \sin \Theta_m \sin \xi$ , Eq. 3.7 can be obtained. We note that the threshold field  $B_{ts0}$  can be derived by calculating the limit of  $\Theta_m \rightarrow 0$ .

In order to calculate the measurable effective dielectric constant ( $\varepsilon_{eff}$ ) of a cell, the liquid crystal has to be split into thin slabs of thickness  $dz$  as it was seen in twist geometry in Fig. 3.6. The capacitance of the  $i$ th slab is  $\delta C_i = \varepsilon_0 \varepsilon_i \frac{A}{dz}$ , where  $A$  is the area of the slab, and  $\varepsilon_i$  is the local effective dielectric constant. The capacitance  $C$  of the cell can be calculated as the net of the  $\delta C_i$  capacitances connected in series:

$$\frac{1}{C} = \sum_i \frac{1}{\delta C_i} = \frac{1}{\varepsilon_0 A} \sum_i \frac{dz}{\varepsilon_i}. \quad (\text{A.7})$$

Replacing the sum by an integral, and using the empty cell capacitance  $C_0 = \varepsilon_0 \frac{A}{d}$ , and the local effective dielectric constant  $\varepsilon_i \Leftrightarrow \varepsilon(\Theta(z)) = \varepsilon_{\perp} + \varepsilon_a \sin^2 \Theta(z)$  obtained

from Eq. (A.1), the effective dielectric constant is given in the form of Eq. (3.8). The final expression Eq. (3.9) can be get after the variable transformations  $dz = \frac{d\Theta}{\Theta'}$  using Eq. (A.5), and  $\sin \Theta = \sin \Theta_m \sin \xi$ .

The case considering  $U \neq 0$  and  $B = 0$  can be similarly treated as the one discussed above, therefore here only the main steps of the derivation are presented. First,  $\Theta'$  has to be expressed via the integration of Eq. (A.4). The result has to be used in the variable transformation in the integral of Eq. (A.2), similarly to Eq. (A.6). Then switching the integral variable to  $\xi$  results in Eq. (3.13).

## Appendix B

### Fitting methods

The complex nonlinear least squares method was used to fit the experimental data of  $\varepsilon'(f)$  and of  $\varepsilon''(f)$  in one step. In order to perform the fitting, the sum  $Q$  has to be calculated:

$$Q(\mathbf{p}_f)|_{\mathbf{p}_c} = \sum_{i=1}^n \left[ (\varepsilon'_{meas}(f_i) - \varepsilon'_{calc}(f_i, \mathbf{p}_f, \mathbf{p}_c))^2 + (\varepsilon''_{meas}(f_i) - \varepsilon''_{calc}(f_i, \mathbf{p}_f, \mathbf{p}_c))^2 \right], \quad (\text{B.1})$$

where  $n$  is number of the different frequencies measured;  $\varepsilon'_{meas}(f_i)$  and  $\varepsilon''_{meas}(f_i)$  are the values of the real, and imaginary parts of the complex dielectric permittivity measured at the frequency  $f_i$ ;  $\varepsilon'_{calc}(f_i, \mathbf{p}_f, \mathbf{p}_c)$  and  $\varepsilon''_{calc}(f_i, \mathbf{p}_f, \mathbf{p}_c)$  are the calculated values using the model functions of Eqs. (1.21) and (1.21) respectively. The vectors  $\mathbf{p}_f$  and  $\mathbf{p}_c$  contain the parameters (e.g. relaxation frequencies, dielectric increments, ...) that are wanted to be fitted or to be kept constant, respectively.

The best fit corresponds to the parameter set  $\mathbf{p}_f^*$  that minimizes  $Q$ :  $Q(\mathbf{p}_f^*)|_{\mathbf{p}_c} = \min_{\mathbf{p}_f} (Q(\mathbf{p}_f)|_{\mathbf{p}_c})$ . The optimization of  $Q(\mathbf{p}_f)|_{\mathbf{p}_c}$  was done by varying the fit variables (the elements of  $\mathbf{p}_f$ ) in Matlab by the nonlinear optimization function *fminsearch*, resulting in the best fit.

The fitting of the experimental data obtained from the splay Fredericksz-transitions was performed similarly as discussed above. The sum of the square differences between the experimental and numerically calculated data is defined in general as:

$$\tilde{Q}(\tilde{\mathbf{p}}_f)|_{\tilde{\mathbf{p}}_c} = \sum_{i=1}^{\tilde{n}} (F_{meas}(\Lambda_i) - F_{calc}(\Lambda_i, \tilde{\mathbf{p}}_f, \tilde{\mathbf{p}}_c))^2, \quad (\text{B.2})$$

where  $\tilde{n}$  is number of the different applied magnetic fields or voltages measured;  $F_{meas}(\Lambda_i)$  is the value of  $\varepsilon_{eff}$  or  $\Delta\varphi$  measured at an applied  $(\Lambda_i =)B_i$  or  $(\Lambda_i =)U_i$ ;

$F_{calc}(\Lambda_i, \tilde{\mathbf{p}}_{\mathbf{f}}, \tilde{\mathbf{p}}_{\mathbf{c}})$  corresponds to the value of  $\varepsilon_{eff}$  or  $\Delta\varphi$  calculated numerically by Matlab functions based on the implementations of the continuum theoretical calculations shown in Sec. 3.2.1. The vectors  $\tilde{\mathbf{p}}_{\mathbf{f}}$  and  $\tilde{\mathbf{p}}_{\mathbf{c}}$  contain the parameters that are wanted to be fitted (e.g. threshold field, combination of elastic constants) or to be kept constant (e.g. cell thickness), respectively.

Here the minimization of  $\tilde{Q}$  was also done with the built-in Matlab function *fminsearch* giving the fit values of the required quantities such as  $B_{ts0}$  and  $\kappa$ .

## Appendix C

# Dielectric measurement using an oscilloscope

Studying the change of the effective dielectric constant as the function of the applied magnetic field  $B$  in the twist geometry required very precise measurements of the impedance. In setup S2, the most reliable results could be obtained using a TiePie Handyscope HS3 instrument with Ithaco Model 1642 current sensitive preamplifier. The function generator output of the HS3 device was used to apply a sinusoidal signal with  $f = 1$  kHz, and  $U_{ampl} = 30$  mV voltage amplitude to the liquid crystal cell. The applied voltage  $\tilde{U}(t) = U_{ampl} \sin(2\pi ft)$  was measured by the Channel 1 of the oscilloscope. Channel 2 was used to record the signal proportional to the current in the circuit. Both channels were triggered by the function generator, and the recorded lengths of the signals were 40 times  $1/f$ . Using the known voltage-current conversion factor of the preamplifier, the current signal could be calculated:  $\tilde{I}(t) = I_{ampl} \sin(2\pi ft + \psi)$ , where  $I_{ampl}$  is the amplitude of the current, and  $\psi$  is a phase shift with respect to the driving voltage. In order to precisely determine  $I_{ampl}$ , and  $\psi$ , the operating principle of a dual-phase lock-in detector was utilized. The signal  $\tilde{U}_{\pi/2}(t) = U_{ampl} \sin(2\pi ft + \pi/2)$  was calculated by shifting the phase of Channel 1 by  $\pi/2$ . The quantities  $X$  and  $Y$  required for the further calculations, are given as:

$$X = \langle \tilde{U}(t) \cdot \tilde{I}(t) \rangle, \quad Y = \langle \tilde{U}_{\pi/2}(t) \cdot \tilde{I}(t) \rangle, \quad (\text{C.1})$$

where  $\langle \rangle$  denotes averaging. The unknown phase  $\psi$  and the current amplitude  $I_{ampl}$  can be calculated by:

$$I_{ampl} = \frac{2\sqrt{X^2 + Y^2}}{U_{ampl}}, \quad \psi = \arctan(Y/X). \quad (\text{C.2})$$

The net complex impedance can be obtained from:

$$Z = \frac{U_{ampl}}{I_{ampl} \exp(-i\psi)}. \quad (\text{C.3})$$

Nevertheless,  $Z$  does not equal to impedance of the liquid crystal cell ( $Z_c$ ), because it contains the contributions of the connecting wires ( $Z_s$ ) and parasitic impedances ( $Z_o$ ) connected parallel with the cell as seen in Fig. C.1. In order to extract the contribution

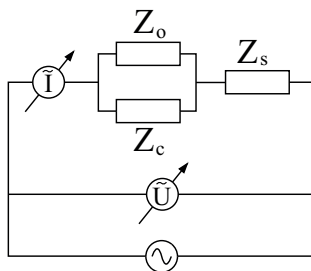


**Fig. C.1:** The schematic circuit of the dielectric measurement performed with an oscilloscope.

that originates only from the cell, corrections have to be performed. Disconnecting the cell from the circuit gives the opportunity to measure  $Z_o$ , and replacing the cell with a short circuit connection allows to measure  $Z_s$  using the procedure discussed above. We note that  $Z_o \gg Z_s$  was assumed. The impedance of the cell is given by:

$$Z_c = Z_o \left( \frac{Z_o}{Z - Z_s} - 1 \right)^{-1}. \quad (\text{C.4})$$

At  $f = 1$  kHz, the equivalent circuit of the liquid crystal cell can well be approximated by a parallel RC-term, hence the contribution of the ITO- and the alignment-layers can be neglected (see Fig. 3.1(b)). The corresponding resistance  $R$  and the capacitance  $C$  of the liquid crystal layer can be calculated by:

$$R = \frac{|Z_c Z_c^*|}{|\text{Re}(Z_c)|}, \quad C = \frac{|\text{Im}(Z_c)|}{2\pi f |Z_c Z_c^*|}, \quad (\text{C.5})$$

where  $'^*$ ,  $\text{Re}()$ , and  $\text{Im}()$  denote complex conjugation, real, and imaginary part, respectively. The effective dielectric constant is finally obtained by  $\varepsilon_{eff} = C/C_0$ , where  $C_0$  is the capacitance of the empty cell.

## Bibliography

- [1] A. Jákli and A. Saupe, *One- and Twodimensional Fluids*. Taylor & Francis, New York, 2006.
- [2] P. De Gennes and J. Prost, *The Physics of Liquid Crystals*. Clarendon Press, Oxford, 1993.
- [3] H. Coles and M. Pivnenko, “Liquid crystal ‘blue phases’ with a wide temperature range,” *Nature*, vol. 436, no. 7053, pp. 997–1000, 2005.
- [4] H. Takezoe and Y. Takanishi, “Bent-core liquid crystals: Their mysterious and attractive world,” *Jpn. J. Appl. Phys. 1*, vol. 45, no. 2 A, pp. 597–625, 2006.
- [5] D. Link, G. Natale, R. Shao, J. Maclellan, N. Clark, E. Körblova, and D. Walba, “Spontaneous formation of macroscopic chiral domains in a fluid smectic phase of achiral molecules,” *Science*, vol. 278, no. 5345, pp. 1924–1927, 1997.
- [6] G. Heppke, A. Jákli, S. Rauch, and H. Sawade, “Electric-field-induced chiral separation in liquid crystals,” *Phys. Rev. E*, vol. 60, no. 5 A, pp. 5575–5579, 1999.
- [7] Y. Shimbo, Y. Takanishi, K. Ishikawa, E. Gorecka, D. Pocięcha, J. Mieczkowski, K. Gomola, and H. Takezoe, “Ideal liquid crystal display mode using achiral banana-shaped liquid crystals,” *Jpn. J. Appl. Phys. 2*, vol. 45, no. 8-11, pp. L282–L284, 2006.
- [8] J. Etxebarria and M. Ros, “Bent-core liquid crystals in the route to functional materials,” *J. Mater. Chem.*, vol. 18, no. 25, pp. 2919–2926, 2008.
- [9] R. Verduzco, P. Luchette, S. Hong, J. Harden, E. Dimasi, P. Palffy-Muhoray, S. Kilbey II, S. Sprunt, J. Gleeson, and A. Jákli, “Bent-core liquid crystal elastomers,” *J. Mater. Chem.*, vol. 20, no. 39, pp. 8488–8495, 2010.
- [10] I. Stewart, *The Static and Dynamic Continuum Theory of Liquid Crystals*. Taylor & Francis, New York, 2004.
- [11] D. Demus, J. Goodby, G. Gray, H.-W. Spiess, and V. Vill, eds., *Handbook of Liquid Crystals*. Wiley-VCH, Weinheim, 1998.
- [12] R. Meyer, “Piezoelectric effects in liquid crystals,” *Phys. Rev. Lett.*, vol. 22, no. 18, pp. 918–921, 1969.
- [13] A. Buka and N. Éber, eds., *Flexoelectricity in Liquid Crystals. Theory, Experiments and Applications*. Imperial College Press, London, 2012.

- 
- [14] A. K. Tagantsev, "Piezoelectricity and flexoelectricity in crystalline dielectrics," *Phys. Rev. B*, vol. 34, pp. 5883–5889, Oct 1986.
- [15] H. Fröhlich, *Theory of Dielectrics*. Oxford University Press, London, 1958.
- [16] W. Maier and G. Meier, "Eine einfache theorie der dielektrischen eigenschaften homogen orientierter kristallinflüssiger phasen des nematischen typs," *Z. Naturforsch.*, vol. 16 A, no. 2, pp. 262–267, 1961.
- [17] K. S. Cole and R. H. Cole, "Dispersion and absorption in dielectrics," *J. Chem. Phys.*, vol. 10, p. 98, 1942.
- [18] S. Havriliak and S. Negami, "A complex plane representation of dielectric and mechanical relaxation processes in some polymers," *Polymer*, vol. 8, no. 0, pp. 161 – 210, 1967.
- [19] P. Debye, *Polar Molecules*. Chemical Catalogue Co., New York, 1929.
- [20] N. K. Mehrotra, T. C. Pant, and M. C. Saxena, "Study of dielectric relaxation mechanism and mutual viscosity in some aromatic compounds," *Bull. of The Chem. Soc. of Jap.*, vol. 45, pp. 356–358, 1972.
- [21] L. Onsager, "Electric moments of molecules in liquids," *J. Am. Chem. Soc.*, vol. 58, no. 8, pp. 1486–1493, 1936.
- [22] F. Gouda, S. Lagerwall, K. Skarp, B. Stebler, F. Kremer, and S. Vallerien, "Broad band dielectric relaxation spectroscopy of a chiral smectic b-crystal phase," *Liq. Cryst.*, vol. 17, pp. 367–379, 1994.
- [23] A. Price and A. Buka, "Dielectric dispersion in nematogens," in *Advances in Liquid Crystal Research and Applications* (L. Bata, ed.), pp. 267–278, Pergamon Press, New York, 1980.
- [24] A. Buka, P. G. Owen, and A. H. Price, "Dielectric relaxation in mbba," *Mol. Cryst. Liq. Cryst.*, vol. 51, no. 3-4, pp. 295–301, 1979.
- [25] J. Kirkwood, "The dielectric polarization of polar liquids," *J. Chem. Phys.*, vol. 7, no. 10, pp. 911–919, 1939.
- [26] H. Kresse, *Physical Properties of Liquid Crystals: Nematics*, ch. Dynamic dielectric properties of nematics, pp. 277–287. Inspec, London, 2001.
- [27] J. McConnell, *Rotational Brownian Motion and Dielectric Theory*. Academic Press, New York, 1980.
- [28] L. Bata and A. Buka, "Dielectric measurements on smectic-a and nematic phases," *Acta Phys. Pol.*, vol. 54 A, pp. 635–641, 1978.
- [29] W. Coffey and Y. Kalmykov, "Rotational diffusion and dielectric relaxation in nematic liquid crystals," *Adv. Chem. Phys.*, vol. 113, pp. 487–551, 2000.
- [30] A. Levstik, T. Carlsson, C. Filipic, I. Levstik, and B. Zeks, "Goldstone mode and soft mode at the smectic-a\* smectic-c\* phase transition studied by dielectric relaxation," *Phys. Rev. A*, vol. 35, pp. 3527–3534, Apr 1987.

- 
- [31] E. Hecht, *Optics*. Addison Wesley, San Francisco, 2002.
- [32] E. Collett, *Field Guide to Polarization*. SPIE Press, Bellingham, 2005.
- [33] D.-K. Yang and S.-T. Wu, *Fundamentals of Liquid Crystal Devices*. John Wiley & Sons Ltd, West Sussex, 2006.
- [34] L. Kramer and W. Pesch, *Pattern Formation in Liquid Crystals*, ch. Electrohydrodynamic instabilities in nematic liquid crystals, pp. 221–255. Springer, New York, 1996.
- [35] L. Blinov and V. Chigrinov, *Electrooptic Effects in Liquid Crystal Materials*. Springer, Berlin, 1994.
- [36] S. Pikin, *Structural Transformations in Liquid Crystals*. Gordon and Breach Science Publishers, New York, 1991.
- [37] A. Buka, N. Éber, W. Pesch, and L. Kramer, *Self-Assembly, Pattern Formation and Growth Phenomena in Nano-Systems*, vol. 218 of *NATO Science Series II, Mathematica, Physics and Chemistry*, ch. Convective Patterns In Liquid Crystals Driven By Electric Field, pp. 55–82. Springer, New York, 2006.
- [38] S. Rasenat, G. Hartung, B. Winkler, and I. Rehberg, “The shadowgraph method in convection experiments,” *Exp. Fluid*, vol. 7, pp. 412–420, 1989.
- [39] E. Carr, “Influence of electric fields on molecular alignment in liquid crystal p-(anisalamino)-phenyl acetate,” *Mol. Cryst. Liq. Cryst.*, vol. 7, pp. 253–268, 1969.
- [40] W. Helfrich, “Conduction-induced alignment of nematic liquid crystals: Basic model and stability considerations,” *J. Chem. Phys.*, vol. 51, pp. 4092–4105, 1969.
- [41] E. Bodenschatz, W. Zimmermann, and L. Kramer, “On electrically driven pattern-forming instabilities in planar nematics,” *J. Phys. France*, vol. 49, pp. 1875–1899, 1988.
- [42] A. Krekhov, W. Pesch, N. Éber, T. Tóth-Katona, and A. Buka, “Nonstandard electroconvection and flexoelectricity in nematic liquid crystals,” *Phys. Rev. E*, vol. 77, no. 2, p. 021705, 2008.
- [43] T. Tóth-Katona, N. Éber, and A. Buka, “Temporal response to harmonic driving in electroconvection,” *Phys. Rev. E*, vol. 83, p. 061704, 2011.
- [44] U. Schneider, M. De La Torre Jurez, W. Zimmermann, and I. Rehberg, “Phase shift of dielectric rolls in electroconvection,” *Phys. Rev. A*, vol. 46, no. 2, pp. 1009–1013, 1992.
- [45] H. Amm, M. Grigutsch, and R. Stannarius, “Optical characterization of electroconvection in nematics,” *Mol. Cryst. Liq. Cryst.*, vol. 320, pp. 11–27, 1998.
- [46] H. Amm, M. Grigutsch, and R. Stannarius, “Spatio-temporal analysis of electroconvection in nematics,” *Z. Naturforsch.*, vol. 53, no. 3-4, pp. 117–126, 1998.

- 
- [47] T. John, J. Heuer, and R. Stannarius, “Influence of excitation wave forms and frequencies on the fundamental time symmetry of the system dynamics, studied in nematic electroconvection,” *Phys. Rev. E*, vol. 71, no. 5, p. 056307, 2005.
- [48] N. Éber, S. Rozanski, S. Németh, A. Buka, W. Pesch, and L. Kramer, “Decay of spatially periodic patterns in a nematic liquid crystal,” *Phys. Rev. E*, vol. 70, no. 6 1, pp. 061706–1–061706–8, 2004.
- [49] W. Pesch, L. Kramer, N. Éber, and A. Buka, “Role of initial conditions in the decay of spatially periodic patterns in a nematic liquid crystal,” *Phys. Rev. E*, vol. 73, no. 6, p. 061705, 2006.
- [50] T. Tóth-Katona, N. Éber, A. Buka, and A. Krekhov, “Flexoelectricity and competition of time scales in electroconvection,” *Phys. Rev. E*, vol. 78, p. 036306, 2008.
- [51] L. E. Aguirre, E. Anoardo, N. Eber, and A. Buka, “Regular structures in 5cb liquid crystals under the joint action of ac and dc voltages,” *Phys. Rev. E*, vol. 85, p. 041703, APR 19 2012.
- [52] D. Wiant, J. Gleeson, N. Éber, K. Fodor-Csorba, A. Jákli, and T. Tóth-Katona, “Nonstandard electroconvection in a bent-core nematic liquid crystal,” *Phys. Rev. E*, vol. 72, no. 4, p. 041712, 2005.
- [53] L. Vistin, “A new electrostructural effect in liquid crystals of nematic type,” *Sov. Phys. Crystallogr.*, vol. 15, p. 514, 1970.
- [54] Y. Bobilev and S. Pikin, “Threshold piezoelectric instability in a liquid crystal,” *Sov. Phys. JETP*, vol. 45, pp. 195–198, 1977.
- [55] M. Barnik, L. Blinov, A. Trufanov, and B. Umanski, “Flexoelectric domains in nematic liquid crystals,” *Sov. Phys. JETP*, vol. 46, p. 1016, 1977.
- [56] M. Barnik, L. Blinov, A. Trufanov, and B. Umanski, “Flexo-electric domains in liquid crystals,” *J Phys (Paris)*, vol. 39, no. 4, pp. 417–422, 1978.
- [57] A. Krekhov, W. Pesch, and A. Buka, “Flexoelectricity and pattern formation in nematic liquid crystals,” *Phys. Rev. E*, vol. 83, no. 5, p. 051706, 2011.
- [58] D. Shen, S. Diele, G. Pelzl, I. Wirth, and C. Tschierske, “Designing banana-shaped liquid crystals without schiff’s base units: m-terphenyls, 2,6-diphenylpyridines and v-shaped tolane derivatives,” *J. Mater. Chem.*, vol. 9, pp. 661–672, 1999.
- [59] K. Fodor-Csorba, A. Vajda, G. Galli, A. Jákli, D. Demus, S. Holly, and E. Gács-Baitz, “Ester-type banana-shaped monomers and investigations of their electro-optical properties,” *Macromol. Chem. Physic.*, vol. 203, no. 10-11, pp. 1556–1563, 2002.
- [60] J. Harden, B. Mbang, N. Éber, K. Fodor-Csorba, S. Sprunt, J. Gleeson, and A. Jákli, “Giant flexoelectricity of bent-core nematic liquid crystals,” *Phys. Rev. Lett.*, vol. 97, no. 15, p. 157802, 2006.

- 
- [61] J. Harden, R. Teeling, J. Gleeson, S. Sprunt, and A. Jákli, “Converse flexoelectric effect in a bent-core nematic liquid crystal,” *Phys. Rev. E*, vol. 78, no. 3, p. 031702, 2008.
- [62] W. Helfrich, “Strength of piezoelectricity in liquid crystals,” *Z. Naturforsch.*, vol. 26, pp. 833–836, 1971.
- [63] A. Derzhanski and A. Petrov, “A molecular-statistical approach to the piezoelectric properties of nematic liquid crystals,” *Phys. Lett. A*, vol. 36, no. 6, pp. 483–484, 1971.
- [64] V. Domenici, C. Veracini, and B. Zalar, “How do banana-shaped molecules get oriented (if they do) in the magnetic field?,” *Soft Matter*, vol. 1, no. 6, pp. 408–411, 2005.
- [65] D. Wiant, S. Stojadinovic, K. Neupane, S. Sharma, K. Fodor-Csorba, A. Jákli, J. Gleeson, and S. Sprunt, “Critical behavior at the isotropic-to-nematic phase transition in a bent-core liquid crystal,” *Phys. Rev. E*, vol. 73, no. 3, p. 030703, 2006.
- [66] O. Francescangeli, V. Stanic, S. Torgova, A. Strigazzi, N. Scaramuzza, C. Ferrero, I. Dolbnya, T. Weiss, R. Berardi, L. Muccioli, S. Orlandi, and C. Zannoni, “Ferroelectric response and induced biaxiality in the nematic phase of a bent-core mesogen,” *Adv. Funct. Mater.*, vol. 19, no. 16, pp. 2592–2600, 2009.
- [67] K. van Le, F. Araoka, K. Fodor-Csorba, K. Ishikawa, and H. Takezoe, “Flexoelectric effect in a bent-core mesogen,” *Liq. Cryst.*, vol. 36, no. 10-11, pp. 1119–1124, 2009.
- [68] P. Kumar, Y. G. Marinov, H. P. Hinov, U. S. Hiremath, C. V. Yelamaggad, K. S. Krishnamurthy, and A. G. Petrov, “Converse flexoelectric effect in bent-core nematic liquid crystals,” *J. Phys. Chem. B*, vol. 113, no. 27, pp. 9168–9174, 2009.
- [69] C. Bailey, K. Fodor-Csorba, R. Verduzco, J. Gleeson, S. Sprunt, and A. Jákli, “Large flow birefringence of nematogenic bent-core liquid crystals,” *Phys. Rev. Lett.*, vol. 103, no. 23, p. 237803, 2009.
- [70] S. Dhara, F. Araoka, M. Lee, K. Le, L. Guo, B. Sadashiva, K. Song, K. Ishikawa, and H. Takezoe, “Kerr constant and third-order nonlinear optic susceptibility measurements in a liquid crystal composed of bent-shaped molecules,” *Phys. Rev. E*, vol. 78, no. 5, p. 050701, 2008.
- [71] C. Bailey, K. Fodor-Csorba, J. Gleeson, S. Sprunt, and A. Jákli, “Rheological properties of bent-core liquid crystals,” *Soft Matter*, vol. 5, no. 19, pp. 3618–3622, 2009.
- [72] S. Tanaka, H. Takezoe, N. Éber, K. Fodor-Csorba, A. Vajda, and A. Buka, “Electroconvection in nematic mixtures of bent-core and calamitic molecules,” *Phys. Rev. E*, vol. 80, no. 2, p. 021702, 2009.

- [73] P. Tadapatri, U. Hiremath, C. Yelamaggad, and K. Krishnamurthy, "Patterned electroconvective states in a bent-core nematic liquid crystal," *J. Phys. Chem. B*, vol. 114, no. 1, pp. 10–21, 2010.
- [74] P. Tadapatri, K. Krishnamurthy, and W. Weissflog, "Multiple electroconvection scenarios in a bent-core nematic liquid crystal," *Phys. Rev. E*, vol. 82, no. 3, p. 031706, 2010.
- [75] P. Sathyanarayana, M. Mathew, Q. Li, V. Sastry, B. Kundu, K. Le, H. Takezoe, and S. Dhara, "Splay bend elasticity of a bent-core nematic liquid crystal," *Phys. Rev. E*, vol. 81, no. 1, p. 010702, 2010.
- [76] B. Kundu, R. Pratibha, and N. Madhusudana, "Anomalous temperature dependence of elastic constants in the nematic phase of binary mixtures made of rodlike and bent-core molecules," *Phys. Rev. Lett.*, vol. 99, no. 24, p. 247802, 2007.
- [77] M.-G. Tamba, W. Weissflog, A. Eremin, J. Heuer, and R. Stannarius, "Electro-optic characterization of a nematic phase formed by bent core mesogens," *Eur. Phys. J. E*, vol. 22, no. 1, pp. 85–95, 2007.
- [78] M. May, W. Schöpf, I. Rehberg, A. Krekhov, and A. Buka, "Transition from longitudinal to transversal patterns in an anisotropic system," *Phys. Rev. E*, vol. 78, no. 4, p. 046215, 2008.
- [79] G. Nair, C. Bailey, S. Taushanoff, K. Fodor-Csorba, A. Vajda, Z. Varga, A. Bóta, and A. Jákli, "Electrically tunable color by using mixtures of bent-core and rod-shaped molecules," *Adv. Mater.*, vol. 20, no. 16, pp. 3138–3142, 2008.
- [80] G.-P. Chen, H. Takezoe, and A. Fukuda *Liq. Cryst.*, vol. 5, pp. 341–347, 1989.
- [81] J. Seltmann, A. Marini, B. Mennucci, S. Dey, S. Kumar, and M. Lehmann, "Non-symmetric bent-core liquid crystals based on a 1,3,4-thiadiazole core unit and their nematic mesomorphism," *Chem. Mater.*, vol. 23, no. 10, pp. 2630–2636, 2011.
- [82] A. Baise, I. Teucher, and M. Labes, "Effect of charge-transfer acceptors on dynamic scattering in a nematic liquid crystal," *Appl. Phys. Lett.*, vol. 21, no. 4, pp. 142–143, 1972.
- [83] N. Hill, W. Vaughan, A. Price, and M. Davies, *Dielectric properties and molecular behaviour*. Van Nostrand Reinhold, London, 1969.
- [84] C. Druon and J. Wacrenier, "Characterization of the sc phase in a liquid crystal by dielectric relaxation.," *Mol. Cryst. Liq. Cryst.*, vol. 108, no. 3-4, pp. 291–308, 1984.
- [85] A. Buka and L. Bata, "Dielectric permittivity and loss measurement on aligned nematic, smectic-a and smectic-c phases of dohop," in *Advances in Liquid Crystal Research and Applications* (L. Bata, ed.), pp. 261–266, Pergamon Press, New York, 1980.
- [86] D. Dunmur, G. Luckhurst, M. De La Fuente, S. Diez, and M. Pérez Jubindo, "Dielectric relaxation in liquid crystalline dimers," *J. Chem. Phys.*, vol. 115, no. 18, pp. 8681–8691, 2001.

- 
- [87] M. Stocchero, A. Ferrarini, G. Moro, D. Dunmur, and G. Luckhurst, "Molecular theory of dielectric relaxation in nematic dimers," *J. Chem. Phys.*, vol. 121, no. 16, pp. 8079–8097, 2004.
- [88] S. Hong, R. Verduzco, J. Williams, R. Twieg, E. Dimasi, R. Pindak, A. Jákli, J. Gleeson, and S. Sprunt, "Short-range smectic order in bent-core nematic liquid crystals," *Soft Matter*, vol. 6, no. 19, pp. 4819–4827, 2010.
- [89] C. Keith, A. Lehmann, U. Baumeister, M. Prehm, and C. Tschierske, "Nematic phases of bent-core mesogens," *Soft Matter*, vol. 6, no. 8, pp. 1704–1721, 2010.
- [90] S. Hong, R. Verduzco, J. Gleeson, S. Sprunt, and A. Jákli, "Nanostructures of liquid crystal phases in mixtures of bent-core and rod-shaped molecules," *Phys. Rev. E*, vol. 83, no. 6, p. 061702, 2011.
- [91] H. Kresse, U. Schuhmacher, D. Demus, and W. Schäfer, "Dielectric relaxation and viscosity in a mixture of liquid crystalline substances," *Mol. Cryst. Liq. Cryst.*, vol. 170, p. 1, 1989.
- [92] L. Bata and G. Molnár, "Dielectric dispersion measurements in a nematic liquid crystal mixture," *Chem. Phys. Lett.*, vol. 33, no. 3, pp. 535–539, 1975.
- [93] B. Ratna and R. Shashidhar, "Dielectric properties of 4'-n-alkyl-4-cyanobiphenyls in their nematic phases," *Pramana*, vol. 6, no. 5, pp. 278–283, 1976.
- [94] A. Buka and W. de Jeu, "Diamagnetism and orientational order of nematic liquid crystals.," *J. Phys. France*, vol. 43, no. 2, pp. 361–367, 1982.
- [95] Leenhouts, F., de Jeu, W.H., and Dekker, A.J., "Physical properties of nematic schiff's bases," *J. Phys. France*, vol. 40, no. 10, p. 989, 1979.
- [96] A. Bogi and S. Faetti, "Elastic, dielectric and optical constants of 4'-pentyl-4-cyanobiphenyl," *Liq. Cryst.*, vol. 28, no. 5, pp. 729–739, 2001.
- [97] W. Helfrich, "Inherent bounds to the elasticity and flexoelectricity of liquid crystals.," *Mol. Cryst. Liq. Cryst.*, vol. 26, no. 1-2, pp. 1–5, 1974.
- [98] S. Lagerwall, *Ferroelectric and Antiferroelectric Liquid Crystals*. Wiley-VCH, Weinheim, 1999.
- [99] P. Sathyanarayana, B. Sadashiva, and S. Dhara, "Splay-bend elasticity and rotational viscosity of liquid crystal mixtures of rod-like and bent-core molecules," *Soft Matter*, vol. 7, no. 18, pp. 8556–8560, 2011.
- [100] P. Tadapatri, U. Hiremath, C. Yelamaggad, and K. Krishnamurthy, "Permittivity, conductivity, elasticity, and viscosity measurements in the nematic phase of a bent-core liquid crystal," *J. Phys. Chem. B*, vol. 114, no. 5, pp. 1745–1750, 2010.
- [101] M. Treiber, N. Eber, A. Buka, and L. Kramer, "Travelling waves in electroconvection of the nematic phase 5: A test of the weak electrolyte model," *J. Phys. France*, vol. 7, no. 4, pp. 649–661, 1997.

- 
- [102] G. Derfel, “Numerical study of ionic current in dielectric liquid layer subjected to ac voltage,” *J. Mol. Liq.*, vol. 144, no. 1-2, pp. 59–64, 2009.
- [103] F. C. M. Freire, G. Barbero, and M. Scalerandi, “Electrical impedance for an electrolytic cell,” *Phys. Rev. E*, vol. 73, p. 051202, 2006.
- [104] F. Freire, A. Alexe-Ionescu, M. Scalerandi, and G. Barbero, “Voltage decay time of a liquid crystal cell submitted to a large difference of potential,” *Appl. Phys. Lett.*, vol. 89, no. 21, p. 214101, 2006.
- [105] A. L. Alexe-Ionescu, G. Barbero, and I. Lelidis, “Models for ionic contribution to the complex dielectric constant of nematic liquid crystals,” *Phys. Rev. E*, vol. 80, p. 061203, Dec 2009.
- [106] L. Palomares, J. Reyes, and G. Barbero, “Optical response of a nematic sample submitted to a periodic external electric field: role of the ionic impurities,” *Phys. Lett. A*, vol. 333, no. 1-2, pp. 157–163, 2004.
- [107] G. Barbero, A. M. Figueiredo Neto, F. C. M. Freire, and J. Le Digabel, “Relaxation time for the ionic current in a nematic cell under a large electric field,” *Phys. Rev. E*, vol. 74, p. 052701, 2006.
- [108] G. Barbero, G. Cipparrone, O. Martins, P. Pagliusi, and A. Figueiredo Neto, “Electrical response of a liquid crystal cell: The role of debye’s layer,” *Appl. Phys. Lett.*, vol. 89, no. 13, p. 132901, 2006.
- [109] G. Barbero, F. Batalioto, and A. Figueiredo Neto, “Theory of small-signal ac response of a dielectric liquid containing two groups of ions,” *Appl. Phys. Lett.*, vol. 92, no. 17, p. 172908, 2008.
- [110] R. Atasiei, A. Alexe-Ionescu, J. Dias, L. Evangelista, and G. Barbero, “Current measurements across a nematic cell submitted to an external voltage and its equivalent electrical circuit,” *Chem. Phys. Lett.*, vol. 461, no. 1-3, pp. 164–169, 2008.
- [111] M. Treiber and L. Kramer, “Bipolar electrodiffusion model for electroconvection in nematics,” *Mol. Cryst. Liq. Cryst.*, vol. 261, pp. 311–326, 1995.
- [112] A. Derzhanski and A. Petrov, “A molecular-statistical approach to the piezoelectric properties of nematic liquid crystals,” *Phys. Lett. A*, vol. 36, no. 6, pp. 483–484, 1971.
- [113] M. Osipov, *Flexoelectricity in Liquid Crystals. Theory, Experiments and Applications*, ch. Molecular Theory of Flexoelectricity in Nematic Liquid Crystals, pp. 101–135. Imperial College Press, London, 2012.
- [114] P. Salter, C. Tschierske, S. Elston, and E. Raynes, “Flexoelectric measurements of a bent-core nematic liquid crystal,” *Phys. Rev. E*, vol. 84, p. 031708, 2011.
- [115] C. Zhang, M. Gao, N. Diorio, W. Weissflog, U. Baumeister, S. Sprunt, J. T. Gleeson, and A. Jakli, “Direct Observation of Smectic Layers in Thermotropic Liquid Crystals,” *Phys. Rev. Lett.*, vol. 109, no. 10, p. 107802, 2012.

- [116] Y. Jang, V. P. Panov, C. Keith, C. Tschierske, and J. K. Vij, "Sign reversal in the dielectric anisotropy as functions of temperature and frequency in the nematic phase of a bent-core mesogen," *Appl. Phys. Lett.*, vol. 97, no. 15, p. 152903, 2010.



## List of publications

- [P1] P. Salamon, N. Éber, Á. Buka, S. Sprunt, J. T. Gleeson, and A. Jákli, "Dielectric properties of mixtures of a bent-core and a calamitic liquid crystal", *Phys. Rev. E*, vol. 81, p. 031711, 2010
- [P2] M. Majumdar, P. Salamon, A. Jákli, J. T. Gleeson, and S. Sprunt, "Elastic constants and orientational viscosities of a bent-core nematic liquid crystal", *Phys. Rev. E*, vol. 83, p. 031701, 2011
- [P3] P. Salamon, N. Éber, J. Seltmann, M. Lehmann, J. T. Gleeson, S. Sprunt, and A. Jákli, "Dielectric technique to measure the twist elastic constant of liquid crystals - The case of a bent-core material", *Phys. Rev. E*, vol. 85, p. 061704, 2012
- [P4] Á. Buka, N. Éber, K. Fodor-Csorba, A. Jákli, and P. Salamon, "Physical properties of a bent-core nematic liquid crystal and its mixtures with calamitic molecules", *Phase Transitions*, vol. 85, no. 10, pp. 872-887, 2012
- [P5] N. Éber, P. Salamon, and Á. Buka, "Competition between electric field induced equilibrium and non-equilibrium patterns at low frequency driving in nematics", 13th Small Triangle Meeting Proceedings, Slovak Academy of Sciences, Stará Lesná, Slovakia, pp. 56-63, 2012
- [P6] N. Éber, P. Salamon, L. Palomares, A. Krekhov, and Á. Buka, "Temporal evolution and alternation of mechanisms of electric field induced patterns at ultra-low-frequency driving", *Phys. Rev. E*, vol. 86, p. 021702, 2012
- [P7] P. Salamon, N. Éber, A. Krekhov, and Á. Buka, "Flashing flexodomains and electroconvection rolls in a nematic liquid crystal", *Phys. Rev. E*, vol. 87, p. 032505, 2013

The publication below is not related to the subject of this Dissertation:

- Z. Li, P. Salamon, A. Jákli, K. Wang, C. Qin, Q. Yang, Z. Liu, and J. Wen, "Synthesis and mesomorphic properties of resorcylic di[4-(4-alkoxy-2,3-diflorophenyl)ethynyl] benzoate liquid crystals", *Liq. Cryst.*, vol. 37, p. 427, 2010

# Theses

1. Using dielectric spectroscopy, I showed that a typical bent-core nematic liquid crystal exhibits qualitatively different frequency dependent dielectric properties, than regular rod-like nematic liquid crystals. I found five dielectric relaxations in the nematic phase of the bent-core compound, in contrast to the number of three that is usual for rod-like nematic materials. One relaxation of the bent-core compound exhibited a characteristic frequency of a few kHz, that is several orders of magnitude lower, than the lowest frequency relaxation in regular rod-like nematic liquid crystals [P1, P4].
2. I investigated the binary mixtures of rod-like and bent-core liquid crystals with dielectric spectroscopy. The experimental data indicated that the relaxations in the mixtures can be attributed to those observed in the pure compounds. I demonstrated, that the composite spectra of the mixtures can be reproduced as the superpositions of the relaxation modes in the bent-core and rod-like compounds [P1].
3. I determined the elastic constants of a typical bent-core liquid crystal, using dielectric and optical measurements of Fredericksz-transitions combined with the numerical fitting of the continuum theory of nematic liquid crystals. The twist and bend elastic constants were found to be one order of magnitude lower than those of rod-like nematic liquid crystals. The unusual findings were attributed to the effect of the bent-shape of the molecules, and to the effect of the molecular clusters [P2].
4. I found a new way to determine the twist elastic constant by the dielectric measurement of the magnetic Fredericksz-transition in the twist geometry. This novel technique utilizes the director pretilt at the alignment layers. The new dielectric method as well as the previously available optical technique was simulated for com-

parison and to reveal the effect of the most relevant parameters such as the cell thickness and the director pretilt. Both the simulation results and the experiments performed on a standard nematic and on a non-typical bent-core compound confirmed the applicability of the novel measurement principle. The elastic constants of the non-typical bent-core compound were found to be similar to those of rod-like nematic liquid crystals, attributed to the unusual molecular structure [P3].

5. I showed that the stationary patterns of standard conductive electroconvection become flashing gradually by decreasing the frequency of the driving voltage in the case of a rod-like liquid crystal. At low frequencies, where flexodomains can additionally be observed, two different pattern morphologies can rapidly appear and vanish after each other in the half period of the applied voltage. The characteristics of the patterns depend differently on the frequency, thus I could find a crossover between electroconvection and flexodomains at a critical frequency, where the threshold voltages for both types of patterns are equal [P5–P7].
6. I revealed that the appearance of the flashing electroconvection pattern coincides with the peak in the current measured in the driving circuit. The nonlinear current phenomenon was explained by the build up of ionic double layers near the insulating polyimide coatings on the electrodes after each polarity reversal. The less sharp threshold characteristics of electroconvection compared to flexodomains were also attributed to the effect of ionic impurities [P7].
7. Using the critical wave numbers of flexodomains measured at various temperatures, the difference of flexoelectric coefficients could be calculated as the function of temperature for a rod-like liquid crystal, that I used to confirm a prediction of the molecular theory of flexoelectricity. The characterization of flexodomains in the case of a bent-core nematic compound resulted in a slightly larger flexoelectric parameter than that of the rod-like liquid crystal; thus reproducing the giant flexoelectricity could not be achieved, similarly to the other electro-optical methods that used non-flexible cells [P7].

## Résumé

The dissertation is based on the work that aimed to reveal the difference between the novel type of bent-core and the well-known rod-like nematic liquid crystals by comparative experimental investigations.

My dielectric spectroscopic studies showed that there are five dielectric relaxations in the nematic phase of a bent-core compound, in contrast to the number of three, which is usual for rod-like nematic liquid crystals. One relaxation in the bent-core material was found at an unusually low frequency. The relaxations in the mixtures of a rod-like and a bent-core compound could be attributed to those observed in the pure liquid crystals. In order to discuss the findings, the molecular dipole moments were determined by quantum chemical calculations that accounted for the different conformations as well. The unusual dielectric properties were attributed to the different symmetry of the bent-core molecules and possibly the effect of the polar clusters.

I studied the electric and magnetic field induced reorientation (the Fredericksz-transitions) of the local symmetry axis of nematic liquid crystals by dielectric and optical methods. Applying the continuum theory of nematic liquid crystals, my numerical fitting method allowed to determine a number of material parameters from the experimental data. The twist and bend elastic constants of a bent-core nematic liquid crystal were found to be one order of magnitude smaller than the usual values, which was attributed to the bent molecular shape and the effect of the polar clusters. Furthermore, I proposed a novel dielectric measurement method for the twist elastic constant that I compared to the earlier optical technique with simulations and experiments as well.

I studied pattern formation phenomena in nematic liquid crystals by applying synchronized high-speed video microscopy. I found a qualitatively different behavior of the conductive electroconvection induced by largely decreasing the frequency of the driving voltage. At low frequencies, the alternating flashes of two distinct patterns (electroconvection and flexodomains) could be observed within a half period of the applied voltage signal. The characterization of flexodomains could be used to determine and compare the flexoelectric parameters of a rod-like and a bent-core nematic liquid crystal by applying a precise theoretical description published recently.

# Összefoglaló

A doktori értekezésem alapjául szolgáló munka fő célkitűzése az új típusú, hajlott törzsű molekulákból álló és a már jól ismert hagyományos rúd alakú molekulák alkotta nematikus folyadékkristályok tulajdonságainak összehasonlító kísérleti vizsgálata volt.

A dielektromos spektroszkópiai méréseim megmutatták, hogy a rúd alakú folyadékkristályoknál szokásos három relaxációval ellentétben egy hajlott törzsű folyadékkristály nematikus fázisában öt dielektromos relaxáció mérhető, melyek közül az egyik szokatlanul alacsony frekvencián jelentkezik. A rúd-alakú és a hajlott törzsű folyadékkristályok elegyeiben található relaxációkat sikerült szétválasztani és a komponenseket a különböző típusú anyagok relaxációihoz társítani. Az eredmények értelmezése érdekében a molekuláris dipólmomentumokat kvantumkémiai számításokkal kaptam meg, melyek a különböző konformációkat is figyelembe vették. A szokatlan dielektromos viselkedés a hajlott törzsű molekulák különböző szimmetriáinak, illetve esetlegesen a bennük megfigyelhető poláros klaszterek hatásának tulajdonítható.

A nematikus folyadékkristályok lokális anizotrópia-tengelyének (direktorának) külső elektromos és mágneses terekkel való átorientálását (a Freedericksz-átmeneteket) vizsgáltam dielektromos és optikai módszerekkel. A nematikus folyadékkristályok kontinuumelméletére alapuló numerikus illesztőprogramom a mérési adatokból számos anyagi állandó meghatározását tette lehetővé. A hajlott törzsű molekulák alkotta folyadékkristály csavarási és hajlítási rugalmas állandói a megszokotthoz képest egy nagyságrenddel kisebbnek bizonyultak, aminek magyarázatát a hajlott molekula-alak és a más módszerekkel már közvetlenül megfigyelt poláros klaszterek jelenléte adta. Továbbá a csavarási rugalmas állandó mérésére egy újfajta dielektromos technikát ajánlottam, melyet összehasonlítottam egy már ismert optikai módszerrel, szimulációk illetve mérési eredmények segítségével.

Nematikus folyadékkristályokban megfigyelhető mintázatképződési folyamatokat vizsgáltam polarizációs mikroszkópban nagy sebességű szinkronizált képrögzítő technikával. Az alkalmazott feszültség frekvenciájának jelentős csökkentésére a konduktív elektrokonvekció jellegének minőségi megváltozását találtam. Alacsony frekvenciákon, egy félperióduson belül két teljesen különböző mintázat (elektrokonvekció és flexodomén) egymást követő villanásszerű feltűnéseit tanulmányoztam. Egy rúd-alakú és egy hajlott törzsű nematikus folyadékkristályon megfigyelt flexodomének tulajdonságaiból a különböző típusú anyagok flexoelektromos paraméterét sikerült meghatározni és összehasonlítani egy a közelmúltban publikált, pontos elméleti leírás segítségével.